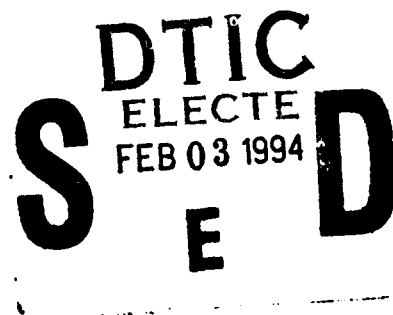


AFTT/GAE/ENY/93D-13

AD-A275 544



Comparison of the Dynamic Behavior of Composite  
Plates and Shells Incorporating Green's Strain Terms  
with the von Karman and Donnell Models

THESIS

Arthur E. Forral, Captain, USAF  
AFTT/GAE/ENY/93D-13

Approved for public release; distribution unlimited.

93-30414



93 12 15 03 4

Comparison of the Dynamic Behavior of Composite Plates and Shells Incorporating  
Green's Strain Terms with the von Karman and Donnell Models

THESIS

Presented to the Faculty of the Graduate School of Engineering  
of the Air Force Institute of Technology

Air University

In Partial Fulfillment of the  
Requirements for the Degree of  
Master of Science in Aeronautical Engineering

DTIC QUALITY INSPECTED 8

Arthur E. Forral, B.S.

Captain, USAF

December 1993

Accession For	
NTIS	CRA&I <input checked="" type="checkbox"/>
DTIC	TAB <input type="checkbox"/>
Unannounced <input type="checkbox"/>	
Justification _____	
By _____	
Distribution /	
Availability Codes	
Dist	Avail and / or Special
A-1	

### *Acknowledgements*

This thesis is part of a research project on the dynamic behavior of suddenly loaded composite shells; Dr. Anthony Palazotto, AFIT/ENY, principal investigator.

I wish to thank Dr. Palazotto for his expertise, guidance, and concern throughout this research; I consider him to be a giant in the world of structural analysis. I also wish to thank committee members Dr. Torvik and Captain Canfield for their guidance as well. It was my great fortune to have PhD candidate Captain Jim Greer accessible throughout my stay at AFIT. Much of my work was a follow-on to his research and his presence facilitated my efforts to an immense degree. A great deal of credit goes to the previous researchers Lt. Col. Scott Dennis and Dr. C.T. Tsai whose monumental efforts lead to the SHELL and DSHELL computer codes respectively. The sponsorship of Arnold Mayer of WL/FIV and Raje Nachman of AFOSR made this investigation possible; many thanks to them.

I am fortunate to be blessed with a family with a high degree of support and understanding over the years. A huge amount of credit goes to my wife, Kelly, who has been so selfless and giving. My two sons, Chris and Ryan, have been quietly supportive.

I am also grateful for the many opportunities that the Air Force has provided for me and my family throughout my career.

Arthur E. Forral

## *Table of Contents*

	Page
Acknowledgements . . . . .	ii
Table of Contents . . . . .	iii
List of Figures . . . . .	v
List of Tables . . . . .	x
Abstract . . . . .	xi
 I. INTRODUCTION . . . . .	 1-1
1.1 Historical Motivation . . . . .	1-3
1.2 Development of Current Approach . . . . .	1-5
1.3 Chaos . . . . .	1-6
1.4 Current Work . . . . .	1-7
 II THEORETICAL DEVELOPMENT	
2.1 Simplified Large Deflection/Rotation (SLR) . . . . .	2-1
2.2 Numerical Technique . . . . .	2-6
2.3 Chaos . . . . .	2-8
 III PROCEDURES . . . . .	 3-1
 IV RESULTS AND DISCUSSION	
4.1 Eight in. Radius Cylindrical Shell . . . . .	4-1
4.2 Twelve in. Radius Cylindrical Shell . . . . .	4-11
4.3 Six in. Radius Cylindrical Shell . . . . .	4-19

4.4 Four in. Radius Cylindrical Shell . . . . .	4-27
4.5 Twenty in. Radius Cylindrical Shell . . . . .	4-32
4.6 Sixty in. Radius Cylindrical Shell . . . . .	4-34
4.7 Flat Plate . . . . .	4-34
 V NUMERICAL STABILITY . . . . .	 5-1
 VI CHAOTIC BEHAVIOR . . . . .	 6-1
 VII SUMMARY, CONCLUSIONS, AND RECOMMENDATIONS	
7.1 Summary . . . . .	7-1
7.2 Conclusions . . . . .	7-2
7.3 Recommendations . . . . .	7-4
Appendix A Effect of Radius on Flexural Stiffness . . . . .	A-1
Bibliography. . . . .	BIB-1
Vita . . . . .	VITA-1

# *List of Figures*

Figure		Page
2.1	36 DOF isoparametric element	2-1
2.2	(a) Poincaré map of chaotic motion of a buckled beam with low damping. (b) Poincaré map of chaotic motion of a buckled beam for higher damping showing fractal-like structure from a strange attractor (from Moon [ :51]).	2-12
3.1	Composite cylindrical shell	3-2
3.2	Loading curves applied to cylindrical shells of various radii	3-2
3.3	Meshes representing cylindrical shells	3-3
3.4	Mesh representing a flat plate	3-4
4.1	Center node displacement of composite cylindrical shells subjected to a transverse step load applied to the center. Radius = 8 in.	4-2
4.2	Meshes representing composite cylindrical shells subjected to a transverse step load applied to the center. Radius = 8 in.	4-6
4.3	Deformation of an element of a composite cylindircal shell subjected to a transverse step load applied to the center. Radius = 8 in., SLR formulation. Dotted lines correspond to the undeformed state.	4-9
4.4	Center node displacement of a composite cylindrical shell subjected to a transverse step load applied to the center. Radius = 12 in., SLR formulation.	4-12
4.5	Center node displacement of a composite cylindrical shell subjected to a transverse step load applied to the center. Radius = 12 in., Donnell formulation.	4-12
4.6	Meshes representing composite cylindrical shells subjected to a transverse step load applied to the center. Radius = 12 in, SLR formulation.	4-13
4.7	Meshes representing composite cylindrical shells subjected to a transverse step load applied to the center. Radius = 12 in, Donnell formulation..	4-16

4.8	Center node displacement of composite cylindrical shells subjected to a transverse step load applied to the center. Radius = 6 in.	4-20
4.9	Meshes representing composite cylindrical shells subjected to a transverse step load applied to the center. Radius = 6 in, SLR formulation..	4-22
4.10	Meshes representing composite cylindrical shells subjected to a transverse step load applied to the center. Radius = 6 in, Donnell formulation..	4-24
4.11	Center node displacement of composite cylindrical shells subjected to a transverse step load applied to the center. Radius = 4 in.	4-28
4.12	Meshes representing composite cylindrical shells subjected to a transverse step load applied to the center. Radius = 4 in, SLR formulation..	4-29
4.13	Meshes representing composite cylindrical shells subjected to a transverse step load applied to the center. Radius = 4 in, Donnell formulation.	4-30
4.14	Center node displacement of a composite cylindrical shell subjected to a transverse step load applied to the center. Radius = 20 in, SLR formulation.	4-33
4.15	Center node displacement of a composite cylindrical shell subjected to a transverse step load applied to the center. Radius = 20 in, Donnell formulation.	4-33
4.16	Meshes representing composite cylindrical shells in an unloaded and collapsed state. Radius = 20 in.	4-35
4.17	Center node displacement of composite cylindrical shells subjected to a transverse step loads applied to the center. Radius = 60 in.	4-35
4.18	Various loading curves applied to flat composite plates.	4-37
4.19	Center node displacement of a composite plate subjected to a transverse step load applied to the center. Initial loading rate of $3.16(10^6)$ lbs/s.	4-37
4.20	Center node displacement of a composite plate subjected to a transverse step load applied to the center. Initial loading rate of $7.90(10^5)$ lbs/s	4-38

4.21	Center node displacement of a composite plate subjected to a transverse step load applied to the center. Initial loading rate of $1.58(10^5)$ lbs/s.	4-38
4.22	Center node displacement of a composite plate subjected to a transverse step load applied to the center. Initial loading rate of $7.90(10^4)$ lbs/s.	4-39
4.23	Effect of loading rate on the center node displacement of a composite plate subjected to a transverse step load applied to the center. Max load = 352 lbs.	4-39
4.24	Center node displacement of a composite plate subjected to a transverse step load applied to the center. Initial loading rate of $1.4(10^6)$ lbs/s, max. load of 4,228 lbs.	4-40
4.25	Meshes representing composite plates subjected to a transverse step load. Vertical displacements are scaled up by a factor of 4.	4-42
5.1	Numerical instability in the center node displacement of a composite cylindrical shell subjected to a transverse step load applied to the center. Radius = 6 in, SLR formulation.	5-2
5.2	Numerical instability in the center node displacement of a composite cylindrical shell subjected to a transverse step load applied to the center. Radius = 4 in, SLR formulation.	5-2
5.3	Numerically unstable solution of a deep composite cylindrical shell subjected to a transverse point load applied to the center.	5-3
6.1	Phase-plane trajectory for chaotic motion of a collapsed 20 in. radius composite cylindrical shell subjected to a transverse point load applied to the center. Shell is undamped.	6-2
6.2	Poincaré map of chaotic motion of a collapsed 20 in. radius composite cylindrical shell with no damping.	6-2
6.3	Portion of the center node displacement history of a collapsed composite cylindrical shell subjected to a transverse point load. Radius = 20 in., SLR formulation.	6-3
6.4	Phase-plane trajectory for chaotic motion of a flat composite plate subjected to transverse point load applied to the center.	6-3
6.5	Phase-plane trajectory of an uncollapsed 8 in. radius composite	6-6

	cylindrical shell subjected to a transverse point load applied to the center node, Donnell formulation.	
6.6	Pseudo-phase-plane trajectory for an uncollapsed 8 in. radius composite cylindrical shell subjected to a transverse point load applied to the center node, Donnell formulation.	6-6
6.7	Frequency spectrum of a collapsed 12 in. radius composite cylindrical shell subjected to a transverse point load applied to the center node, SLR formulation.	6-8
6.8	Frequency spectrum of a collapsed 12 in. radius composite cylindrical shell subjected to a transverse point load applied to the center node, Donnell formulation.	6-8
6.9	Frequency spectrum of a collapsed 20 in. radius composite cylindrical shell subjected to a transverse point load applied to the center node, SLR formulation.	6-9
6.10	Frequency spectrum of an uncollapsed 8 in. radius composite cylindrical shell subjected to a transverse point load applied to the center node, Donnell formulation.	6-9
6.11	Phase-plane trajectory for chaotic motion of a composite plate subjected to a transverse step load applied to the center. Initial loading rate of $3.16(10^6)$ lbs/s, max load of 1,592 lbs.	6-10
6.12	Phase-plane trajectory for chaotic motion of a composite plate subjected to a transverse step load applied to the center. Initial loading rate of $7.9(10^5)$ lbs/s, max load of 1,592 lbs.	6-10
6.13	Phase-plane trajectory for chaotic motion of a composite plate subjected to a transverse step load applied to the center. Initial loading rate of $7.9(10^5)$ lbs/s, max load of 1,592 lbs.	6-11
6.14	Scaled up version of Figure 6.13 revealing similar orbital trajectories.	6-11
6.15	Frequency spectrum of the center node of a composite plate subjected to a transverse step load applied to the center. Initial loading rate of $3.16(10^6)$ , max. load of 1,592 lbs.	6-13
6.16	Frequency spectrum of the center node of a composite plate subjected to a transverse step load applied to the center. Initial loading rate of $7.9(10^5)$ lbs/s max. load of 1,592 lbs.	6-13

6.17	Frequency spectrum of the center node of a composite plate subjected to a transverse step load applied to the center. Initial loading rate of $7.9(10^4)$ lbs/s, max. load of 1,592 lbs.	6-14
6.18	Poincaré map of a composite plate subjected to a transverse point load applied to the center. Initial loading rate of $7.9(10^4)$ lbs/s, max. load of 1,592 lbs.	6-14
6.19	Center node deflection of a composite plate subjected to a transverse step load applied to the center. Initial loading rate of $7.90(10^4)$ lbs/s, max. load of 1,592 lbs.	6-15
6.20	Possible convergence of the Lyapunov exponent of a transversely loaded composite plate (see Figure 6.19).	6-15
A.1	Thin arch.	A-1
A.2	Normal compressive stresses, due to $H$ and $V_1$ only, acting on a cross section perpendicular to the neutral axis.	A-3
A.3	Moments acting along an arch.	A-3
A.4	Radial shear stress distribution acting along an arch.	A-4
A.5	Average membrane stress distribution along a thin arch.	A-5

### *List of Tables*

Table	Page
3.1 Physical properties of AS4-3501-6 graphite epoxy composite (psi).	3-5
3.2 First three natural frequencies of composite cylindrical shells of varying radii.	3-6

### *Abstract*

The dynamic collapse behavior of thin composite cylindrical shells subjected to transverse point loads is considered. The dynamic behavior of the undamped cylindrical shells of varying radii is analyzed with a finite element formulation that incorporates all nonlinear Green's strain terms in the in-plane directions; transverse shear strains are linear and vary parabolically through the shell thickness. This formulation is denoted as the simplified large displacement/rotation (SLR) theory. Graphical representations are used extensively to examine dynamic behaviors not noted in similar research that utilized the DSHELL finite element code. Composite plate behavior is also explored. Comparison of the higher-order formulations to Donnell and von Karman models, modified with transverse shear flexibility, is also made. Several deep shell configurations, using the SLR and Donnell models, are analyzed in an effort to determine the maximum displacement and rotational limits of these formulations. The nonlinear features of the plates and shells imply the potential for *chaotic* behavior. Various techniques are used to characterize the chaotic behavior of these undamped shells in pre- and post-collapsed states.

# Comparison of the Dynamic Behavior of Composite Plates and Shells Incorporating Green's Strain Terms with the von Karman and Donnell Models

## *1. INTRODUCTION*

There has been considerable effort directed towards the study of composite materials because of their advantages over conventional isotropic materials. The high strength-to-weight properties of many composites are ideally suited towards aerospace applications. Composites are typically formed in lamina layers with the high strength properties usually oriented in the in-plane directions. Thus, composites can be made lighter and thinner than conventional isotropic materials in a given application. However, composites may be substantially weaker in the transverse directions, especially if the composite is thin. Therefore, depending on the application, the stability of a composite may be an important consideration.

The technical literature is rich in researchers' efforts to model the behavior of composite structures. Since the strength properties in a lamina may vary drastically from ply to ply with respect to a given reference, composites are clearly more complicated to analyze than isotropic materials. In an attempt to reduce the complexity of the mathematical model, analysts typically make simplifying assumptions especially if the laminate is thin. The model formulations in this research exploit this dimensionality as well. When applications involve small deflections and small rotations, many classical theories neglect or simplify nonlinear terms and yet retain good accuracy. However, when deflections become many times larger than the laminate thickness, a more thoughtful approach towards including higher-order nonlinear terms is required.

Linear bifurcation analysis is not suitable in predicting the collapse behavior of shells. For small deflections and rotations, linear bifurcation analysis may adequately predict the nonlinear stability limits of some structures, although some degree of error is expected (11:466). This is generally true for Euler columns and axially loaded flat plates since these structures experience little stress distribution or geometry changes prior to the onset of the buckling instability. On the other hand, thin composite shells may not collapse until moderate deflections, rotations, and stress redistributions have occurred. Therefore, it is expected that a real structure may collapse at a load quite different than that predicted by a linear bifurcation buckling analysis.

Von Karman is considered the first person to reconcile the buckling of cylindrical shells, observed in experiments, with a theoretical formulation which incorporates large deflection. "The main feature of the large deflection approach is that one or more nonlinear partial differential equations are solved approximately. The post-collapse curve branching from the fundamental equilibrium state is subsequently determined" (11:465). In his work with cylindrical shells subjected to axial loads and external pressure, von Karman showed that, at a load or pressure level less than the value predicted by linear bifurcation analysis, the deforming cylindrical shell jumps (i.e., snaps) into another equilibrium state, corresponding to the collapsed configuration. A similar approach was taken by Dennis and Palazotto (14); they also observed similar collapse characteristics in their work with transversely loaded shells. Their work is the basis for the findings contained in this research.

In recent years, a new scientific approach to analyzing complicated and seemingly unpredictable behavior has developed:

This new paradigm goes by the name of *Chaos*, referring to a scientific philosophy, an approach, and a set of methods to deal with the manifestations of chaos in the physical sciences. To a large extent the enthusiasm that has developed for Chaos is the result of the breadth of its applications. These applications for Chaos for understanding complex and unpredictable behavior range across the spectrum of scientific disciplines. Indeed, Chaos has much the same flavor as classical thermodynamics in that the fundamental ideas and results seem applicable to a wide variety of different physical systems. There is probably no physical system exhibiting unpredictable behavior that is presently not being scrutinized through the lens of Chaos by someone (16:vii)

By definition *chaotic* vibrations arise from physical systems whose input forces or excitations are known (deterministic). However, knowledge of all influences acting on a system and the exact laws governing the behavior does not guarantee accurate prediction of how a system's response will evolve over time. Even with huge advances in computer technology, Peitgen, Jürgen, and Saupe (15:viii) assert that the ability to see more accurately into future developments is unattainable. Moreover, they maintain that stricter determinism and apparently accidental development are not mutually exclusive, but rather that their coexistence is more the rule in nature. Therefore, as a researcher attempts to accurately model, to a high degree, the behavior of a physical system, some of the phenomenon that he or she may observe might be best analyzed with the tools developed from this new scientific approach.

### *1.1 Historical Motivation*

The subject of dynamic buckling of shells has drawn the attention of researchers over many years because of the numerous possible applications. Applications for the aerospace industry was one of the primary motivations for the interest in cylindrical shell buckling due to the possible performance and cost advantages that could result from a weight-

optimized structure. The vast majority of researchers were interested in the behavior of cylindrical shells when loaded with axial, radial pressure, and torque forces since these combinations are the basic loading configurations for cylindrical shell structures (5:413).

For example, Brush and Morton (1) published one of the first papers on experiments with the static buckling of shells with axial forces, with an intended application for missiles and launch vehicles. One advantage to the loading modes described is that closed form solutions may be derived, typically through the use of series solutions. Flugge (5:413-473) provides examples of this technique. One of the first American papers that examined the dynamic buckling of cylindrical shells was written by Yao (28) and examined the buckling of a cylinder under flexural loads and an external step pressure pulse. The formulations used were based on Mathieu and Donnell type equations.

In the last 30 years, there have been several approaches and solution methods in the static and dynamic analysis of plates and shells. In order to reduce the complexity of the general elasticity equations, many researchers utilized thin plate and shell assumptions which include 1) small rotations and deflections, 2) normals to the shell datum surface remaining normal before and after deformation, and 3) transverse normal stresses that are negligible. A common method is to use a two dimensional formulation to predict plate and shell behavior. Noor and Burton (12) have classified the various methods of modelling a multilayer plate with two-dimensional models (applicable to shell theory as well) into 4 general approaches. They are the 1) method of hypotheses, 2) method of expansion, 3) asymptotic integration technique, and 4) iterative methods and methods of successive corrections. The first approach is based on Kirchhoff-Love formulations with assumptions on the variations of displacements and strains (or stresses) in the thickness

direction. The second approach is based on series expansions with respect to the thickness parameter of the plate or shell. Power series, Legendre polynomials, and trigonometric series have been used. The third approach involves the formulation of recursive sets of two-dimensional equations from the three-dimensional elasticity equations. The fourth approach includes iterative approximations of the three-dimensional elasticity equations and successive corrections to the two-dimensional formulations.

### *1.2 Development of Current Approach*

Dennis and Palazotto (14) developed a simplified large displacement/rotation (SLR) formulation where the in-plane strain equations incorporated all nonlinear Green's strain terms while the transverse strain equations retained linear terms only. The transverse strain equations satisfy boundary conditions on the upper and lower surface of the shell. The kinematics equations are based on a power series expansion with respect to the thickness direction. The SLR formulation lead to the development of the SHELL computer code which was used for the static analysis of plates and shells. This is one of the computer codes used in this research. Comparisons to the previous work of Sabir and Lock (14:200) showed excellent agreement between the two approaches. Sabir and Lock used an assumed strain function and the finite element method to predict the collapse behavior of cylindrical shells. The SLR approach was also expanded to include analysis of shells composed of composite materials.

Tsai and Palazotto (26) incorporated the capability to perform dynamics analysis into the SLR approach. Their DSHELL computer code is one other program used in this work. A Newton-Rhapson iterative method and Beta-m time-marching integration scheme

is used to solve the differential equations of motion. Comparisons of DSHELL results to the work of Clough and Wilson (3), whose arbitrarily thin shells utilized an assumed constant transverse shear, showed excellent agreement. Greer (6) added the IDEAS™ post-processing feature to the program to graphically display the shell at any point in the loading history (this feature was not used in this work).

### 1.3 Chaos

An essentially two dimensional structural system, such as the thin composite plates and shells, is an extremely complex structure to analyze, especially when chaotic behavior is to be examined. Other work in numerical simulation of chaotic motion typically reduces the complexity by reducing the dimensionality and degrees of freedom. These simplified models still allow for a diversity of nonlinear features that is necessary in a truly chaotic system. Researchers such as Siljak (21), Moon (10), Nayfeh and Mook (12), Shaw and Holmes (20), and Kounadis (8) have examined simple structural systems (usually with one or two degrees of freedom) with geometric or material nonlinearities. Simulation of nonlinear behavior has also been carried out using piecewise-linear properties. For example, Thompson et al. (25:291) examined the dynamics of a tower using linear damping and bilinear stiffness beams. Their results demonstrated complex dynamic behavior that contained chaotic characteristics. Liaw (9) performed a more extensive analysis by examining a one-degree-of-freedom model that had similar stiffness and damping properties. He demonstrated that the system exhibited chaotic tendencies through quantitative (e.g., *Lyapunov* exponents) and qualitative (e.g., *bifurcation* diagrams) analyses.

#### 1.4 Current Work

An overall purpose of this research is to further elaborate on the dynamic behavior of cylindrical shells as predicted by the DSHELL computer code. Thus far, only a few researchers have used the DSHELL computer code to examine the complex collapse behavior of cylindrical shells. With so many possible shell configurations, there is the potential to do much more. Shell geometry, lengths, thicknesses, boundary conditions, and various composite ply orientations and materials are just a few of the parameters that can be varied.

One significant hurdle was recently overcome by Greer's work (6) in defining a method for selecting computational parameters that would lead to numerically stable results. Early efforts with the DSHELL code lead to results that were often misinterpreted. For example, it was originally thought that DSHELL could not perform accurate post-collapse analysis due to highly erratic results. However, Greer demonstrated that the proper choice of certain computational parameters would allow prediction of behavior long after the shell had collapsed. This ability to produce numerically stable results facilitated the study of *chaotic* motion in the collapsed shell.

In previous work, most of the studies in the dynamic behavior of cylindrical shells centered on the behavior of shells with shallow to moderate depths. It was not clear that DSHELL could predict the behavior of deeper shell geometries, nor was it clear Greer's method could be applied to these geometries, another objective is to gain insight on the limits of the SLR models. Moreover, there are extremely limited studies that examine composite cylindrical shell responses when subjected to a sudden transverse point load. A basis of comparison is therefore generated by using a more linearized model, namely,

the modified Donnell formulation. Finally, an attempt is made to gain insight into the chaotic behavior of complex structures, such as composite shells. Towards these goals, SPARC2, SPARC10, and Silicon Graphics UNIX computer systems were used extensively.

## II THEORETICAL DEVELOPMENT

### 2.1 Simplified Large Deflection/Rotation (SLR)

The finite element formulation used in this research is based on a total Lagrangian approach and features:

- (1) all non-linear in plane Green's strain terms and linear transverse strain terms
- (2) the capability for shell normals to the midplane to lose their orthogonality after loading.
- (3) zero  $\sigma_{33}$  normal stress due to thin shell assumptions.
- (4) transverse shear strains that vary parabolically through the shell thickness and vanish on the top and bottom surfaces of the shell.

Although a shell is three dimensional, a two dimensional formulation is used to model a thin shell. Figure 1 shows a typical shell element.

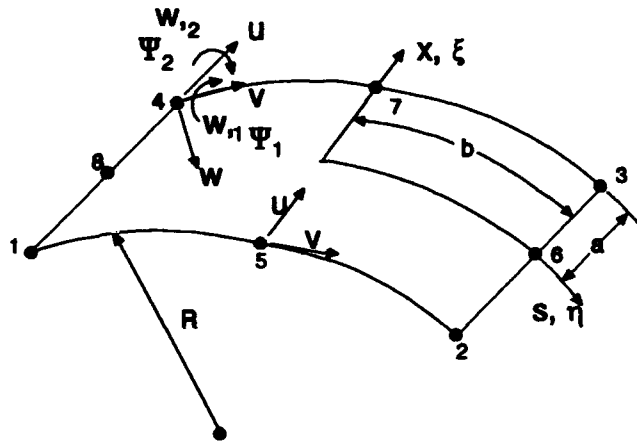


Figure 2.1. 36 DOF isoparametric shell element

where

•  $\xi = x/a$  and  $\eta = s/b$ , the curvilinear coordinates of the surface

- $u$  is the displacement in the  $x$  coordinate direction
- $v$  is the displacement in the  $s$  coordinate direction
- $w$  is the transverse displacement in the  $z$  coordinate direction
- $w_{,1}$  is the slope  $\delta w/\delta x$  at the node
- $w_{,2}$  is the slope  $\delta w/\delta s$  at the node
- $\Psi_1$  is the rotation of the normal to the shell midsurface in the  $x$  direction (about the  $s$  axis)
- $\Psi_2$  is the rotation of the normal to the shell midsurface in the  $s$  direction (about the  $x$  axis)

The general shell kinematics in orthogonal curvilinear coordinates are

$$\begin{aligned}
 u_1(\xi, \eta, \zeta) &= u \left( 1 - \frac{\zeta}{R_1} \right) + \zeta \Psi_1 + \zeta^3 k \left( \Psi_1 + \frac{w_{,1}}{\alpha_1} \right) \\
 u_2(\xi, \eta, \zeta) &= v \left( 1 - \frac{\zeta}{R_2} \right) + \zeta \Psi_2 + \zeta^3 k \left( \Psi_2 + \frac{w_{,2}}{\alpha_2} \right) \\
 u_3(\xi, \eta) &= w
 \end{aligned} \tag{1}$$

or

$$\begin{Bmatrix} u_1(\xi, \eta, \zeta) \\ u_2(\xi, \eta, \zeta) \\ u_3(\xi, \eta, \zeta) \end{Bmatrix} = [R] \begin{Bmatrix} u(\xi, \eta) \\ v(\xi, \eta) \\ w(\xi, \eta) \\ w(\xi, \eta)_{,1} \\ w(\xi, \eta)_{,2} \\ \Psi_1(\xi, \eta) \\ \Psi_2(\xi, \eta) \end{Bmatrix}$$

where  $k = -4/(3h^2)$ .  $\xi$  and  $\eta$  are in the natural coordinates and  $\zeta$  is the coordinate along the mid-surface normal.  $[R]$  is a matrix that is a function of  $\zeta$  only. For a cylinder,  $\zeta/R_1=0$ . For a flat plate,  $\zeta/R_1$  and  $\zeta/R_2$  are both 0.  $R_1$  and  $R_2$  are shell radii in the  $\zeta$

and  $\eta$  coordinate directions respectively.

The strains are defined as

$$\epsilon_{ij} = \frac{\gamma_{ij}}{h_i h_j} \quad (2)$$

where  $\gamma_{ij}$  is the Green's strain tensor and  $h_i$  are scale factors (19:594). Insertion of equation (1) into equation (2) results in strain equations with many linear and nonlinear terms. In this investigation only the linear terms of strains  $\epsilon_{44}$  and  $\epsilon_{55}$ , are retained. Palazotto and Dennis (14) included transverse shear flexibility in the Donnell and Von Karman strain equations. The in-plane modified Donnell (14:63) strain equations for cylindrical shells are

$$\begin{aligned} \epsilon_{11} &= u_{1,1} + \frac{1}{2} w_{,1}^2 \\ \epsilon_{22} &= u_{2,2} - \frac{w}{R_2} + \frac{1}{2} w_{,2}^2 \\ \epsilon_{66} &= u_{1,2} + u_{1,2} + w_{,1} w_{,2} \end{aligned} \quad (3)$$

and utilize the kinematic terms of equation (1). The modified Von Karman plate equations are similar except  $w/R_2$  is zero. The transverse shear equations, after linearizations, are

$$\begin{aligned} \epsilon_{44} &= w_{,2} + \psi_2 + \zeta^2 3k(w_{,2} + \psi_2) \\ \epsilon_{55} &= w_{,1} + \psi_1 + \zeta^2 3k(w_{,1} + \psi_1) \end{aligned} \quad (4)$$

Shape functions are used to relate the  $u(\xi, \eta)$  and  $v(\xi, \eta)$  to the values of  $u$  and  $v$  at

each node of the element.

$$\begin{Bmatrix} u(\xi, \eta) \\ v(\xi, \eta) \\ w(\xi, \eta) \\ w(\xi, \eta)_{,1} \\ w(\xi, \eta)_{,2} \\ \psi_1(\xi, \eta) \\ \psi_2(\xi, \eta) \end{Bmatrix} = [N] \{U_j^{(0)}\} \quad (5)$$

where  $[N]$  is a matrix of shape functions.  $\{U_j^{(0)}\}^T = \{u \ v \ w \ w_{,1} \ w_{,2} \ \psi_1 \ \psi_2\}_j$  for  $j= 1, 2, 3, 4$  and  $\{U_j^{(0)}\}^T = \{u \ v\}_j$  for  $j=5, 6, 7, 8$ . Quadratic shape functions are used to relate the  $u(\xi, \eta)$  and  $v(\xi, \eta)$  to the values of  $u$  and  $v$  at each node. Linear Lagrangian shape functions are used to relate  $\psi_1(\xi, \eta)$  and  $\psi_2(\xi, \eta)$  to the values of  $u$  and  $v$  at each node. Hermitian shape functions are used to relate the  $w(\xi, \eta)$  to the values of  $w$ ,  $w_{,1}$ , and  $w_{,2}$  at each corner node. See (14:83).

The equation of motion is derived using the Hamilton principal where the variation in the time integral of the total energy is set to zero:

$$\delta \int_{t_1}^{t_2} (E - T - W_e) dt = 0 \quad (6)$$

where  $E$  is the internal strain energy, the work of nonconservative forces, and the work of body forces.  $T$  is the kinetic energy and  $W_e$  is the external work. The virtual work for a laminated plate and shell are

$$\delta E = \int_{\Omega} \sum_{k=1}^L \int_{\zeta_{k-1}}^{\zeta_k} (\sigma_y^{(k)} \delta e_y^{(k)} + c^{(k)} v_j^{(k)} \delta u_j^{(k)} + P_j^{(k)} \delta u_j^{(k)}) d\zeta d\Omega \quad (7)$$

$$\delta W_e = \int_{\Omega} F_j \delta u_j d\Omega = 0 \quad (8)$$

$$\delta T = \int_{\Omega} \sum_{k=1}^L \int_{\zeta_{k-1}}^{\zeta_k} \{ \rho^{(k)} v_j^{(k)} \delta v_j^{(k)} \} d\zeta d\Omega \quad (9)$$

where  $i, j = 1 - 3$ ,  $\zeta_{k-1}$  and  $\zeta_k$  are positions at the top and bottom of the  $k$ th layer,  $\Omega$  is the domain of the mid surface,  $\sigma_{ij}^{(k)}$ ,  $\delta_{ij}^{(k)}$ ,  $P_i^{(k)}$ ,  $\delta u_j^{(k)}$ ,  $v_j^{(k)}$ ,  $\rho^{(k)}$ , and  $c^{(k)}$  are the stress tensor, virtual strain tensor, body force vector, virtual displacement vector, velocity vector, mass density, and damping coefficient for the  $k$ th layer respectively.  $F_j$  is the external force vector.  $L$  denotes the number of layers in the laminate.

The dynamic equation of motion can be derived from (6).

$$M U^{(2)} + C U^{(1)} + K(U^{(0)}) U^{(0)} = P(t) \quad (10)$$

$U^{(2)}$ ,  $U^{(1)}$  and  $U^{(0)}$  are acceleration, velocity, and displacement vectors respectively at each nodal point.  $P(t)$  is the external load applied to each point.  $K$  can be stated as:

$$K(U^{(0)}) = \left( K_0 + \frac{K_1(U^{(0)})}{2} + \frac{K_2(U^{(0)})}{3} \right) \quad (11)$$

where  $K_0$  is a constant stiffness matrix,  $K_1$  is a stiffness matrix related to linear displacement, and  $K_2$  is a stiffness matrix related to quadratic displacement. The consistent mass matrix is obtained by substituting equation (1) into equation (9) and integrating by parts to obtain

$$M = \int_{\Omega} \sum_{k=1}^L \int_{\zeta_{k-1}}^{\zeta_k} \rho^{(k)} [N]^T [R]^T [R] [N] d\zeta d\Omega \quad (12)$$

The damping matrix is obtained in a similar manner; however, for this research, no

damping is considered. However for completeness, damping terms will be carried through the development below.

## 2.2 Numerical Technique

Solution of the dynamic equation is accomplished through the Newton-Raphson and Beta-m methods. The Beta-m method (7) is a generalization of the Newmark time marching integration scheme. The Beta-m method transforms equation (10) into a set of nonlinear algebraic equations where the loading at each point at a given time is known. A Newton-Raphson iteration method is then used to solve these equations.

The Beta-m method has some important advantages for numerical computation. First, it is a single step method and therefore requires only the latest data from the previous time step. Second, the method is general; the differential equation determines the method order  $m$  and the user selects  $m$  integration parameters  $\beta_0, \beta_1, \dots, \beta_{m-1}$ . These  $\beta_i$  selections influence stability and accuracy of the particular algorithm chosen to solve the differential equation. Third, the finite difference scheme is not required. The beta-m method is defined by

$$U_{n+1}^{(k)} = q_k + b_k \Delta U^{(m)} \quad (13)$$

where

$$q_k = \sum_{j=k}^m U_n^{(j)} h^{j-k} / (j-k)!, \quad (14)$$

and

$$b_k = \beta_k h^{m-k} / (m-k)!, \quad (15)$$

where  $k = 0, 1, \dots, m$  and  $h$  is the time increment. For this research,  $\beta_0 = 0.5$ ,  $\beta_1 = 0.5$ ,

and  $\beta_2 = 1.0$ .

Substitution of (13) into (10) at time  $t_{n+1}$  results in

$$[b_2 M + b_1 C + b_0 K(q_0 + b_0 \Delta U^{(m)})] \Delta U^{(m)} = P_{n+1} - \{M q_2 + K(q_0 + b_0 \Delta U^{(m)}) q_0\} \quad (16)$$

Equation (16) is a set of nonlinear algebraic equations which may be solved by various algorithms. A Newton-Raphson iterative method is used in the DSHELL code. At each time step

$$\Delta U_{i+1}^{(m)} = \Delta U_i^{(m)} + \delta \Delta U_i^{(m)} \quad (17)$$

where  $i$  is the iteration number. Insertion of equation (17) into (16) results in

$$\begin{aligned} [b_2 M + b_1 C + b_0 K_T(q_0 + b_0 \Delta U_i^{(m)})] \delta U_i^{(m)} = P_{n+1} \\ - M\{q_2 + b_2 \Delta U_i^{(m)}\} - C\{q_1 + b_1 \Delta U_i^{(m)}\} - K(q_0 + b_0 \Delta U_i^{(m)})\{q_0 + b_0 \Delta U_i^{(m)}\} \end{aligned} \quad (18)$$

where  $K_T(U^{(0)})$  is a tangential stiffness matrix at deformation state  $U^{(0)}$ , which is

$$K_T(U^{(0)}) = K_0 + K_1(U^{(0)}) + K_2(U^{(0)}) \quad (19)$$

Equation (18) is solved by the following algorithm:

- (1) Given  $U_n^{(0)}, U_n^{(1)}, \dots, U_n^{(m)}$  at time  $t_n$ , we seek solutions at  $t_{n+1}$ .
- (2) Calculate  $q_0, q_1, \dots, q_m$  from equation (14).
- (3) Given  $\Delta U_i^{(m)}$  and  $U_{n+1}^{(0)}$  from the  $i$ th iteration, we obtain the right hand side of equation (18) and update the tangential stiffness matrix from (19).
- (4) Solve for the unknown,  $\delta U_i^{(m)}$  from equation (18).
- (5) Calculate the update of solution vector  $U_{i+1}^{(m)}$  from equation (17).

(6) Update  $U_{n+1}^{(0)}, U_{n+1}^{(1)}, \dots, U_{n+1}^{(m)}$ , for the  $(i + 1)$ th iteration from equation (13).

(7) If

$$\frac{\left\{ \sqrt{\sum_{l=1}^L (U_{n+1}^{(0)})^2_l} \right\}_{i+1} - \left\{ \sqrt{\sum_{l=1}^L (U_{n+1}^{(0)})^2_l} \right\}_i}{\left\{ \sqrt{\sum_{l=1}^L (U_{n+1}^{(0)})^2_l} \right\}_i} \leq \varepsilon \quad (20)$$

for a specified convergence criteria  $\varepsilon$ , then step (1) is repeated for the next time step, otherwise step (3) is repeated until equation (20) is satisfied. The value of  $l$  is the degree of freedom (dof) number and  $L$  is the total number of dof.

### 2.3 Chaos

"*Chaotic* is a term assigned to that class of motions in deterministic physical and mathematical systems whose time history has a *sensitive dependence on initial conditions*" (10:4). Moreover, in contrast to random motion, there are no unpredictable inputs or parameters in a system that is classified as chaotic. Linear systems cannot exhibit chaotic vibrations (10:39); the system must have nonlinear features. In mechanical systems, there are several possible ways for nonlinearities to exist and thus the potential for chaotic behavior to occur. For example, nonlinearities may exist in elastic elements, damping, material properties, geometric relations, boundary conditions, backlash, play, etc. In this research, the mechanical system is elastic with nonlinear geometric effects arising from large displacements and moderately large rotations.

There are several methodologies available to indicate the presence of chaotic

behavior. For this work, the following methods are considered:

- Observation of phase-plane histories
- Fourier spectrum analysis
- Poincaré maps
- Calculation of *Lyapunov* exponents

The motion of some given feature of a mechanical system subjected to excitation may be displayed in terms of a dimensional phase-plane history. For example, a plot of velocity  $\dot{x}^{(1)}(t)$  versus position  $x^{(0)}(t)$  (a classic phase-plane plot) of some point on a mechanical system represents a two-dimensional map. If this point on the system were in an equilibrium state, the phase plane history would appear as a point; for periodic motion, the trajectory map would appear as a closed curve; for quasiperiodic motion, the trajectory map may be plotted as a surface in three-dimensional space. For chaotic systems, the phase-plane history tends to consist of orbits whose trajectories tend to fill up a portion of the phase space. A *pseudo-phase-plane* map also yields similar results for all of the types of systems discussed. A pseudo-phase-plane map (also known as the *embedding space method*) plots  $q(t + \Delta t)$  versus  $q(t)$  where  $q$  is some system variable. This method is particularly useful when only one variable is measured. The idea is that the signal  $q(t + \Delta t)$  is related to its time derivative and should exhibit properties similar to the classic phase plane display.

Another clue to detecting chaotic vibrations is the presence of a broad spectrum of frequencies in a signal analysis. The fast Fourier transform is a popular method to decompose a signal into a set of sinusoidal or harmonic signals. It is assumed that any signal may be represented as a function

$$f(t) = \frac{1}{2\pi} \int_{\Gamma} F(\omega) e^{i\omega t} d\omega \quad (21)$$

where  $e^{i\omega t} = \cos \omega t + i \sin \omega t$  and  $\Gamma$  is a path along a the complex plane  $\omega$ . However, calculation of equation (21) is not efficient. Fast Fourier transform algorithms are typically used when data sets composed of discrete points are to be processed. The fast Fourier transform is defined by

$$T(J) = \sum_{I=1}^N f(I) e^{-2\pi i(I-1)(J-1)/N} \quad (22)$$

where  $I$  and  $J$  are integers. Moon (10:149) indicates that a typical frequency spectrum plot may consist of many closely grouped frequency spikes, over a broad frequency range, that gradually diminish in strength as the frequency increases.

A qualitative feature of a phase-plane map useful in the study of chaotic systems is the Poincaré map or section. A Poincaré map consists of a sampling of points in a dimensional map at some predetermined interval of time or space. For example, if one establishes planes at even intervals of time in a phase-plane trajectory and maps those points (where the trajectories intersect the planes) onto a single plane, a Poincaré map is formed. For a forced vibration systems, Moon (10:50) has recommended that for a plot of velocity  $\dot{x}^{(1)}(t_n)$  versus position  $x^{(0)}(t_n)$ ,

$$t_n = nT + \tau_0 \quad (23)$$

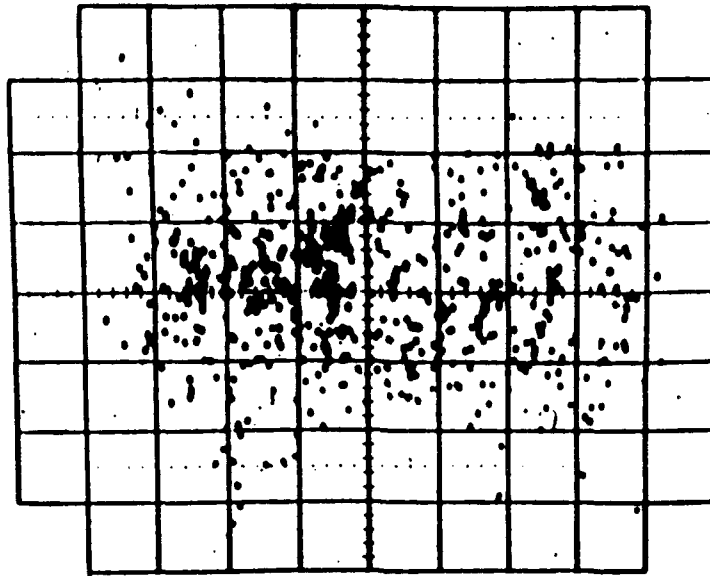
where  $T$  is the period of the driving motion,  $\tau_0$  is a delay time which is generally some fraction of the period  $T$  (See Wolf (27)), and  $n$  is an integer. For harmonic systems, the Poincaré map would appear as distinct and finite points, the number of points dependent

on the parameters chosen in equation (21). For chaotic systems, the Poincaré map may consist of an arrangement of points whose appearance depends on the type of system involved. For systems with little or no damping, the Poincaré map often appears as a cloud of unorganized points in the phase plane; Figure 2.2a is an example. For chaotic systems with dissipation involved, the map often appears as a structure with "an infinite set of highly organized points arranged in what appears to be parallel lines" (10:53). Figure 2.2b is an example of a Poincaré map exhibiting fractal patterns which are associated with *strange attractors*. An *attractor* is a set of points or a subspace toward which a time history approaches after transients die out. For example, for equilibrium in which no motion is present, a Poincaré map would be a single point since the phase-plane trajectory would pierce all phase planes, in the same location on that plane, for all times.

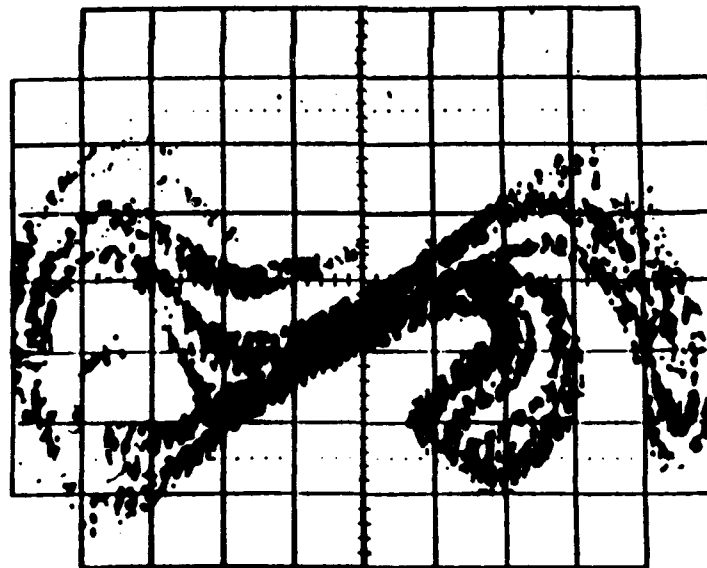
One quantitative measure of chaotic motion is the calculation of the *Lyapunov* exponent. In general, the initial conditions of a dynamical system may be thought to reside in an infinitesimal sphere of diameter  $d_0$  in a phase space. Chaotic trajectories are considered to map the sphere into an ellipsoid whose major axis changes according to:

$$d = d_0 2^{\lambda(t-t_0)} \quad (24)$$

where  $\lambda$  is the Lyapunov exponent. For periodic or harmonic motion,  $\lambda$  will be less than or equal to 0. For chaotic motion,  $\lambda$  is positive. However, small amounts of data are not sufficient to determine if chaotic motion is present. One method averages several data values over a different regions of the phase space. Wolf (27:295) proposed the following algorithm:



(a)



(b)

**Figure 2.2** (a) Poincaré map of chaotic motion of a buckled beam with low damping. (b) Poincaré map of chaotic motion of a buckled beam for higher damping showing fractal-like structure from a strange attractor (from Moon (10:51)).

$$\lambda = \lim_{N \rightarrow \infty} \frac{1}{N} \sum_1^N \frac{1}{(t - t_0)} \ln_2 \frac{d_i}{d_0^i} \quad (25)$$

where  $N$  corresponds to the number of replacement steps (intervals) in a set of discrete data points. An excellent explanation of the process along with a computer algorithm is provided in the aforementioned reference.

### III PROCEDURES

In this research, shells of various radii were subjected to stepwise transverse point loads. Figure 3.1 shows an example of a cylindrical shell and its hinged boundary;  $h$  is the depth of the shell and  $c$  is the chord length. The curved edges (arc lengths) are free and have a fixed length of 12 inches, while the straight edges are hinged and have a length of 18 inches. However, with the arc lengths fixed and radii prescribed, the curvilinear shape of any cylindrical shell may be described as a ratio of the depth to the chord length as long as the thickness and lengths remain proportional to the other dimensions.

The transverse point load is applied in a step-wise fashion to shells of various radii. Figure 3.2 illustrates the loading curves applied to the center node. The initial loading rate was held constant at  $1.4 \times 10^6$  lbs/s for all cylindrical shells. This loading rate was the same value used by Taylor (24) and Greer (6). Cylindrical shell radii of 4, 6, 8, 12, 20, 60 inches were considered. Figure 3.3 shows the various cylindrical shell geometries considered. A flat plate was simulated by increasing the radius to an arbitrarily large value of 900,000 inches. Figure 3.4 shows the flat plate mesh. In all cases, the longitudinal lengths of the composite is 18 inches. The maximum load level for each shell was chosen as the static collapse load for that shell. The SHELL (14) computer code was used to calculate this load. Chien and Palazotto (2) showed that the non-linear static equilibrium load that causes buckling predicts the upper bound solution of the dynamic buckling load. The collapse loads were determined by a finite element method using a displacement-increment method (14:131); that is, displacement is specified and the equilibrium load corresponding to that displacement is determined using Newton-

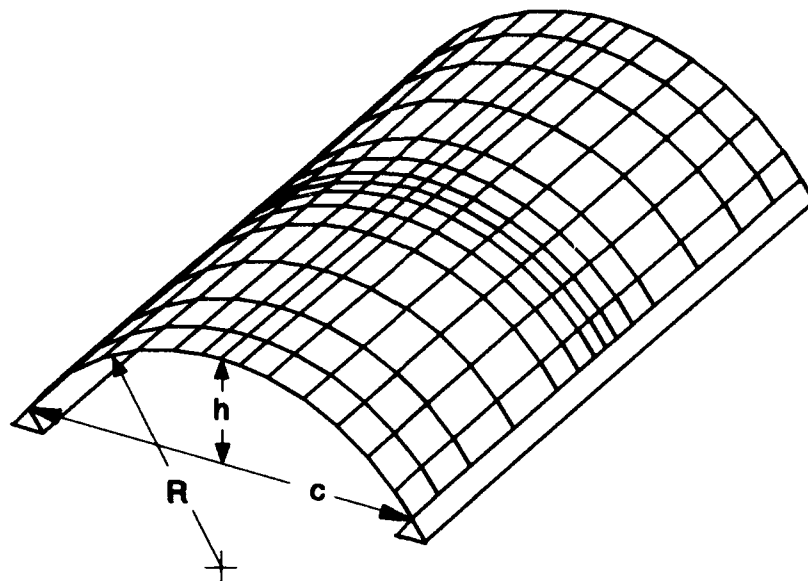


**Figure 3.1.** Composite cylindrical shell.

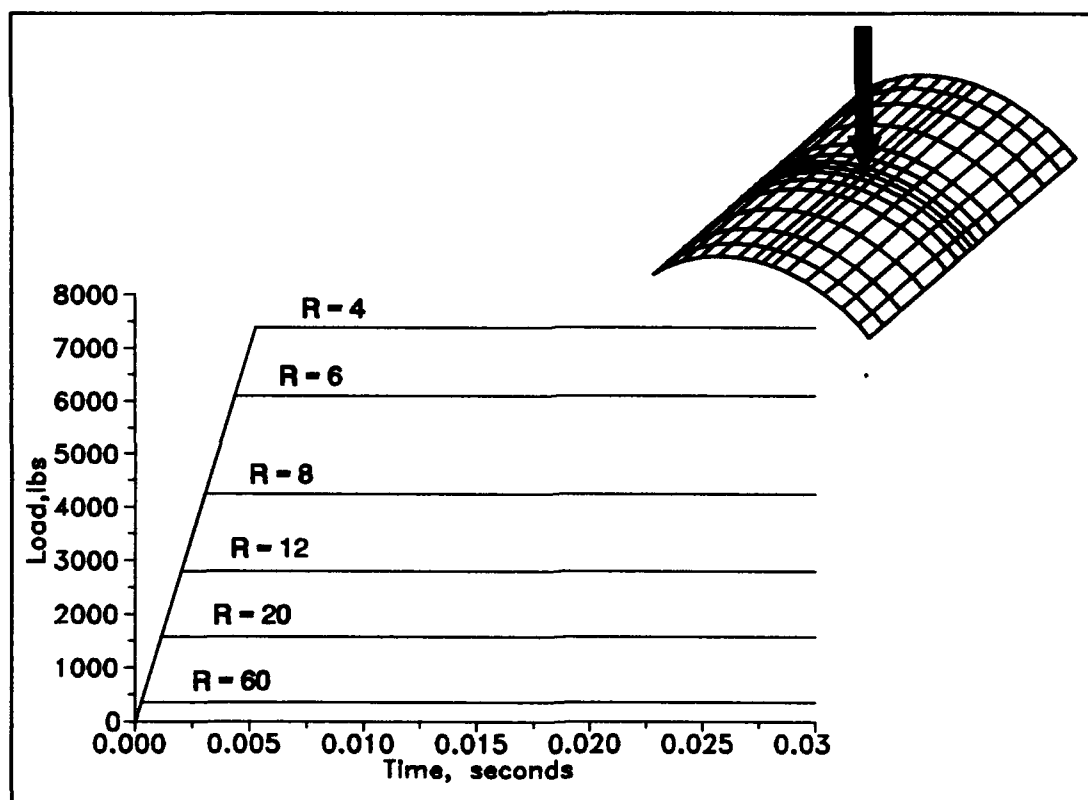
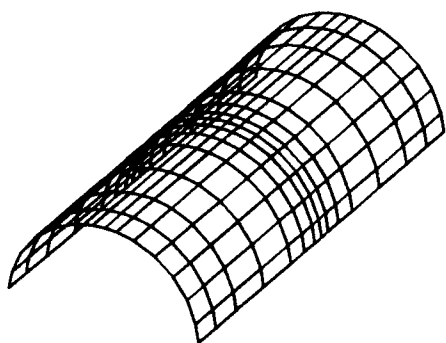
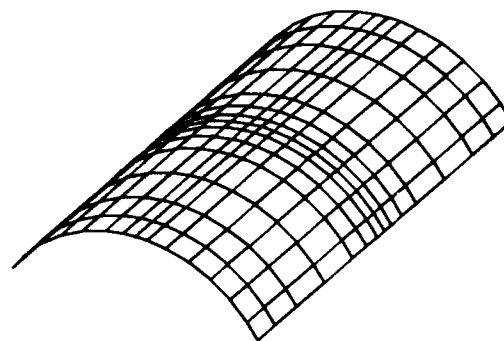


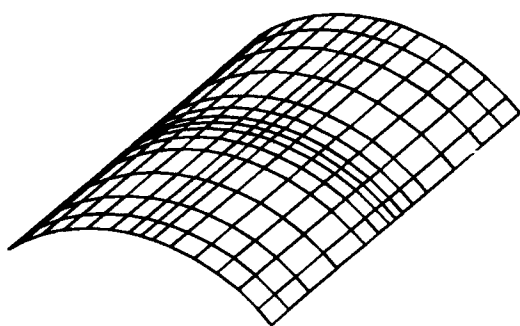
**Figure 3.2.** Loading curves applied to cylindrical shells of various radii.



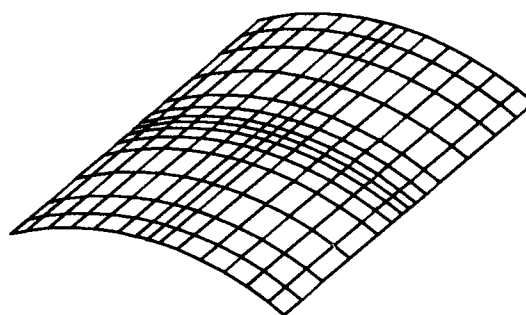
Radius = 4.0 in.



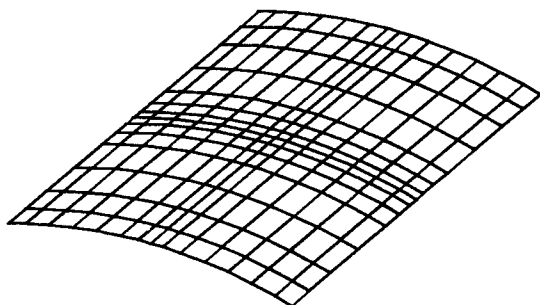
Radius = 6.0 in.



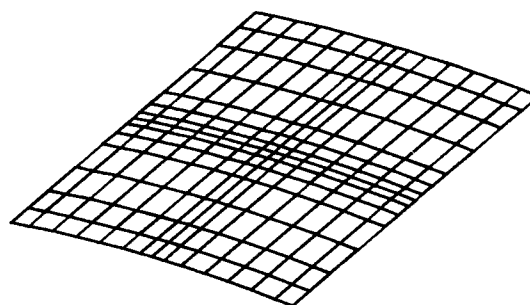
Radius = 8.0 in.



Radius = 12.0 in.



Radius = 20.0 in.



Radius = 60.0 in.

**Figure 3.3** Meshes representing cylindrical shells.

Raphson iteration. All in-plane nonlinear terms and linear transverse shear terms are used

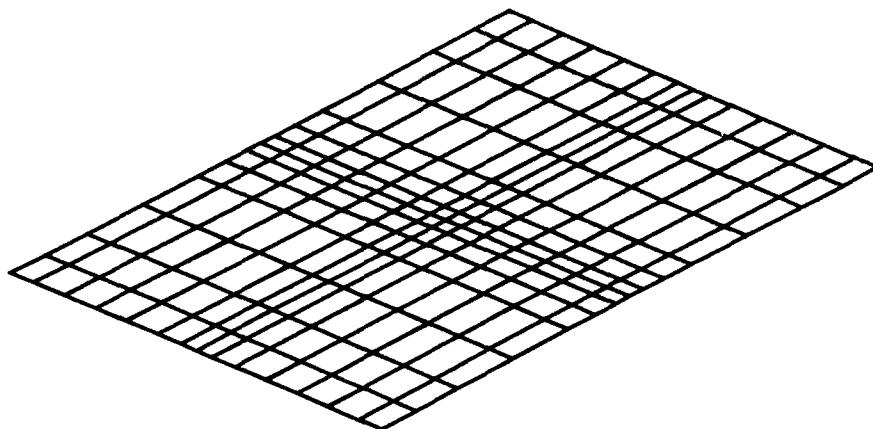


**Figure 3.4.** Mesh representing a flat plate.

in the formulation similar to the above. The SHELL [ ] program was used to determine the static collapse loads.

Due to the extensive computational resources (i.e., time and memory) required to run the finite element code, all shell configurations were limited to a 7x7 quarter element Taylor (24) mesh. When compared to finer Silva (22) meshes, the Taylor meshes fell within 5% of the criteria set forth by Silva based on peak loadings; thus the coarser mesh was deemed adequate to capture the general behavior of the shell as it collapses. Moreover, of the many possible degrees-of-freedom that could be analyzed, it is assumed that the generalized displacement associated with the degree-of-freedom of the load dominates the behavior of the system. Therefore, the center node displacements are of primary interest throughout this work.

The shell properties were modeled after a 24-ply, 0.12 inch thick, Hercules AS4-3501-6

[0<sub>2</sub>/90<sub>2</sub>], graphite epoxy. The material properties are listed in Table 3.1. The shell is assumed to behave in a perfectly elastic fashion with no interlaminar failure and no damping. The density is 0.00015088 slugs/in<sup>3</sup>.

In a dynamically loaded shell, the choice of time step and convergence tolerance is a crucial parameter for producing numerically stable results for the integrating scheme used in this research. In particular, the time step required to capture the behavior of the shell after buckling must be significantly smaller than the time step before collapse. For a 12 inch radius shell, Greer (6) determined that the time step required to capture the prebuckling behavior of the shell is approximately  $\tau_1/20$ , where  $\tau_1$  is the period (in seconds) of the first fundamental frequency determined from an eigenvalue analysis. Using this time step for post collapse analysis results in numerically unstable results. Numerical instability typically leads to erratic data or unbounded motion. The time step required for numerically stable results for the 12 in. radius shell was recommended to be  $\tau_2/160$ , where  $\tau_2$  is the period of the highest frequency experienced by a free edge node as the shell oscillates with an applied load that does not result in collapse; the value of  $\tau_2$  was determined by a fast Fourier transform analysis of the displacement data at the free edge node.

**Table 3.1.** Physical properties of AS4-3501-6 graphite epoxy composite (psi)

$E_1$	$E_2$	$G_{12}$	$G_{13}$	$G_{23}$	$\nu_{12}$
18.844(10 <sup>6</sup> )	1.468(10 <sup>6</sup> )	0.91(10 <sup>6</sup> )	0.91(10 <sup>6</sup> )	0.45(10 <sup>6</sup> )	0.26

In Greer's work, the value of  $\tau_2$  corresponded closely to the second natural frequency

period of the 12 in. radius cylindrical shell. Therefore, in an attempt to reduce the workload, the value of  $\tau_2$  in this research was initially chosen as the natural period corresponding to the second eigenvalue. The value of  $\tau/160$  was then rounded down to the nearest single significant digit. The DSHELL (26) computer code was used to determine the eigenvalues. Table 3.2 lists the first three natural frequencies.

**Table 3.2.** First three natural frequencies of composite cylindrical shells of varying radii

Radius (in.)	1st Frequency (Hz)	2nd Frequency (Hz)	3rd Frequency (Hz)
4	460	1339	1535
6	486	1070	1524
8	497	911	1520
12	505	757	1512
20	508	655	1251
60	479	547	699

TECPLOT™ was used to display mesh geometries. The output of the DSHELL program produces changes in the degree of freedom variables with respect to the original curvilinear coordinate system. Therefore, the new position may be found by algebraically adding the changes. In order for TECLOT™ to graph the results, a transformation from the curvilinear coordinate system to a Cartesian system is first required. For simplicity, only the displacement coordinates for the corner nodes (mid-side nodes have in-plane displacements only) were utilized for graphical display purposes. The transformation requires simple trigonometric relations. Simple computer algorithms were written and used to carry out the transformation.

#### IV RESULTS AND DISCUSSION

There are several objectives addressed in this research. A major objective is to observe any dynamic cylindrical shell behavior characteristics not noted in other similar studies with the DSHELL program. Another objective is to explore displacement and rotational limits under which the SLR and the modified Donnell may be applicable in a dynamics application for plate and cylindrical shell structures. Comparisons between the results predicted by the SLR and Donnell formulations are to be made. Numerical stability characteristics are also examined as the shell radius varies. One other goal is to demonstrate whether or not these point-loaded cylindrical shells exhibit chaotic motions at certain phases in the loading history.

Previous research has indicated that the SLR formulation for static analysis produces acceptable results when no more than approximately 15 percent of a shell structure undergoes up to 40 degrees of rotation (14). For these shells, maximum rotation would be expected to occur at the hinged boundaries. With these particular shell geometries, the 8 in. radius shell would be expected to be at or slightly above the limits of the maximum rotation after collapse if a static analysis was applied. Therefore, of the shells examined in this research, the behavior characteristics of the 8 in. radius cylindrical shell are considered first.

##### *4.1 Eight in. Radius Cylindrical Shell*

Figure 4.1 shows the center node displacement of the 8 in. radius cylindrical shell. Upon initial application of the load, both formulations show that there is an initial and nearly constant velocity increase. After approximately 1 in. of displacement, the center

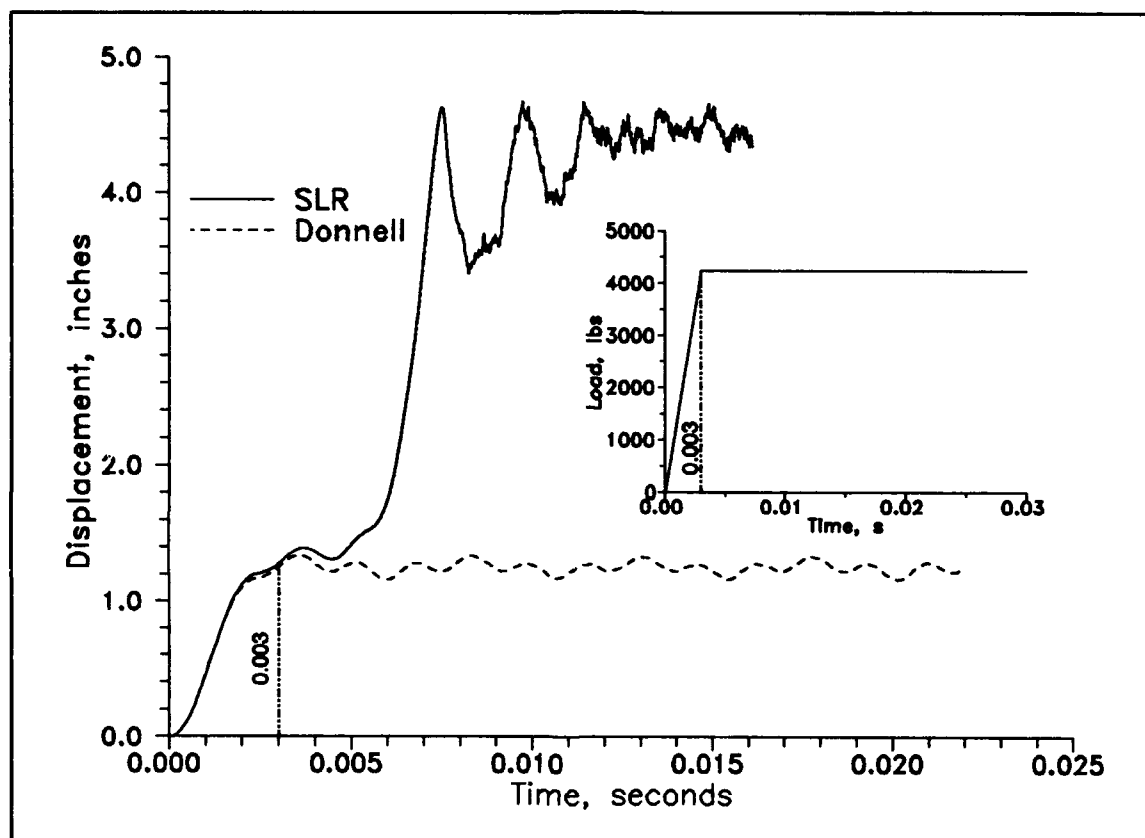


**Figure 4.1.** Center node displacements of composite cylindrical shells subjected to a transverse step load applied to the center. Radius = 8.

node of the SLR shell reduces its average velocity as the center node oscillates momentarily. Next, the SLR shell center node displacement rate increases dramatically. Globally, the entire displacement field undergoes a quick reversal defined as the snapping phenomenon (2:631). The Donnell shell does not snap and is discussed later on. Measurement of  $\Delta w/\Delta t$  from the graph indicates that the velocity of the center node reaches speeds in excess of 100 miles per hour when the shell snaps. Immediately after the shell reaches its maximum displacement, the center node enters into a state where it vibrates with an amplitude and period that decays over a short period and will be referred to as a *transient* phase in this paper. After the transient phase, the center node oscillates about an equilibrium point which is near the static equilibrium load. Kounadis noted similar displacement characteristics with his two-degree of freedom pendulum model (8).

Work has been done to define the point of dynamic instability of a system. Kounadis analyzed one and two-degree-of-freedom systems, with material nonlinearities (instead of geometric nonlinearities), subjected to step loading and defined dynamic buckling as "that state for which an escaped motion is initiated" (8). The escaped motion was associated with an angular degree of freedom with subsequent unbounded behavior over time. The sudden rise in velocity as indicated in Figure 4.1 is analogous to the escaped motion observed by Kounadis with the exception that unbounded motion is not observed nor expected. For this higher degree-of-freedom system, Chien and Palazotto (2) defined the inflection point on the displacement curve as the point where dynamic instability initiates for arches and cylindrical shells. A general discussion of this dynamic instability phenomenon from energy considerations may be found there. In short, the snapping phenomenon is a sudden transference of stored potential energy to kinetic energy at a

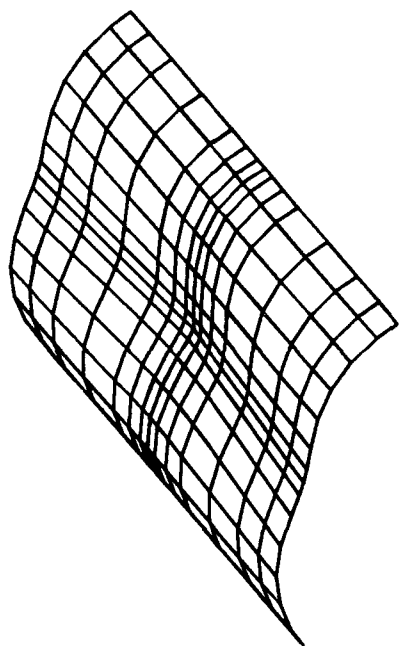
certain threshold level. This effect may be seen at the early part of the displacement history in Figure 4.1. Upon initial application of the load, there is an increase in velocity. Soon after, the average velocity decreases considerably while the peak load level is obtained; potential energy is stored. Continued load application eventually releases the stored energy.

It is interesting to note that the 8 in. radius shell does not initiate snapping until 0.0025s after the maximum load has been reached as indicated by the pairs of vertical lines in Figure 4.1. This delay is attributed to a period of dynamic instability that dominates the behavior even though the static collapse load level, which is sufficient for dynamic collapse, has been reached. Chien and Palazotto (2) showed that the onset of dynamic instability can be determined by comparing the behavior of a shell with a load that does not initiate collapse with the behavior of the same shell with a load that just initiates collapse. The onset of dynamic instability occurs at the point where the two displacement curves diverge. For the 8 in. radius shells, this divergence takes place at approximately  $t = 0.003$  which is coincident with the time when the maximum load has been achieved. The pre-collapsed behavior of the SLR shell is similar to the dotted curve in Figure 4.1. In general, the Donnell curves are slightly lower than the SLR curves in the pre-collapsed phases). Comparatively speaking, this period of dynamic instability for the 8 in. radius shell was more prolonged than the shallower arches and shells studied by Chien and Palazotto. Therefore, there appears to be a relation between the depth-to-chord ( $h/c$ ) ratio, namely that dynamic instability is expected to be more pronounced for shells with higher  $h/c$  ratios. However, the mechanism for the delay caused by the instability is not fully understood. Chien and Palazotto (2) have suggested that the dynamic

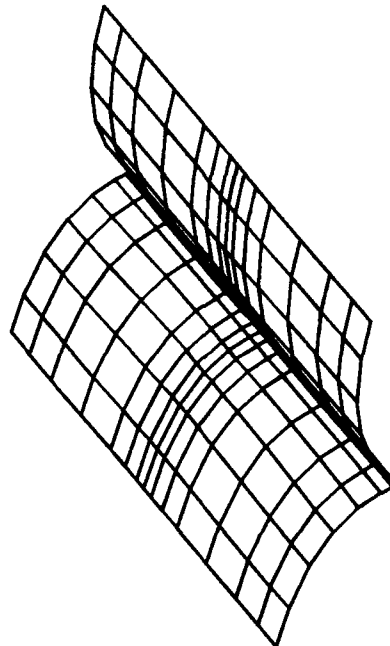
instability is associated with a dynamic coupling between the primary state function and a secondary state displacement state known as *parametric* resonance. Simitses (22) noted the potential for parametric resonance to occur in a suddenly loaded structure. That is, besides the motion produced by the forcing function, there may be other significant motions not necessarily in the direction as the forcing function. Evidence of this phenomenon is presented below.

Figure 4.2 shows a sequence of meshes that depict the composite shell at various times in the loading history. It should be also noted that the meshes represent the datum surface of the composite. The meshes displayed generally correspond to significant points on the center node displacement curve, i.e., the inflection point, local maxima and minima during the transient phase, and the later stages. The figure shows that an initial dimpling takes place followed by the formation of a deep crease along the longitudinal direction. Very soon after, the shell reaches a maximum displaced state in a very short time, i.e., the snapping phenomenon.

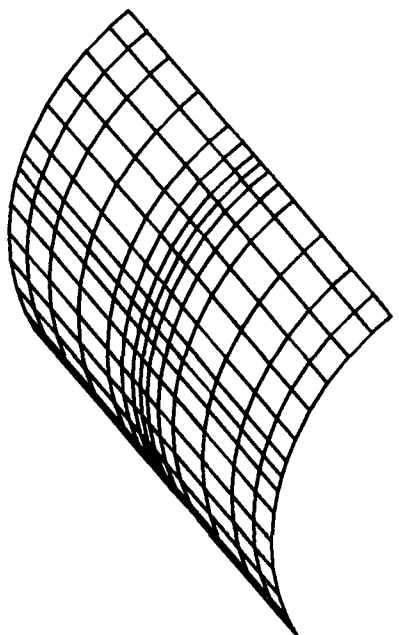
During the transient phase (approximately  $t=0.0075$  to  $0.014$  seconds), Figure 4.2 at  $t = 0.0085s$  shows that the free edges of the shell undergo secondary snapping motions. When the shell bottoms out, the nodal velocities are minimal and potential energy is stored. Since the center node is the only node that has direct loading, all other nodes are free to give up stored elastic energy, hence the secondary snapping. After the transients have stopped, the displacement field stays reversed with no further large displacements taking place. Vibratory motion in the  $w$  direction, after the transient phase has ceased, is apparent from Figure 4.1, but there are also in-plane parametric vibrations as well. The distorted mesh elements at the various times in Figure 4.2 is visual evidence of this idea.



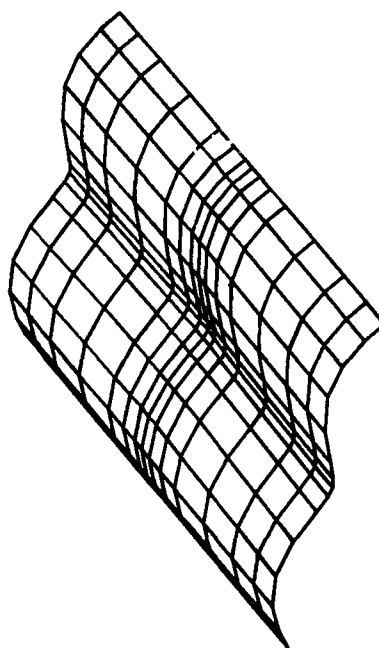
0.0045 seconds



0.0077 seconds

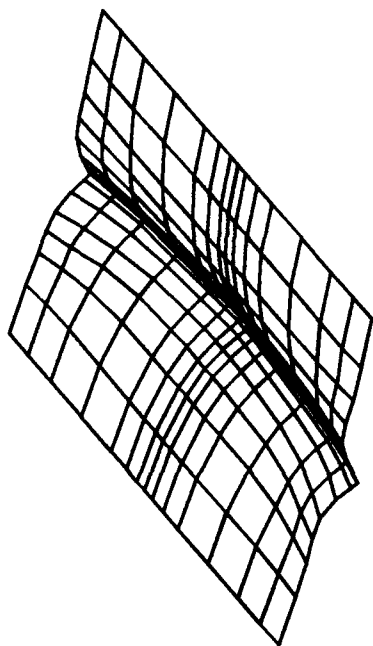


0.0 seconds

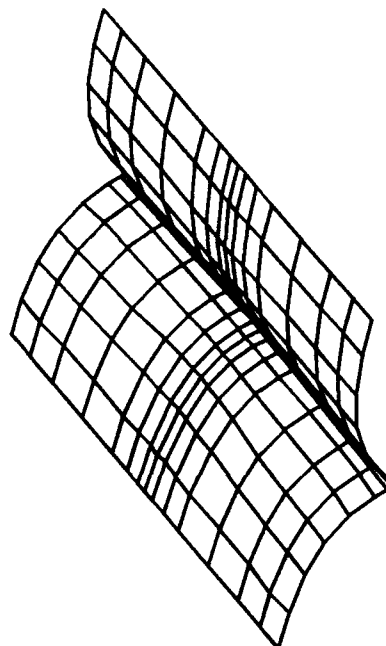


0.0065 seconds

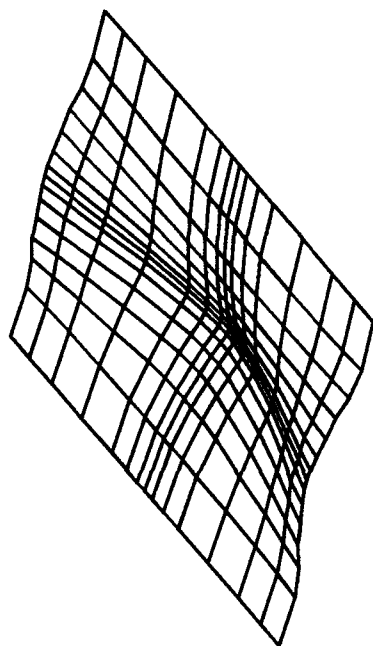
**Figure 4.2a.** Meshes representing a composite cylindrical shell subjected to a transverse step load applied to the center.  
Radius = 8 in., SLR formulation.



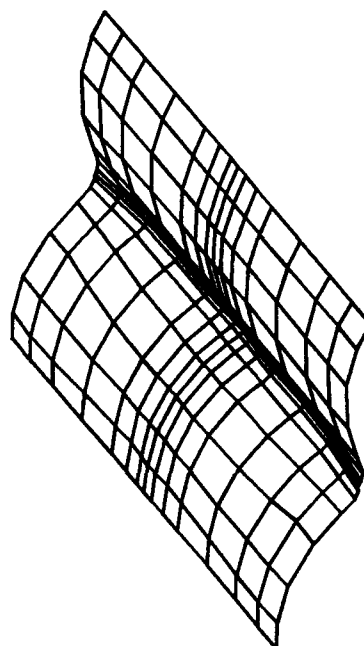
0.0100 seconds



0.0115 seconds



0.0085 seconds



0.0107 seconds

**Figure 4.2b.** Meshes representing a composite cylindrical shell subjected to a transverse step load applied to the center.  
Radius = 8 in., SLR formulation.

To further clarify this point, Figure 4.3 shows a 1" x 1" square element at various times in its loading history. In order to illustrate the changing shape of the element, the lower left corners of the elements are fixed to the same location, i.e., translation of the deformed element with respect to the undeformed element is removed. Figure 4.3a corresponds to times generally during the transient phase whereas Figure 4.3b corresponds to even intervals of time after the transient phase. Comparisons between the deformed and undeformed shell elements give a qualitative impression of the strain and stress fields as they change with time. In general, one would surmise that after collapse the elements closer to the hinged boundaries are primarily in a state of tension while the elements towards the middle are cycling between tensile and compressive states. A cursory examination of the shell elements also indicates that distortions are more evident in the  $v$  in-plane directions (circumferential) rather than the  $u$  directions. A check of the output data files for all of the shells studied indicates that  $u$  displacements are indeed minimal and may be due to rotational effects only. Since numerical models are ideal from a material and load applications standpoint, excitation of the shell in the longitudinal direction does not occur for the composite layup orientations considered.

The lower curve in Figure 4.1 is a result from the Donnell model. The curve indicates that the Donnell shell does not collapse despite the fact that the loading is the same as the SLR shell. Recall that the collapse load level was calculated with a static version of the SLR formulation. This result indicates that the Donnell shell has stiffer effective flexural characteristics than the higher-order formulation. It is believed that this higher stiffness is a by-product of the absence of higher-order terms in the formulation. At first glance, the Donnell shell goes primarily into a quasiperiodic oscillation mode;

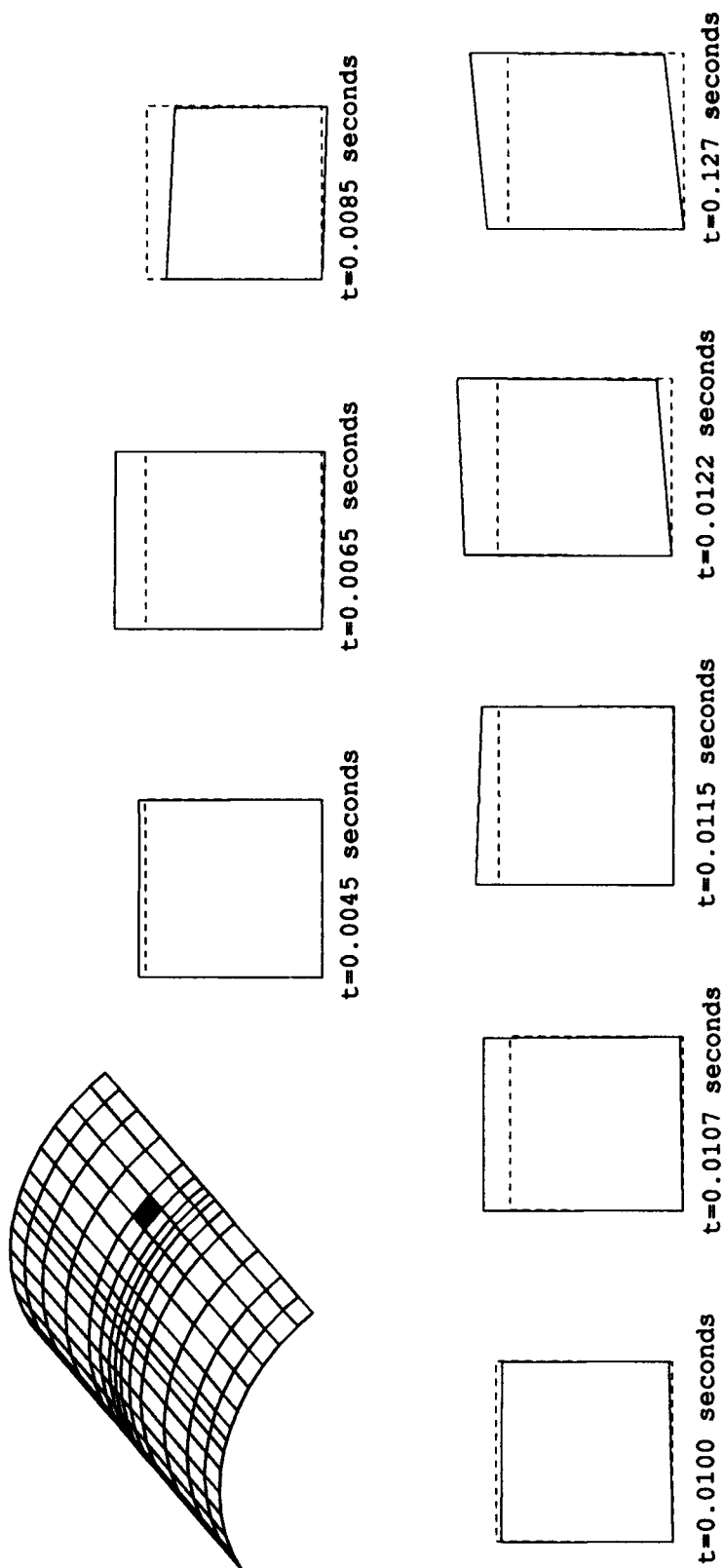


**Figure 4.3a.** Deformation of an element of a composite cylindrical shell subjected to a transverse step load applied to the center. Radius = 8 in., SLR formulation. Dotted lines correspond to the undeformed state.

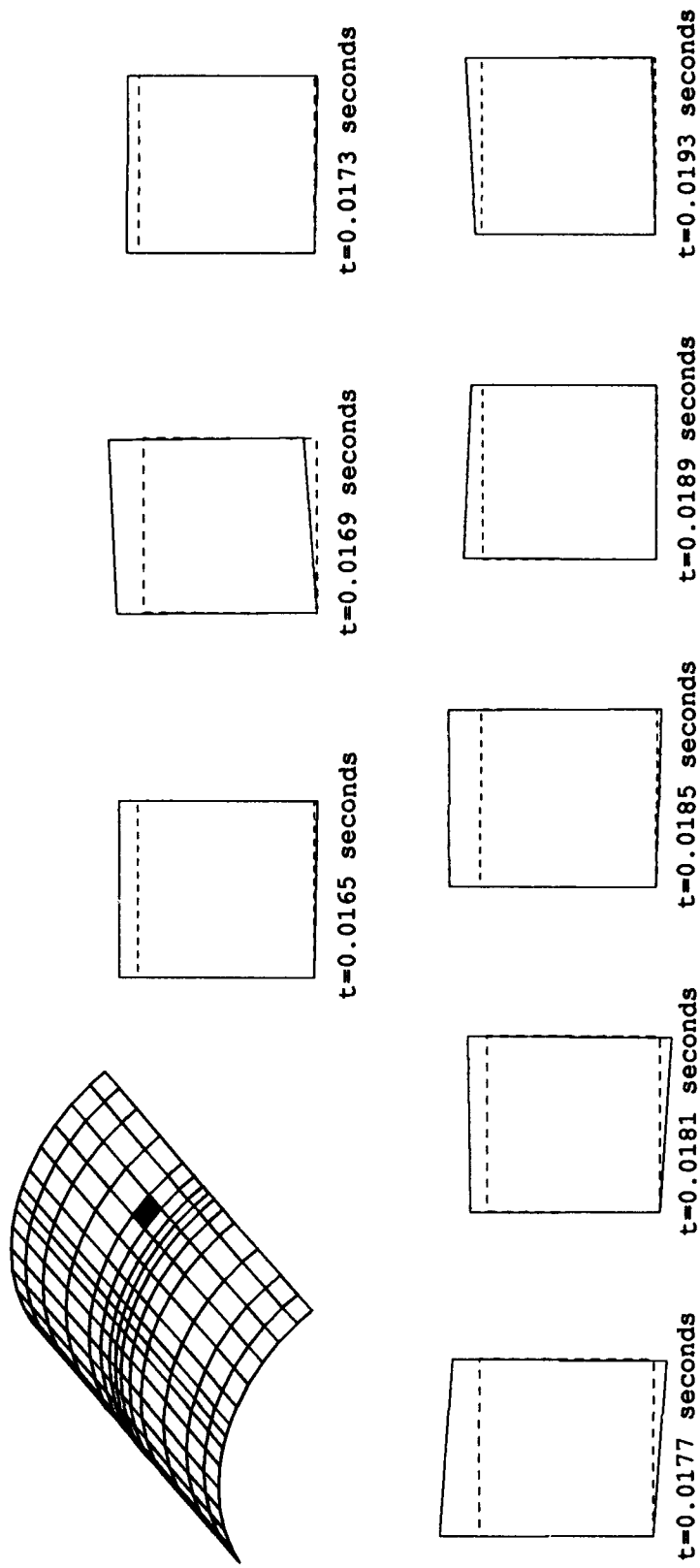


**Figure 4.3b.** Deformation of an element of a composite cylindrical shell subjected to a transverse step load applied to the center. Radius = 8 in., SLR formulation. Dotted lines correspond to the undeformed state.

however this is not the case as will be demonstrated in Section VI. A display of the deformed, uncollapsed mesh is not provided, but is similar to the precollapsed SLR mesh in Figure 4.2 at  $t = 0.0045s$ .

#### *4.2 Twelve in. Radius Cylindrical Shell*

Figures 4.4 and 4.5 show the center node displacement characteristics of a 12 in. radius cylindrical shell using both formulations. The curve characteristics of Figures 4.4 and 4.5 are similar to the SLR curve in Figure 4.1 in that there is an instability inflection point, a sudden increase in the velocity of the displacement field, a decaying transient period, and an oscillation about an equilibrium level. Unlike the 8 in. radius shell, both 12 in. radius shells collapse under the same loading history. It appears that either 1) the increase in the cylindrical radius has the effect of reducing the effective flexural stiffness (see Appendix A) of the Donnell shell to a level close to that of the SLR shell (recall that previous results indicate that the Donnell shell is stiffer than the SLR shell) or 2) the applied load is well beyond the levels required to cause collapse. In either case, there is a very small delay between the occurrence of the maximum load and the onset of snapping. This result is further evidence that the dynamic instability is related to the  $h/c$  ratio which in turn, is related to the stiffness properties of the shell.

Figures 4.6 and 4.7 show a sequence of meshes depicting the 12 in. radius shell as it deforms. The similarities between the mode shapes of the two sets of figures are also apparent and indicate the good agreement between the SLR and Donnell models for this shell geometry. The primary difference between Figures 4.6 and 4.7 is in the transient phase following the shell collapse. The transient phase of the SLR shell has a decaying

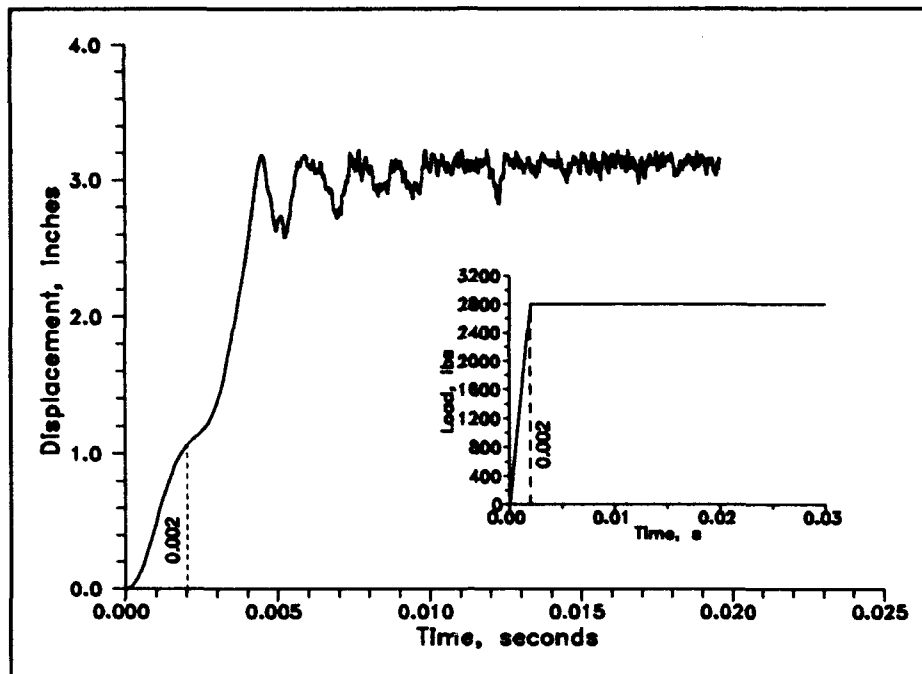


**Figure 4.4.** Center node displacement of a composite cylindrical shell subjected to a transverse step load applied to the center. Radius = 12 in., SLR formulation.

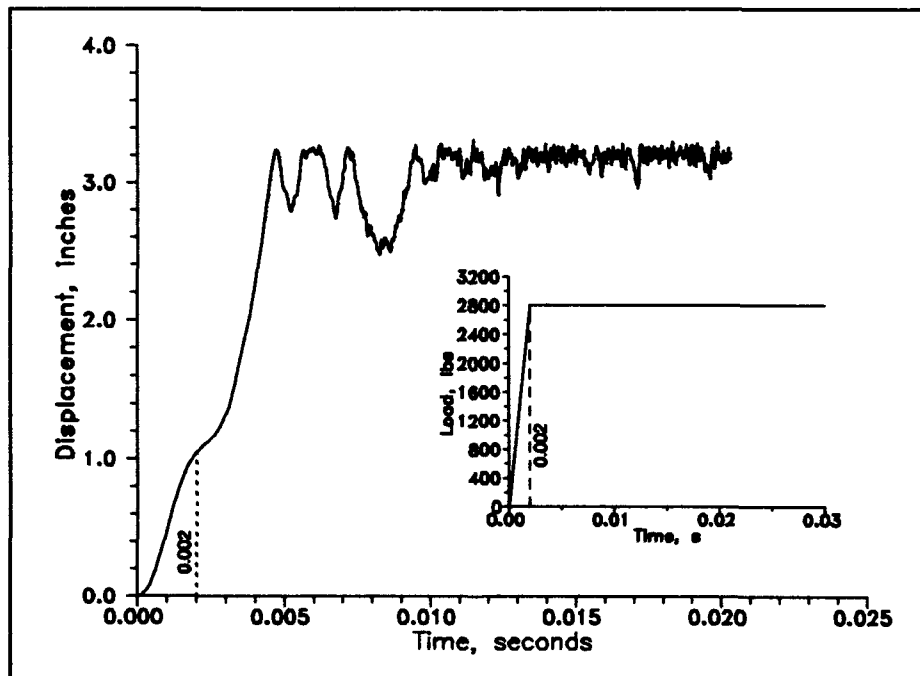
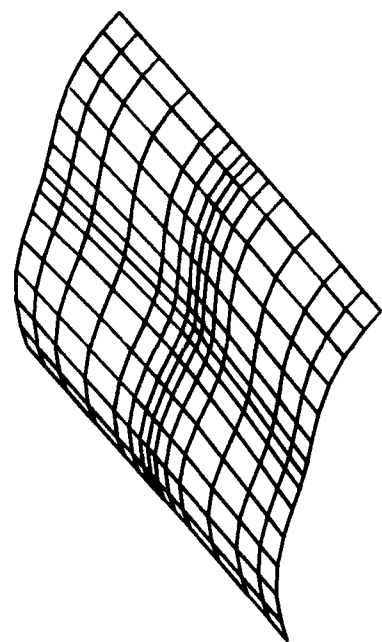
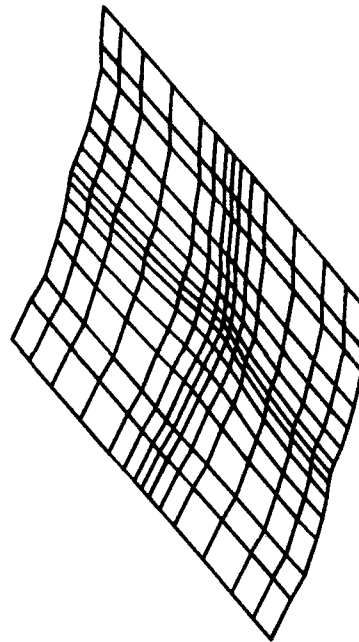


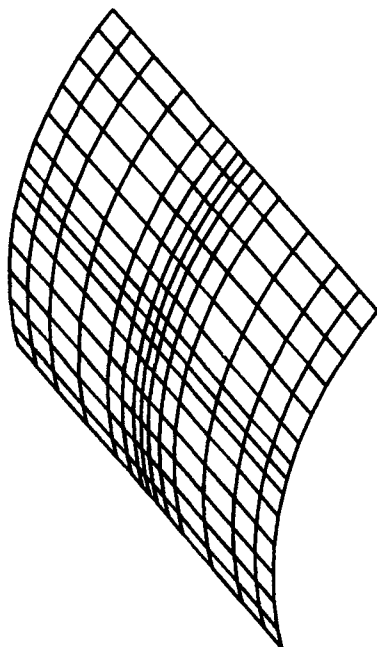
**Figure 4.5.** Center node displacement of a composite cylindrical shell subjected to a transverse step load applied to the center. Radius = 12 in., Donnell formulation.



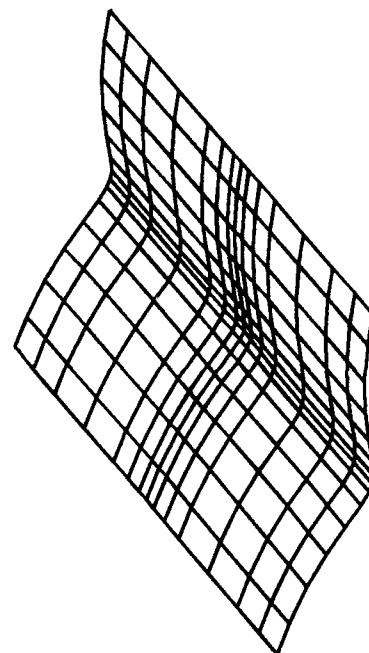
0.0030 seconds



0.0050 seconds

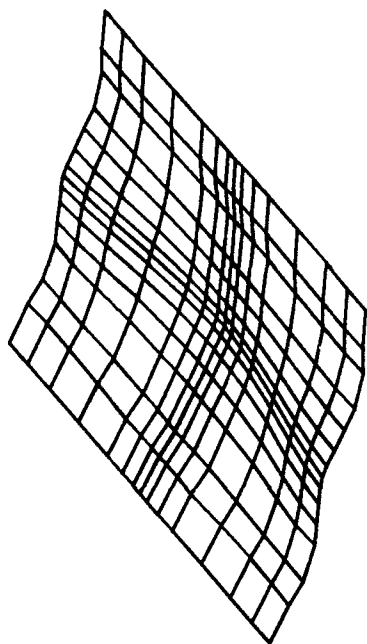


0.0 seconds

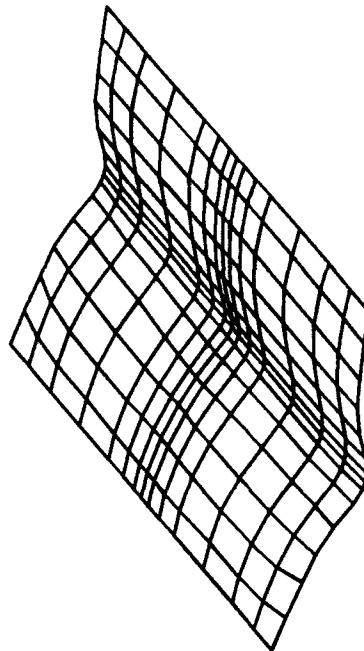


0.0045 seconds

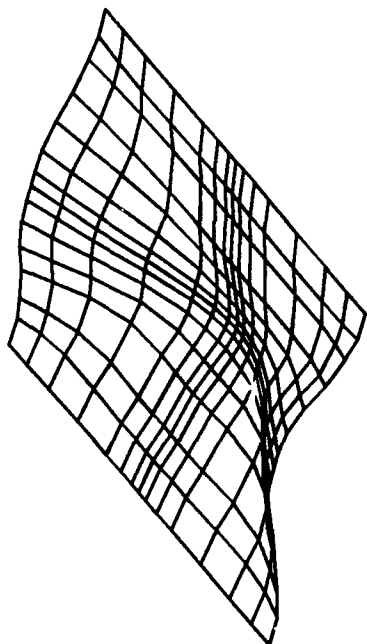
**Figure 4.6a.** Meshes representing a composite cylindrical shell subjected to a transverse step load applied to the center.  
Radius = 12 in., SLR formulation.



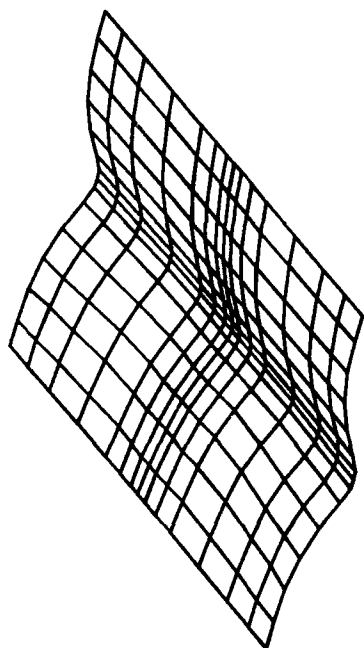
0.0070 seconds



0.0085 seconds

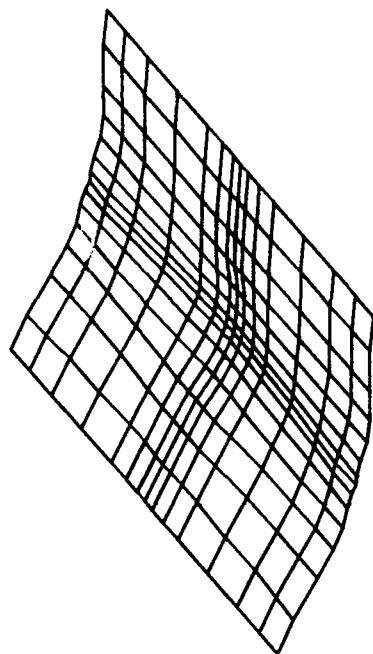


0.0060 seconds

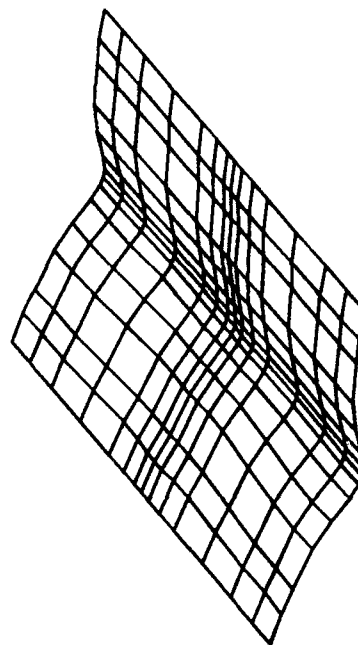


0.0080 seconds

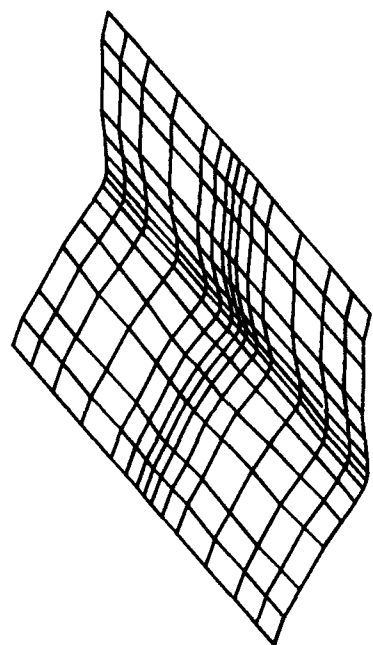
**Figure 4.6b.** Meshes representing a composite cylindrical shell subjected to a transverse step load applied to the center.  
Radius = 12 in., SLR formulation.



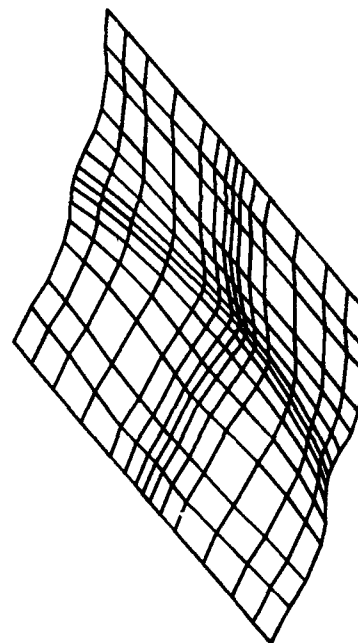
0.0095 seconds



0.0114 seconds

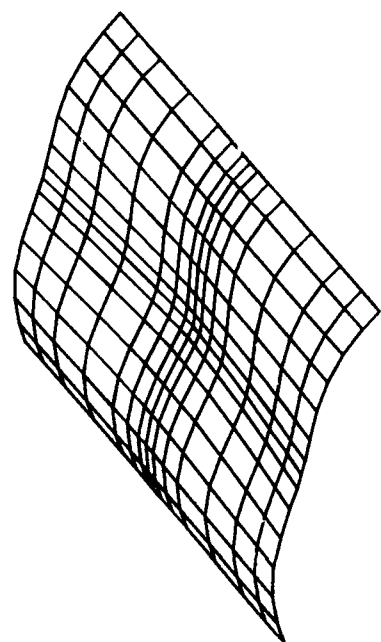


0.0090 seconds

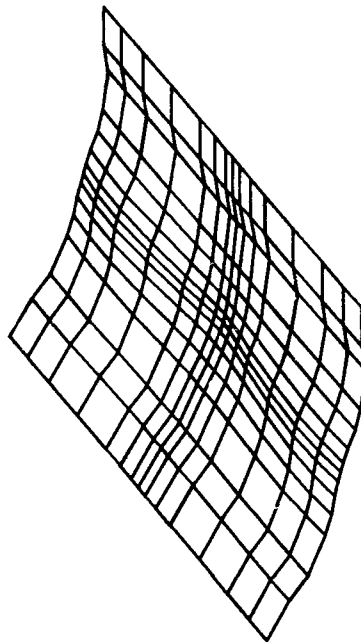


0.0105 seconds

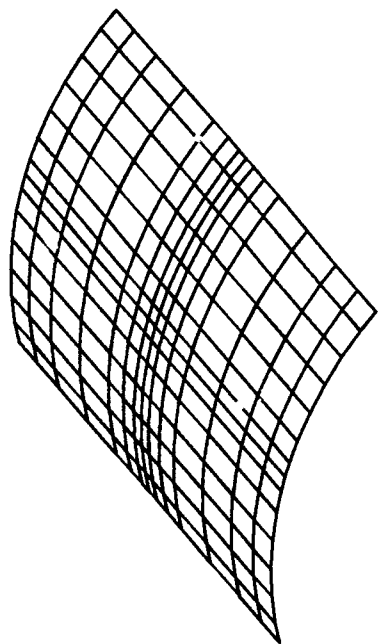
**Figure 4.6c.** Meshes representing a composite cylindrical shell subjected to a transverse step load applied to the center.  
Radius = 12 in., SLR formulation.



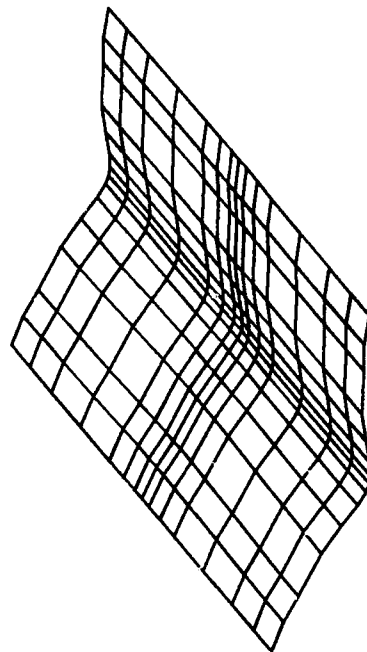
0.0030 seconds



0.0053 seconds

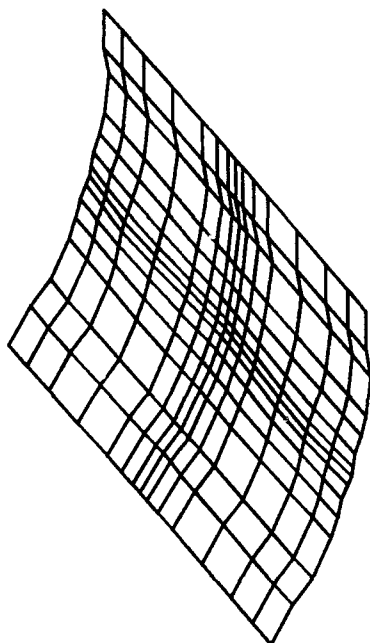


0.0 seconds

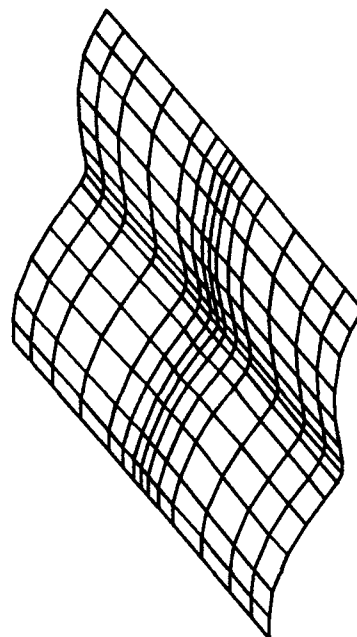


0.0048 seconds

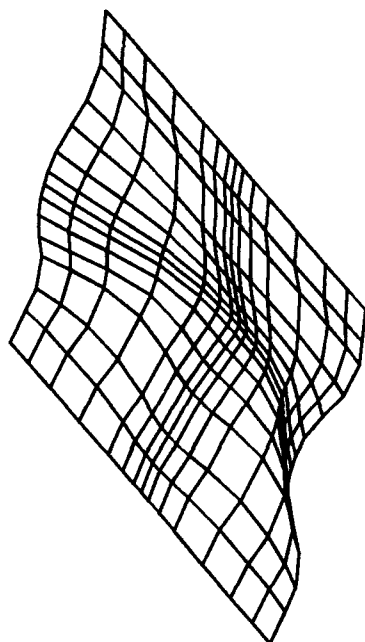
**Figure 4.7a.** Meshes representing a composite cylindrical shell subjected to a transverse step load applied to the center.  
Radius = 12 in., Donnell formulation.



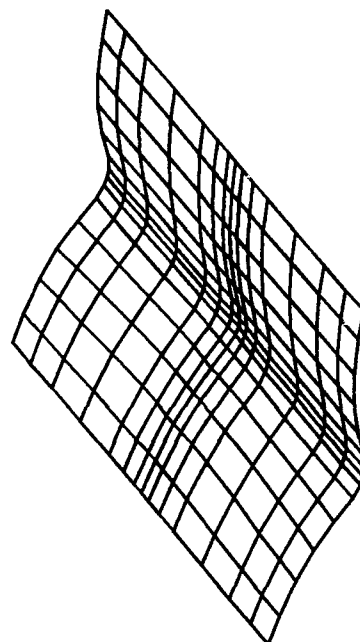
0.0068 seconds



0.0085 seconds

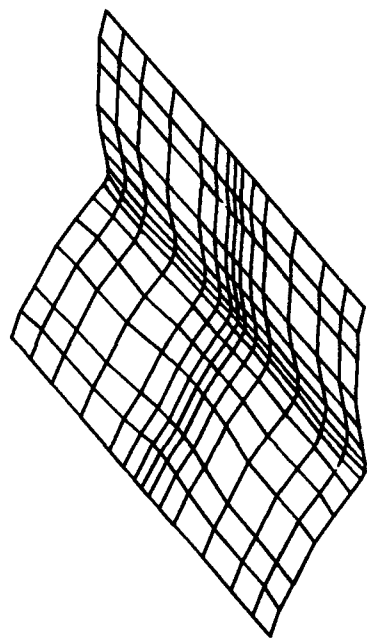


0.0060 seconds

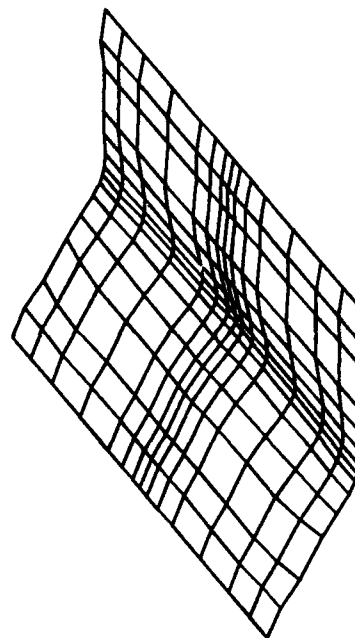


0.0072 seconds

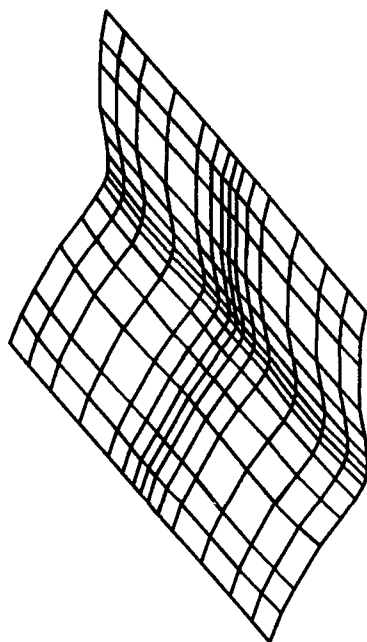
**Figure 4.7b.** Meshes representing a composite cylindrical shell subjected to a transverse step load applied to the center.  
Radius = 12 in., Donnell formulation.



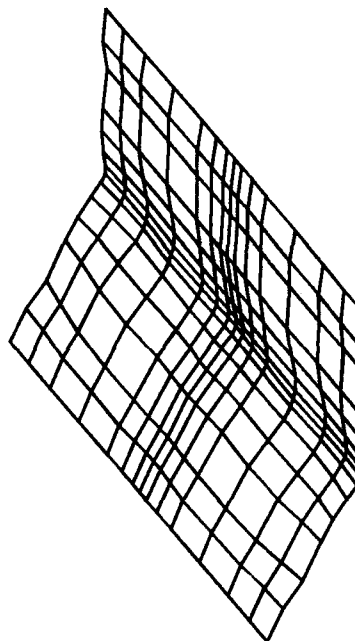
0.0141 seconds



0.0204 seconds



0.0115 seconds



0.0165 seconds

**Figure 4.7c.** Meshes representing a composite cylindrical shell subjected to a transverse step load applied to the center.  
Radius = 12 in., Donnell formulation.

amplitude and an increasing frequency at the center node. On the other hand, the center node of the Donnell shell experiences a significant upward motion at the end of the transient phase. Further, the entire displacement field (except at the boundaries) experiences a sudden upward movement; this phenomenon is illustrated in Figure 4.7 at  $t = 0.0085s$ . This effect is not apparent in the SLR models. In general, the potential and kinetic energy distribution of the Donnell model distributes throughout the shell differently than the SLR model because energy that would normally distribute through all of the higher-order nonlinear terms (numerically through solution of the matrix equations) is not possible in the Donnell model. This effect shows up graphically in figures for the deeper shells in the following section.

#### *4.3 Six in. Radius Cylindrical Shell*

For a deeper 6 in. radius cylindrical shell, both model formulations are observed to initiate collapse under the same load history as indicated in Figure 4.8. Although the effective flexural stiffness of the Donnell shell is higher than the SLR shell (as it was in the 8 in. radius shell), the applied loading is sufficient to result in collapse for both shells. However, it is likely that there is a small range of load levels, for a given loading rate, where only the SLR shell, and not the Donnell shell, would collapse. Figure 4.8 shows that the Donnell curve also experiences a significant upward displacement near the end of the transient period which is a behavior observed in the 12 in. radius Donnell shell. Moreover, Figure 4.8 at time  $t=0.0115s$  is also similar to Figure 4.4 at  $t=0.0085s$  in that the displacement field snaps a small distance upwards. It is also apparent from Figure 4.8 that the differences between the Donnell and SLR formulations are more conspicuous.

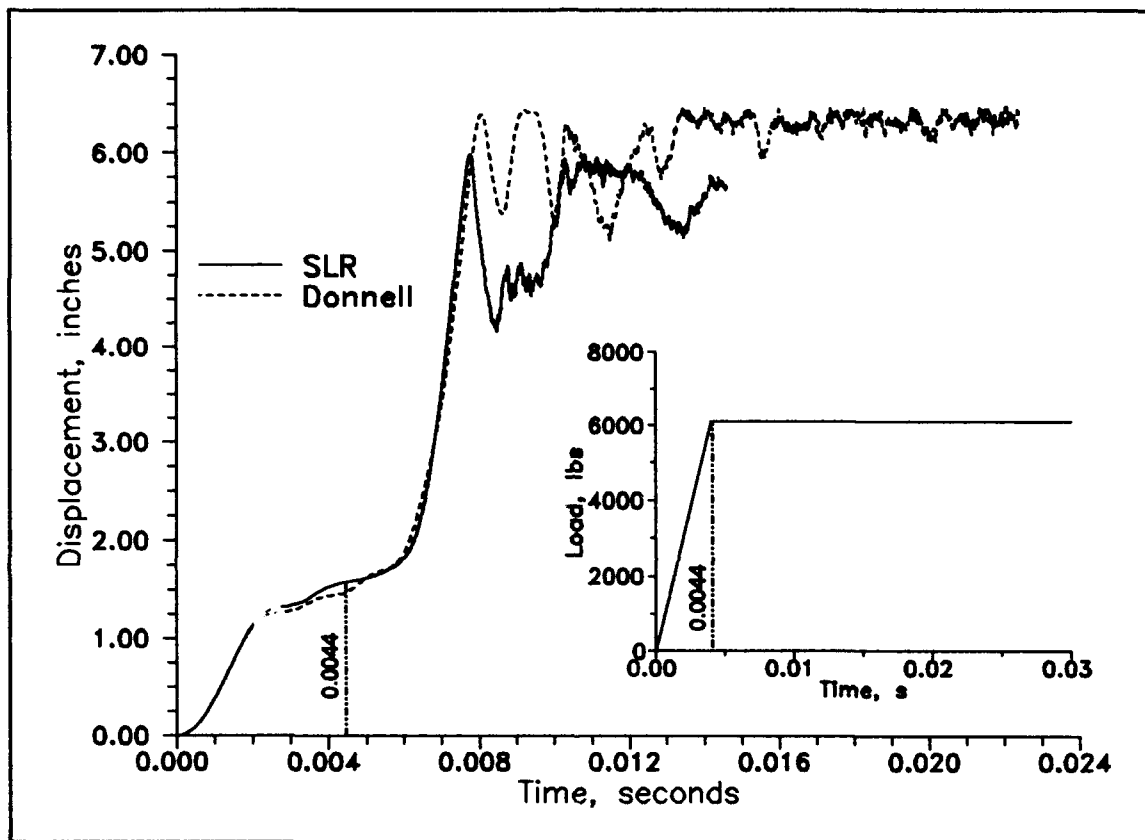
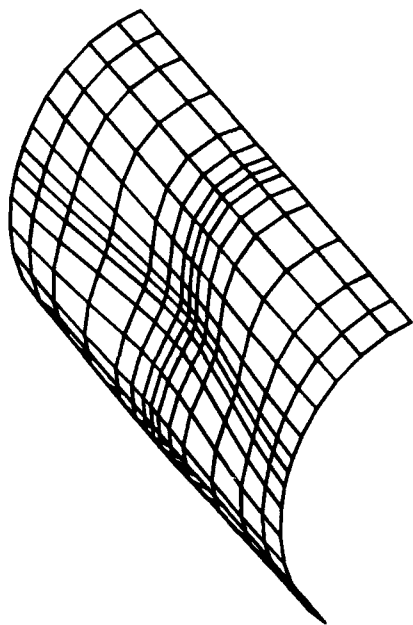


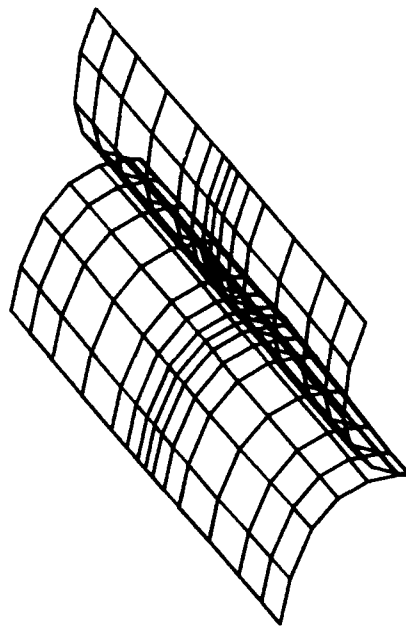
**Figure 4.8.** Center node displacements of composite cylindrical shells subjected to a transverse step load applied to the center. Radius = 6 in.

Prior to collapse, both formulations predict similar behavior. Also, the reduction of the center node displacement rate in the early part of the curve is more conspicuous when compared to shallower shells. Again, collapse occurs a significant time after the maximum load level is achieved as indicated in Figure 4.8. As Chien and Palazotto indicate (2), the point of divergence between curves, corresponding to a shell that eventually collapses and a shell that does not collapse, indicates the initiation of dynamic instability. A curve corresponding to a shell that does not collapse was generated but is not shown. As in the 8 in. radius shell, the dynamic instability initiates at the same time the maximum load level is reached. The vertical line in Figure 4.16 indicates the time when the maximum load level is reached (the initiation of dynamic instability possibly due to parametric vibration).

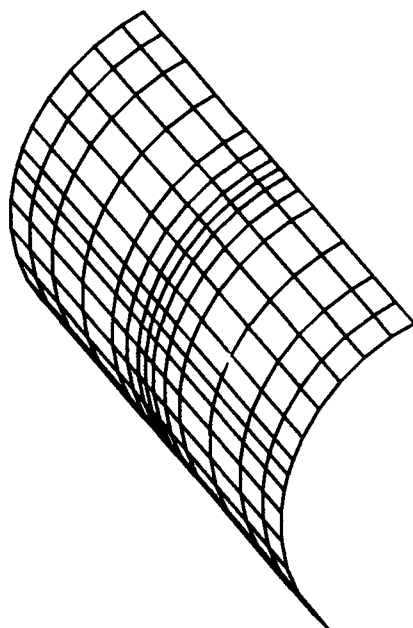
After collapse, the Donnell shell displaces a further distance. Also, the Donnell shell has more oscillations during the transient phase. Figures 4.9 and 4.10 show the Donnell and SLR displacement fields at various times for the 6 in. radius shell. For the stages up to and at collapse, the shell shapes are similar. During the transient phases, the behaviors are very different. In particular, the Donnell formulation exhibits some peculiar behavior. For example, Figure 4.10 shows that some meshes have elements along the boundaries that have stretched to several times its original size, while the elements along the centerline have compressed to very small sizes. In particular, the Donnell mesh at  $t = 0.0095s$  takes on an odd appearance. This behavior shows, with more clarity (from a graphical viewpoint), that the distribution of energy in the Donnell model is significantly differently than the SLR model. The Donnell solution has the elements along the boundary in a higher state of tension (indicated by stretched elements) and the elements



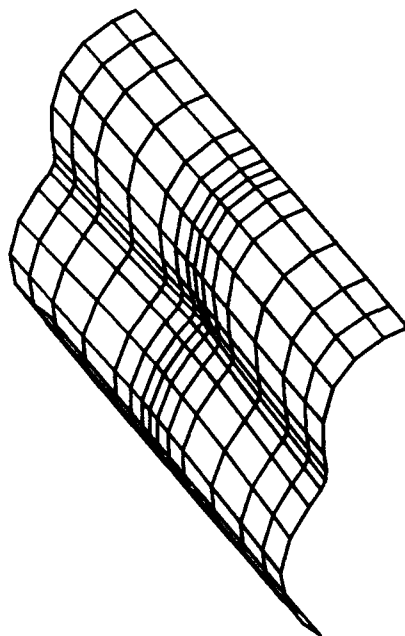
0.0024 seconds



0.0078 seconds

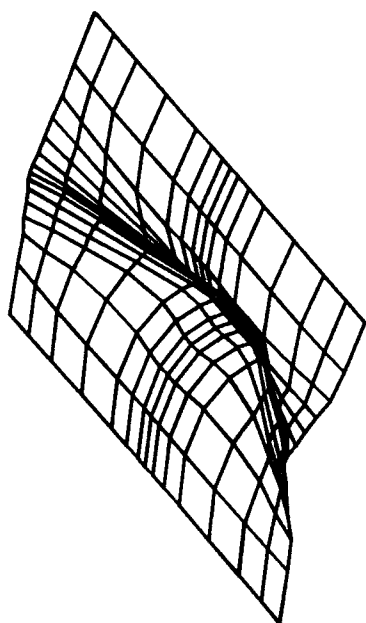


0.0 seconds

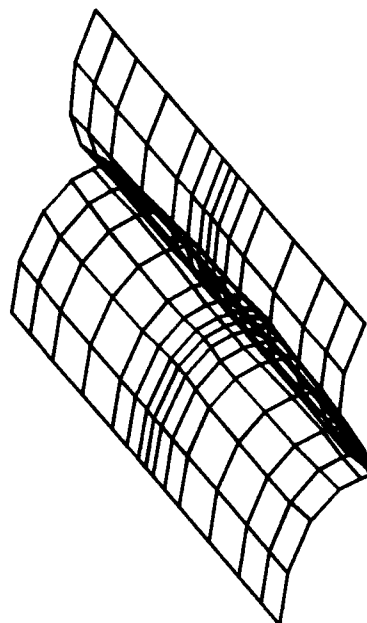


0.0062 seconds

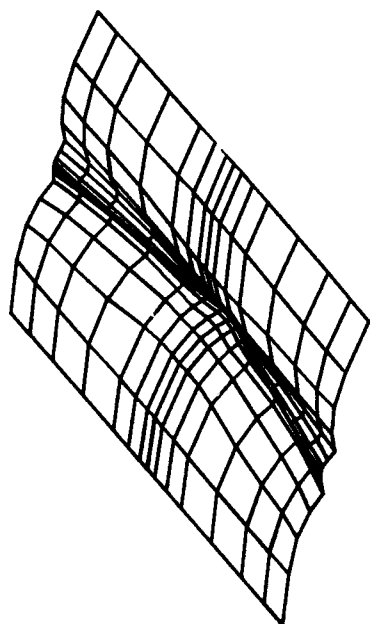
**Figure 4.9a.** Meshes representing a composite cylindrical shell subjected to a transverse step load applied to the center. Radius = 6 in., SLR formulation.



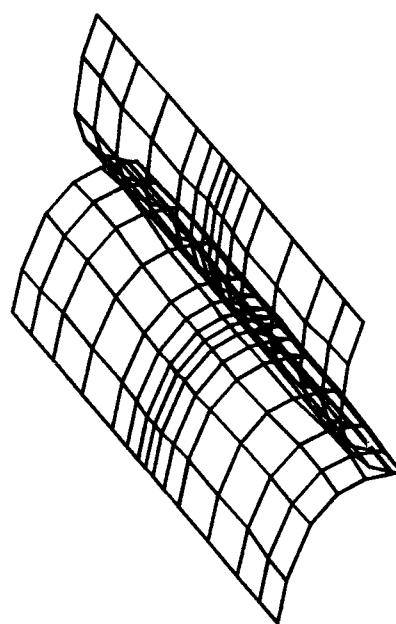
0.0092 seconds



0.0126 seconds

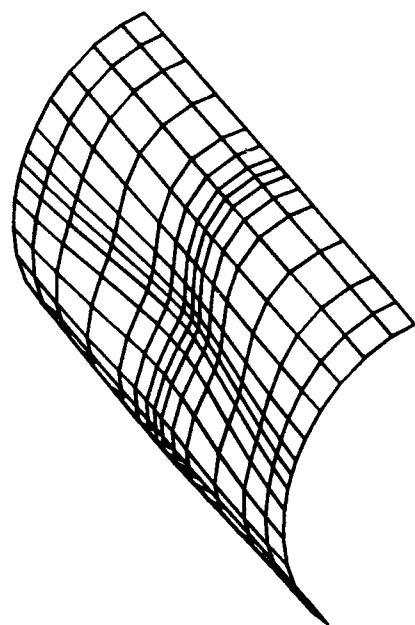


0.0085 seconds

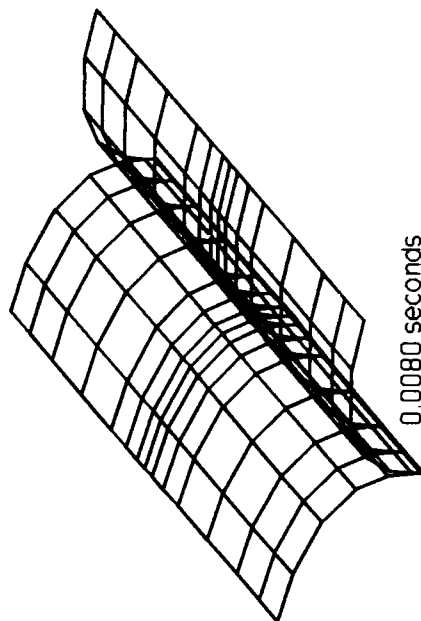


0.0109 seconds

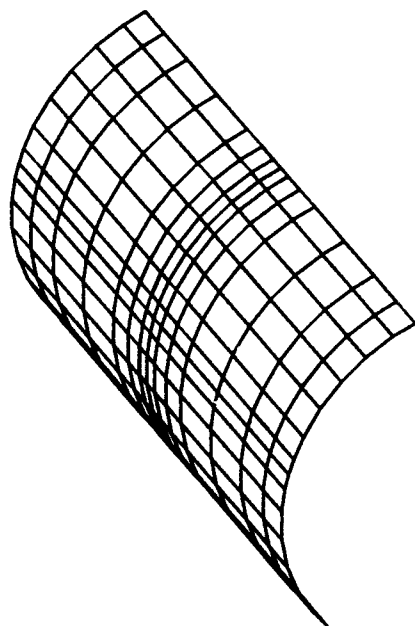
**Figure 4.9b.** Meshes representing a composite cylindrical shell subjected to a transverse step load applied to the center.  
Radius = 6 in., SLR formulation.



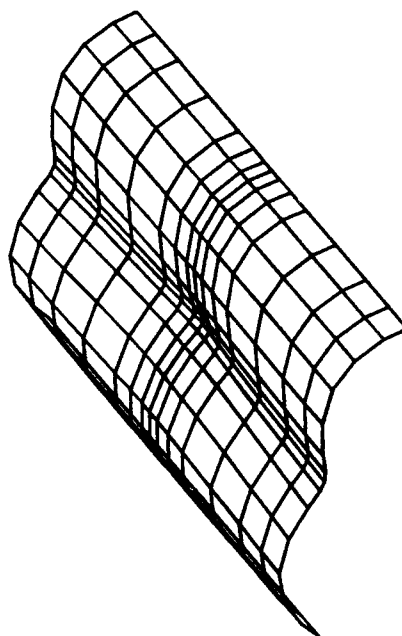
0.0024 seconds



0.0080 seconds

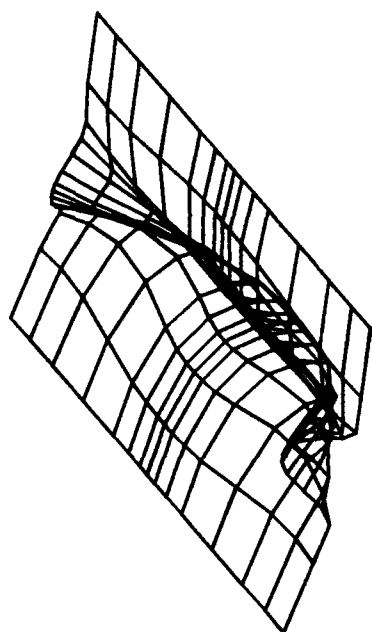


0.0 seconds

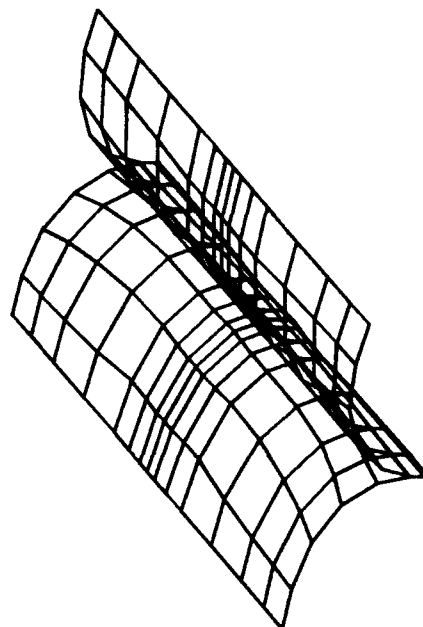


0.0062 seconds

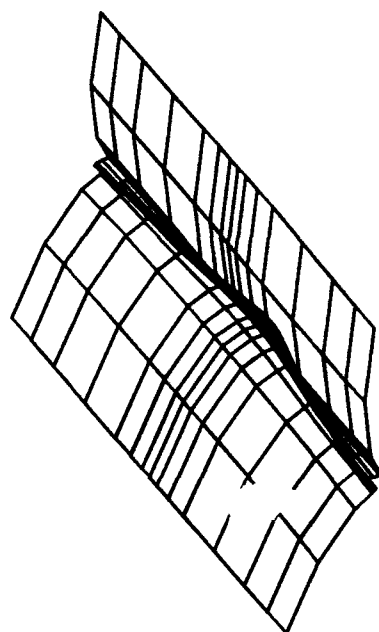
**Figure 4.10a.** Meshes representing a composite cylindrical shell subjected to a transverse step load applied to the center.  
Radius = 6 in., Donnell formulation.



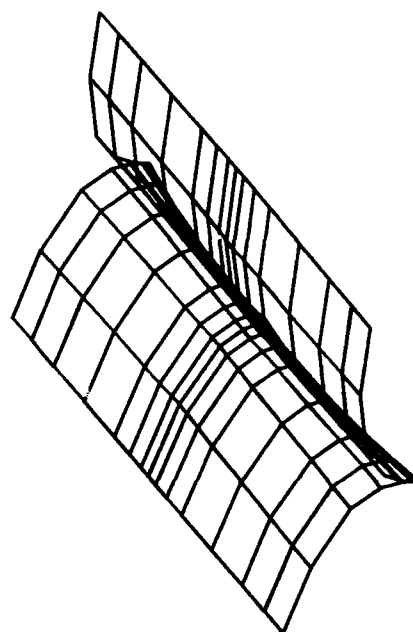
0.0095 seconds



0.0105 seconds

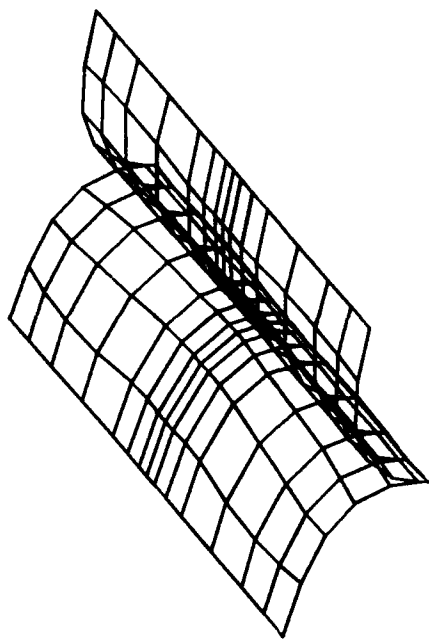


0.0087 seconds

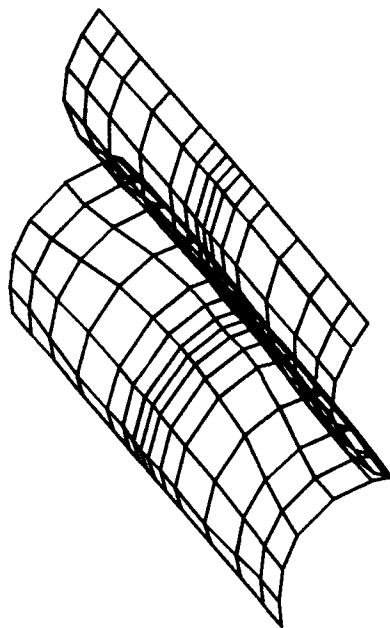


0.0100 seconds

**Figure 4.10b.** Meshes representing a composite cylindrical shell subjected to a transverse step load applied to the center. Radius = 6 in., Donnell formulation.



0.0125 seconds



0.0115 seconds

**Figure 4.10c.** Meshes representing a composite cylindrical shell subjected to a transverse step load applied to the center. Radius = 6 in., Donnell formulation.

along the center line in an higher state of compression (indicated by compressed elements), when compared to the SLR model during the transient phase. The elements in the SLR model tend to be more evenly proportioned relative to the original undeformed element shapes. After the transient period, both models show that the elements are distributed more evenly in size.

#### *4.4 Four in. Radius Cylindrical Shell*

Figure 4.11 shows the center node displacement curves of 4 in. radius cylindrical shells using the SLR and Donnell formulations. The disagreement between both models is even more apparent after collapse, although the curve characteristics as discussed in the preceding paragraphs are the same. The inflection point, which is an indication of the onset of instability, is not as distinguishable as it is in the shallower shells; this may be due to the maximum load level occurring in a more gradual fashion as indicated in the loading curve. The SLR shell snaps sooner than the Donnell shell since the higher number of rotational terms gives the SLR shell more flexibility. Figures 4.12 and 4.13 display the deformed geometries of the Donnell and SLR shells. Despite the fact that the models assume perfectly elastic behavior with no material failure, the odd post-collapsed meshes suggest that the SLR and Donnell formulations may only be applicable for the analysis of deep cylindrical shells in the pre-collapsed stages. The post-collapsed geometries simply do not appear to be consistent with physical expectations. A comparison between deformed shell elements with the undeformed elements suggests that inordinate levels of strain are taking place in both models, especially near the hinged boundaries. In addition, apparent graphical aberrations in the meshes, such as the ones

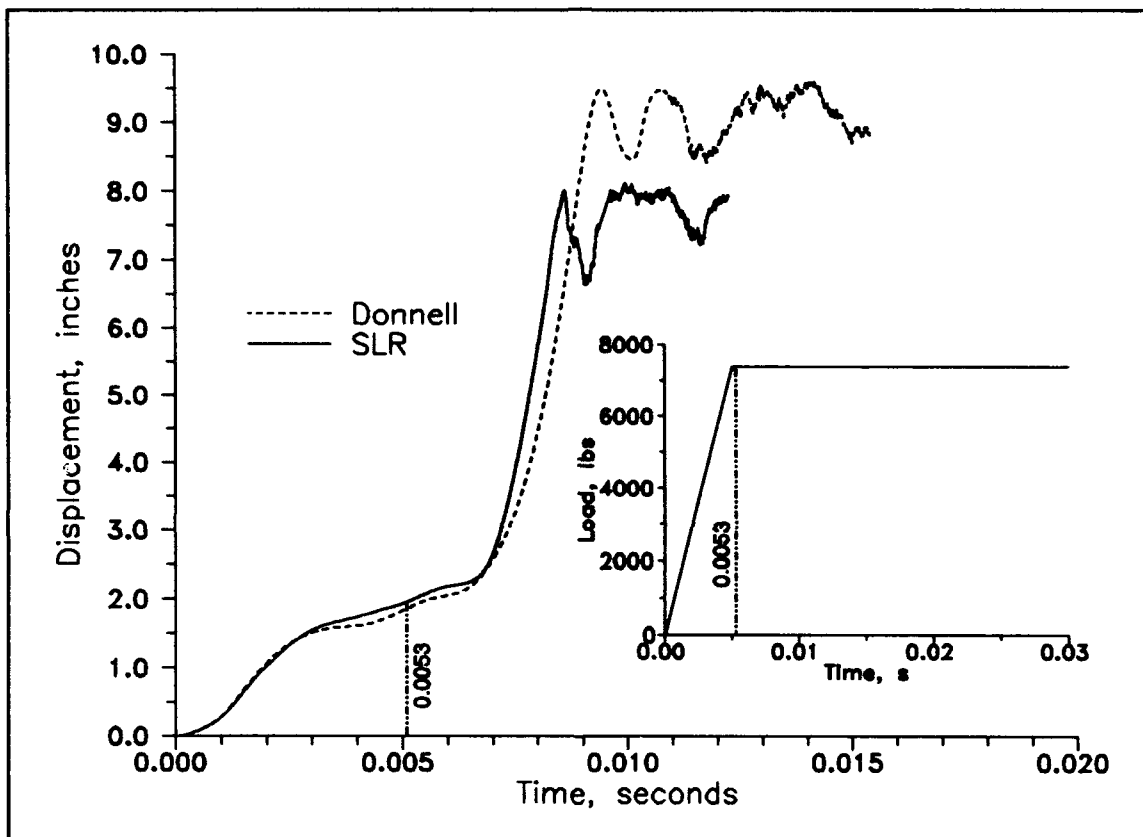


**Figure 4. 11.** Center node displacements of composite cylindrical shells subjected to a transverse step load applied to the center. Radius = 4 in.

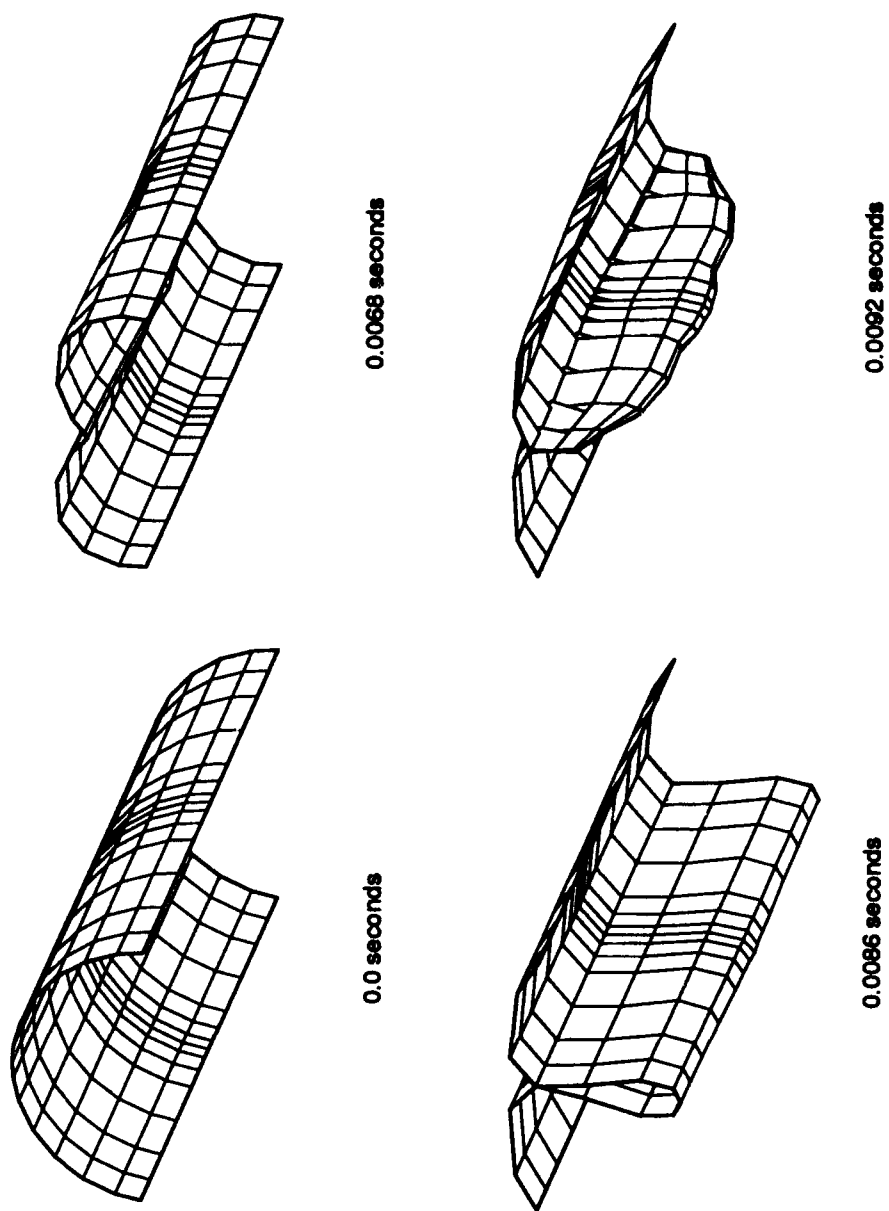


**Figure 4.12.** Meshes representing a composite cylindrical shell subjected to a transverse step load applied to the center.  
Radius = 4 in., SLR formulation.

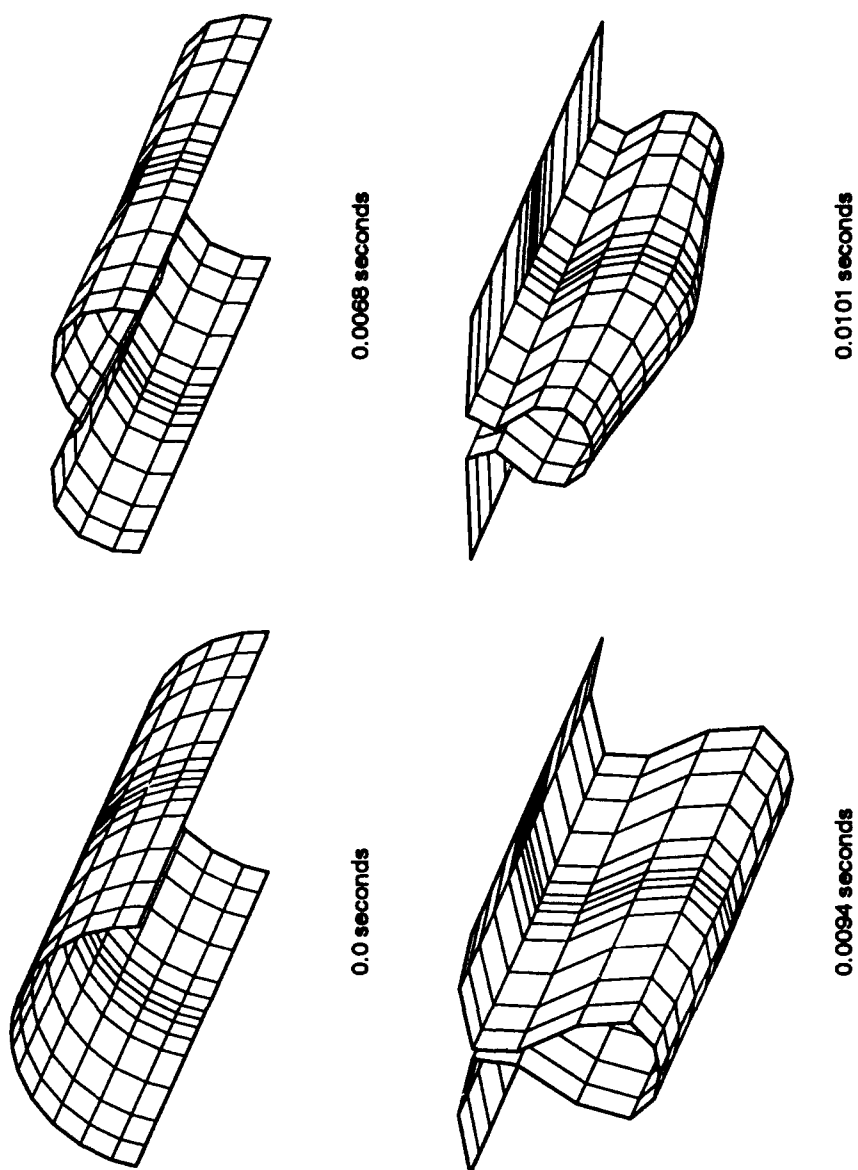
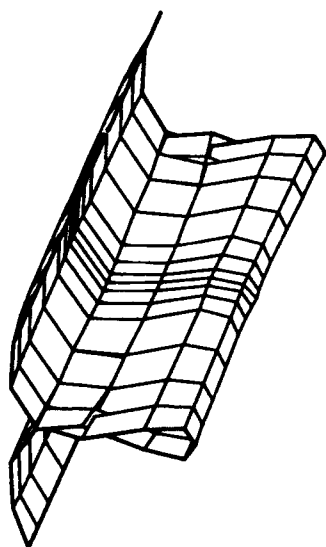
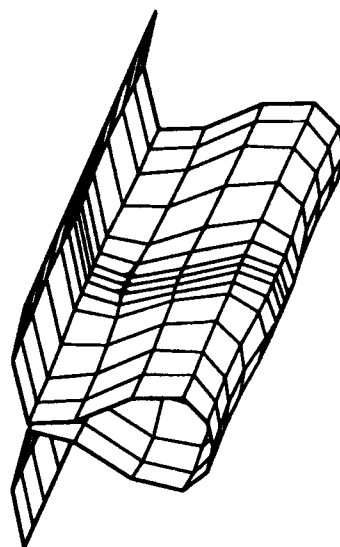


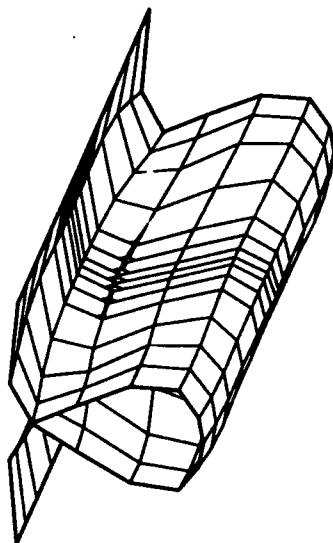
**Figure 4.13a.** Meshes representing a composite cylindrical shell subjected to a transverse step load applied to the center.  
Radius = 4 in., Donnell formulation.



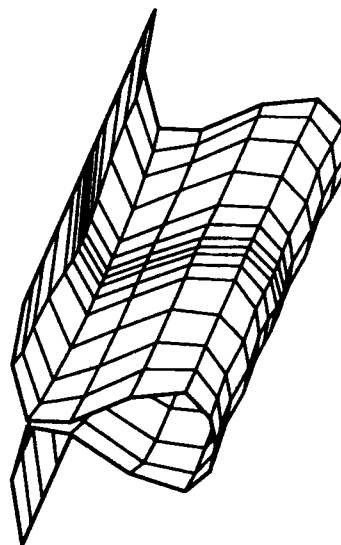
0.0118 seconds



0.0141 seconds



0.0108 seconds



0.0131 seconds

**Figure 4.13b.** Meshes representing a composite cylindrical shell subjected to a transverse step load applied to the center.  
Radius = 4 in., Donnell formulation.

displayed at  $t = 0.0092s$  in Figure 4.12 and three of the meshes in Figure 4.13 are a result of portions of the laminate passing through its symmetric half. Further, it appears that there are severe slope discontinuities between many of the elements<sup>1</sup>. Still, compatibility and potential energy constraints are satisfied even though the shapes do not correlate well with a real system. This problem indicates a limitation of the Donnell and SLR formulations at these levels of rotations. It is possible that refining the mesh may improve the results. The initiation of somewhat similar trends in the 6 in. radius shell may also appear to question some of the peculiar features observed in that solution.

#### *4.5 Twenty in. Radius Cylindrical Shell*

For cylindrical shells shallower than the 12 in radius shell, the SLR and Donnell formulations produce very similar results. Figures 4.14 and 4.15 show that the center node displacements for a 20 in. radius cylindrical shell have very similar general characteristics. The differences between the two curves would only be one of precise detail. The displacement curve has many of the characteristics noted earlier, i.e., an inflection before collapse, a snapping action, a transient period, and an oscillation near the static equilibrium solution. As in all previous cases, the initiation of collapse occurs slightly after the peak load is attained, but this period of dynamic instability is very short.

A comparison of the deformed meshes between both models indicates no significant differences between the two formulations. The collapsed shell of Figure 4.16 could represent the collapsed shape of either the Donnell or SLR models. As in the other cases,

---

<sup>1</sup>It should be noted that this discontinuity is primarily a limitation in the software package used to display the meshes. The node defining an element are connected by straight lines only. Therefore interelement slope compatibility is not accurately represented.

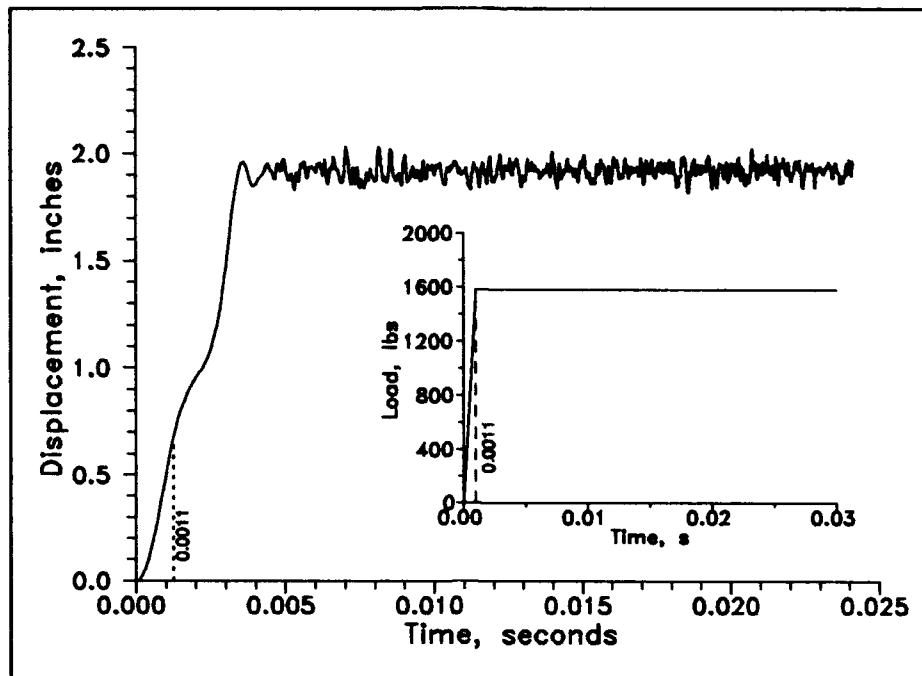


**Figure 4.14.** Center node displacement of a composite cylindrical shell subjected to a transverse step load applied to the center. Radius = 12, SLR formulation.

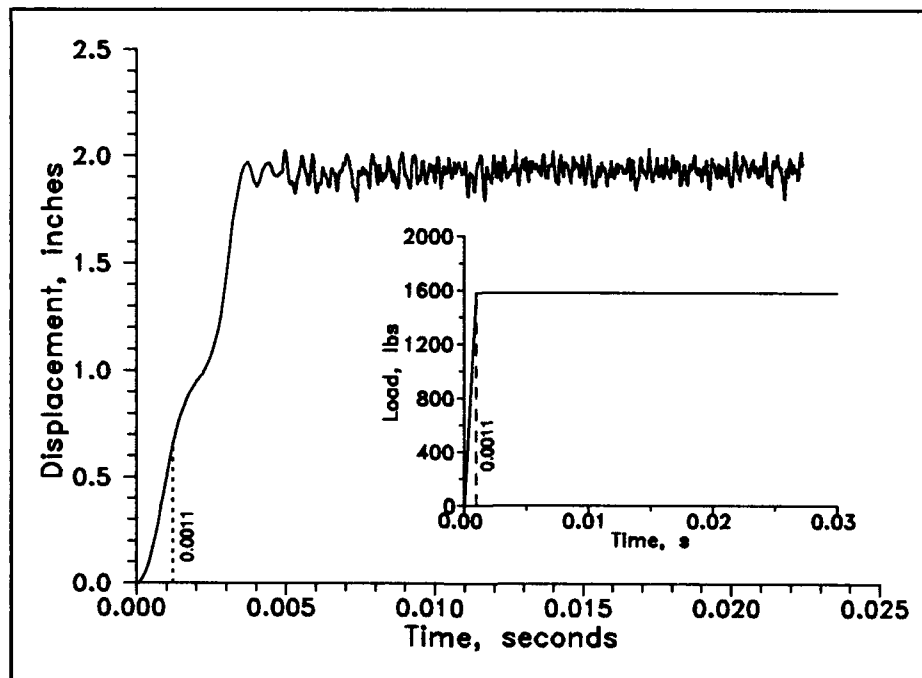


**Figure 4.15.** Center node displacement of a composite cylindrical shell subjected to a transverse step load applied to the center. Radius = 20, Donnell formulation.

one may observe slight deformations of the shell elements indicating the presence of in-plane vibrations. However, these changes are very slight from a graphical standpoint, and for this reason, no other collapsed meshes are displayed.

#### **4.6 *Sixty in. Radius Cylindrical Shell***

For a 60 in. radius shell, there appears to be no discernable deflection point; the shell appears to collapse immediately as indicated in the center node displacement history of Figure 4.17. One significant difference between this displacement curve and the previous curves is an absence of very high frequency oscillations superimposed on any portion of the waveform. Due to the higher radius of this shell, when compared to the smaller radii shells, the behavior is more oriented to plate response as will be subsequently discussed. This figure also shows that the SLR and Donnell models are in good agreement during the first one-and-a half cycles but that the different flexural behaviors predicted by the two formulations result in a slight phase difference at latter cycles.

#### **4.7 *Flat Plate***

A cylindrical shell with an arbitrarily large radius of 900,000 in. is assumed to behave as a flat plate. For a flat plate, there is no flexural stiffness for a transverse load to overcome and hence no snapping. The stress field is predominantly in tension upon immediate application of the load. Various excitation loads were applied to the flat plate. Figure 4.18 shows loading histories applied to a flat plate where the maximum load level is the same as the load applied to the 20 in. radius shell, but with loading rates that differ. The motivation was to determine the effect of loading rate on plate response. Figures

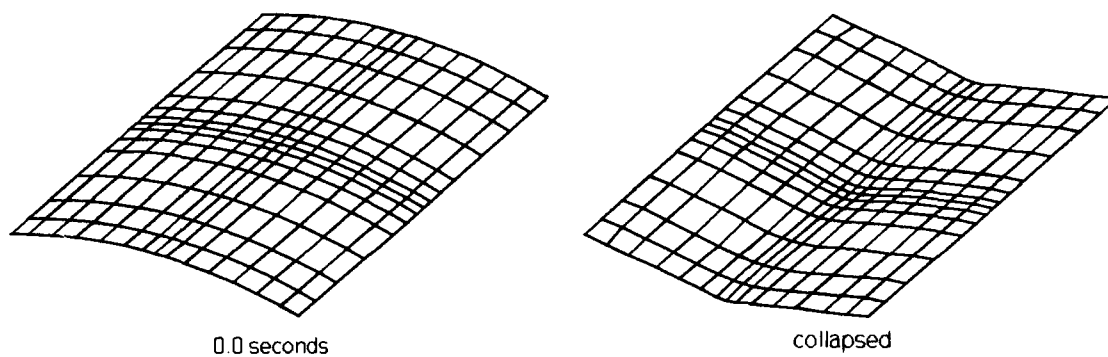


**Figure 4.16.** Meshes depicting a composite cylindrical shell in an unloaded and collapsed state. Radius = 20 in.

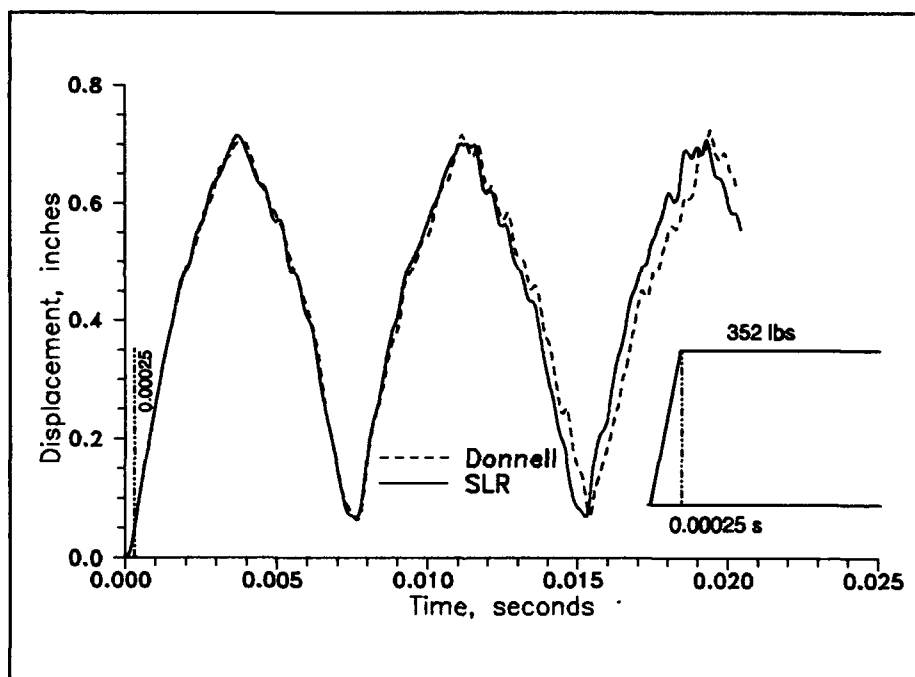


**Figure 4.17.** Center node displacements of composite cylindrical shell subjected to a transverse point load applied to the center. Radius = 60 in.

4.19, 4.20, 4.21, and 4.22 show the center node displacement of plates that result from these loads. The plate subjected to a higher loading rate undergoes larger deflections and contains higher frequency components when compared to the plates with the lower loading rates (this is further shown in Section 6.). However, the higher frequency components are at a much lower frequency when compared to the cylindrical shells with radii less than 60 in. (this is shown in Section 6 also). The plates with the lower loading rates also appear to exhibit harmonic or quasiperiodic motion after the applied load reaches its maximum level; however, this is not the case as will be demonstrated in Section VI. Figure 4.23 is another example which shows, with more clarity, the effect that initial loading rate has on the behavior of the composite plate. This figure represents the load applied to the 60 in. radius cylindrical shell with the exception that the various loading rates are much lower than any of the rates used thus far.

Figure 4.24 shows the center node displacement of a flat plate subjected to the loading history of the 8 in. radius shell (see Figure 3.2). Higher deflections, larger oscillation amplitudes, and an increase in high frequency components are apparent when compared to the previous plate examples. Compared to the 8 in. radius shell, the plate does not exhibit similar high frequency behavior (see Figure 4.1). This effect may be due the absence of the snapping phenomenon and the constrained motion of a vibrating plate. The snapping phenomenon is associated with the high inertia values due to the sudden change in the displacement field. Moreover, after collapse the cylindrical shell elements vibrate with in-plane and out-of-plane motions. The plate elements, on the other hand, probably vibrate primarily in the vertical directions. Therefore, the high frequency character of the collapsed shell center node may be due in part to the disturbance caused

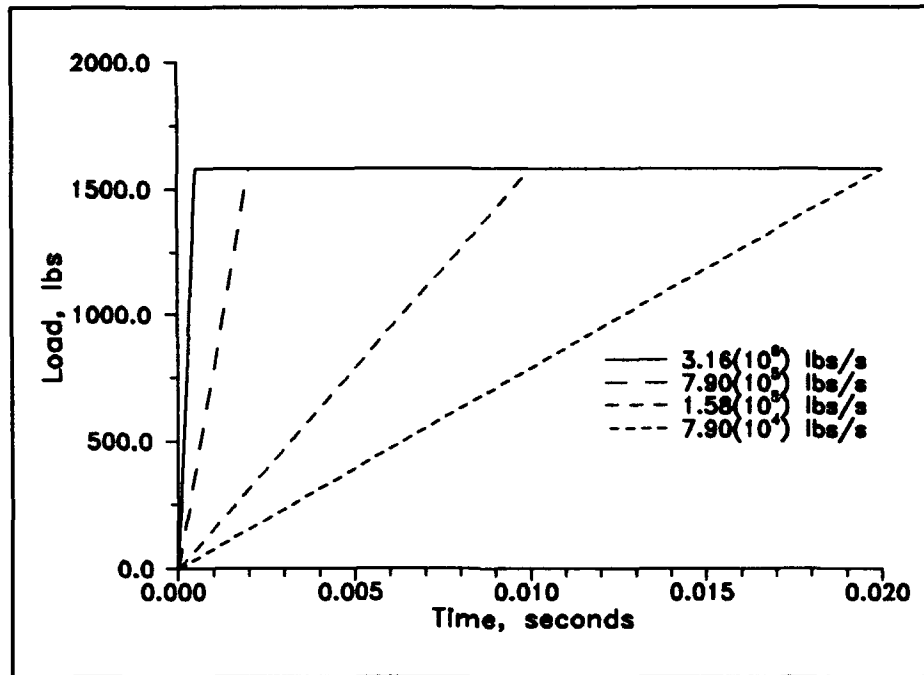


**Figure 4.18.** Various loading curves applied to flat composite plates.

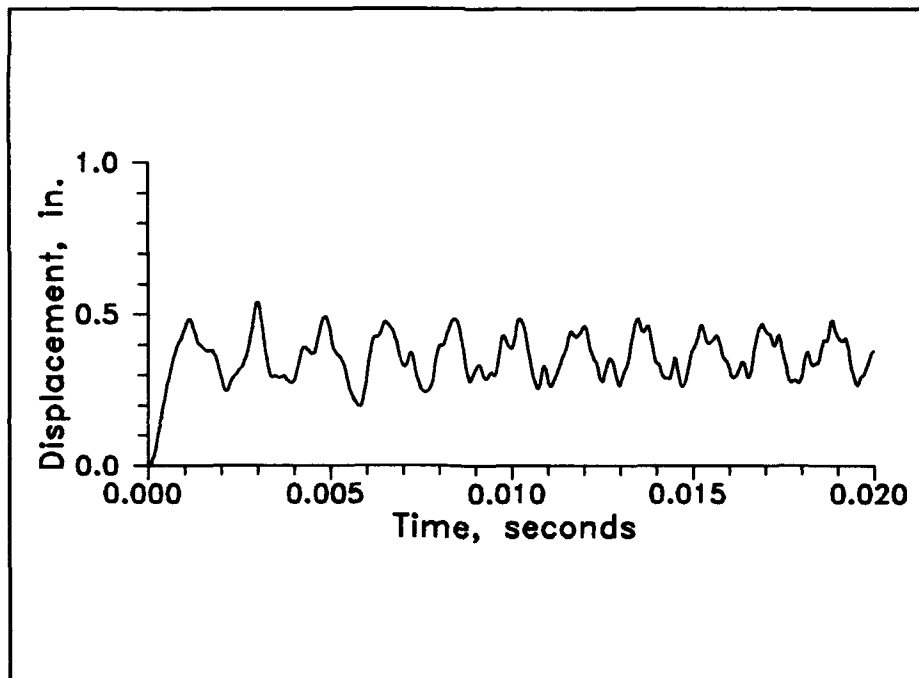


**Figure 4.19.** Center node displacement of a composite plate subjected to a transverse step load applied to the center. Initial loading rate of  $3.16(10^6)$  lbs/s

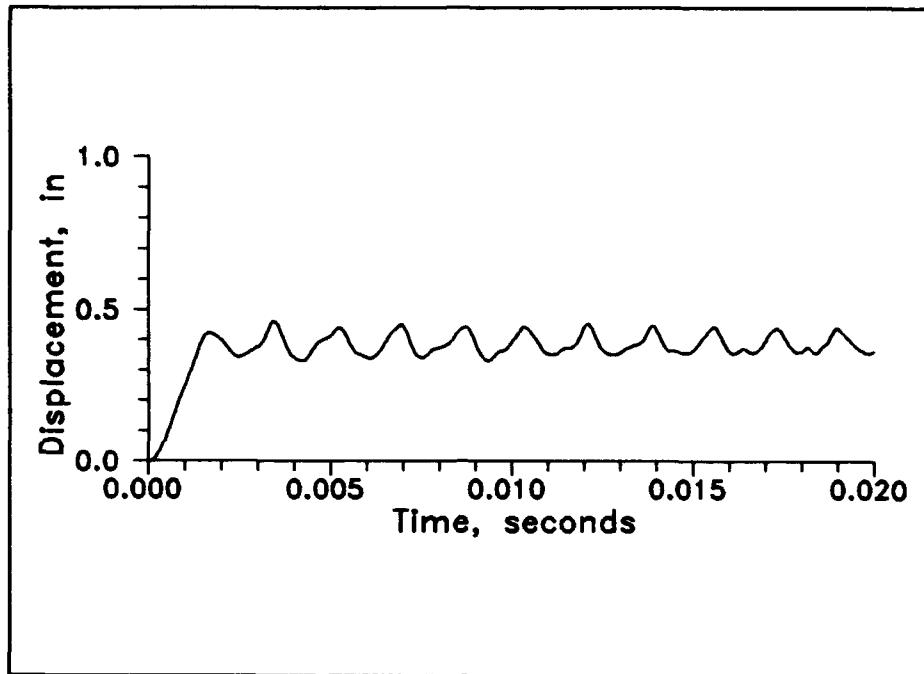


**Figure 4.20.** Center node displacement of a composite plate subjected to a transverse step load applied to the center. Initial loading rate of  $7.90(10^5)$  lbs/s

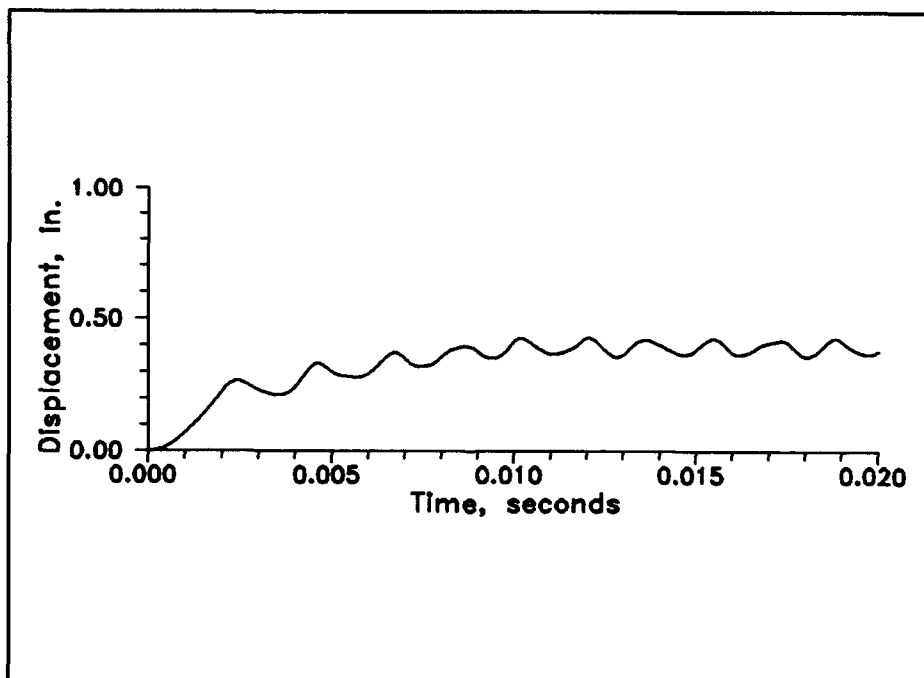


**Figure 4.21.** Center node displacement of a composite plate subjected to a transverse step load applied to the center. Initial loading rate of  $1.58(10^5)$  lbs/s

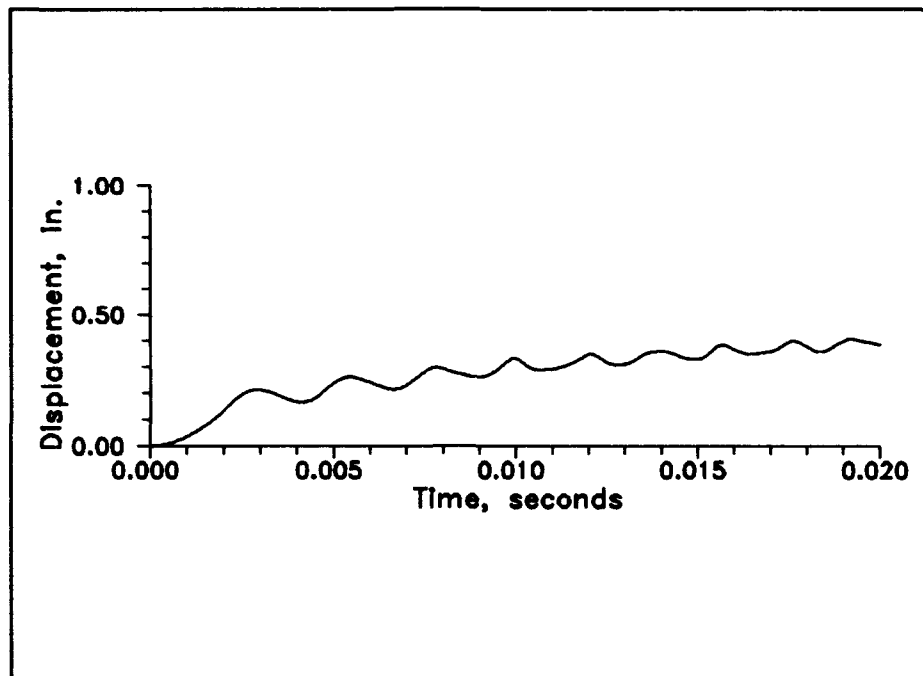


**Figure 4.22.** Center node displacement of a composite plate subjected to a transverse step load applied to the center. Initial loading rate of  $7.90(10^4)$  lbs/s

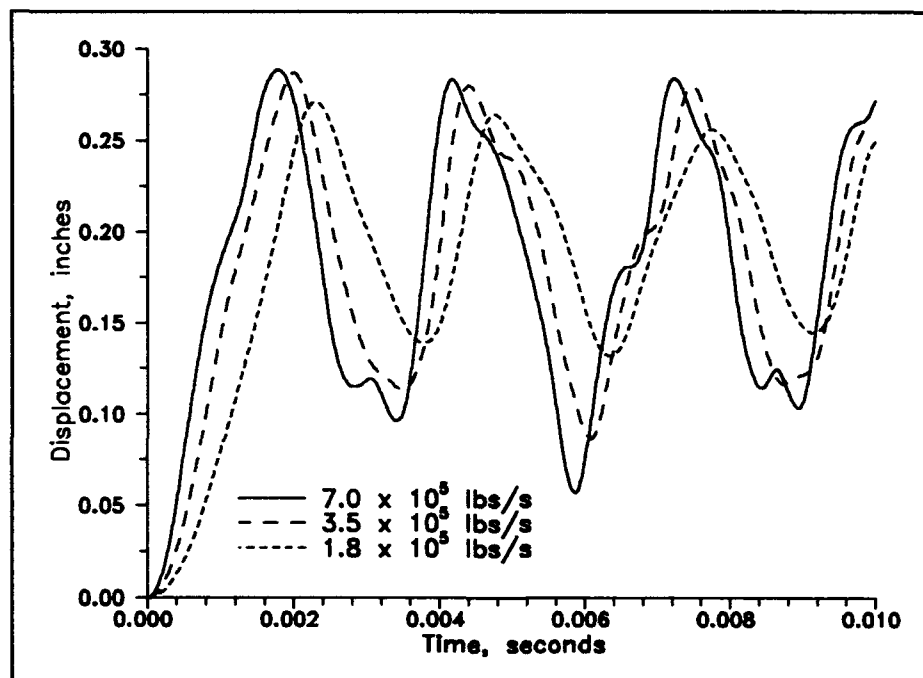


**Figure 4.23.** Effect of loading rate on the center node displacement of a flat composite plate subjected to a transverse step load applied to the center. Max load = 352 lbs.

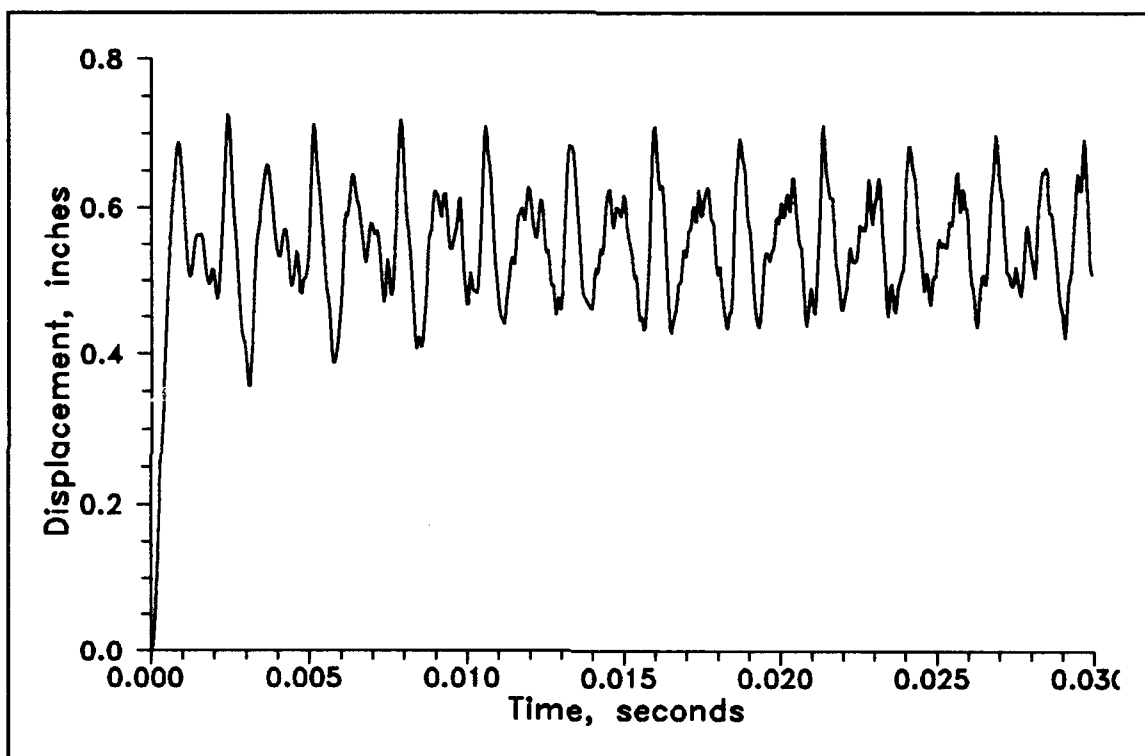
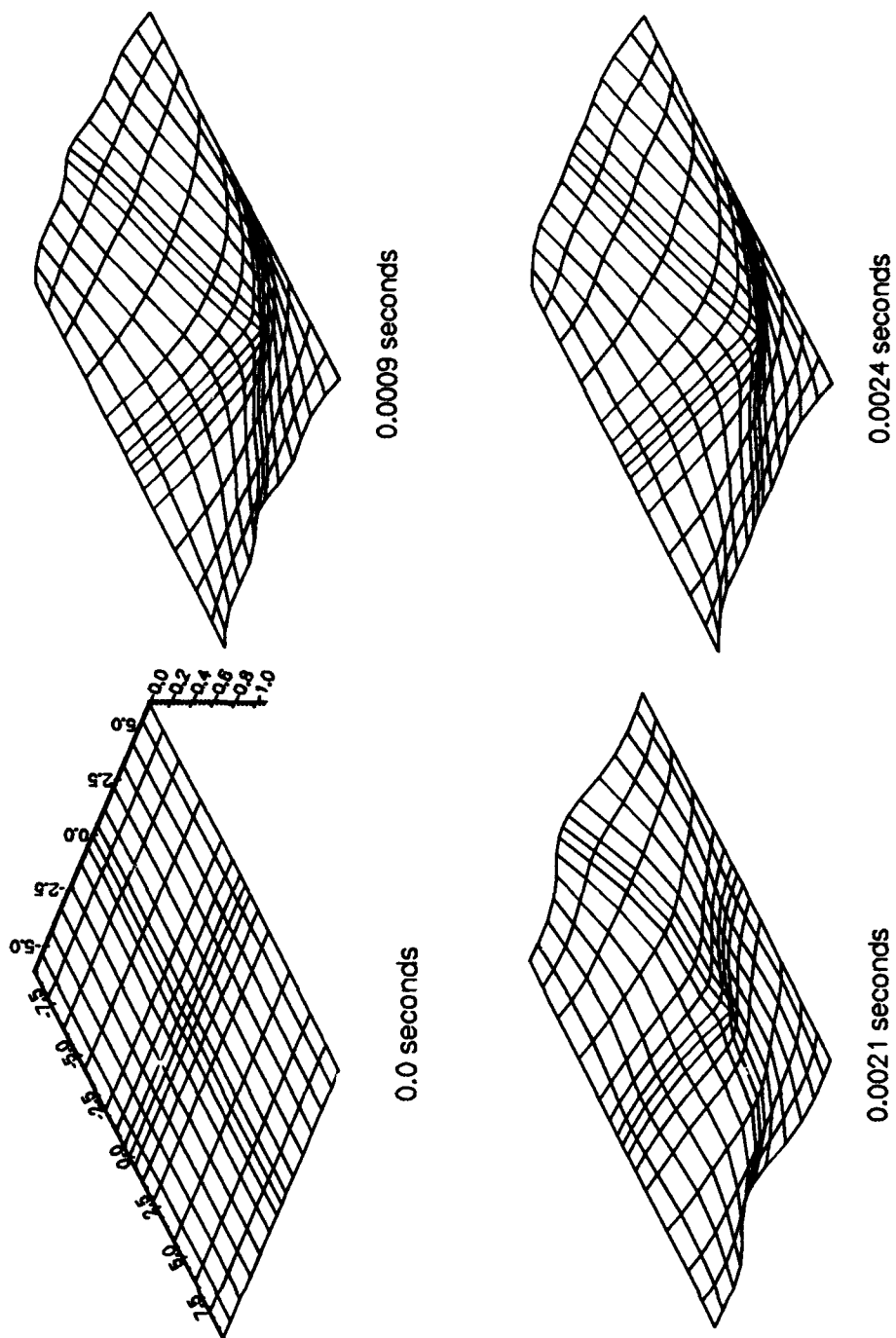


**Figure 4.24.** Center node displacement of a flat composite plate subjected to a transverse step load applied to the center. Initial loading rate of  $1.4(10^6)$  lbs/s, max load of 4232 lbs.

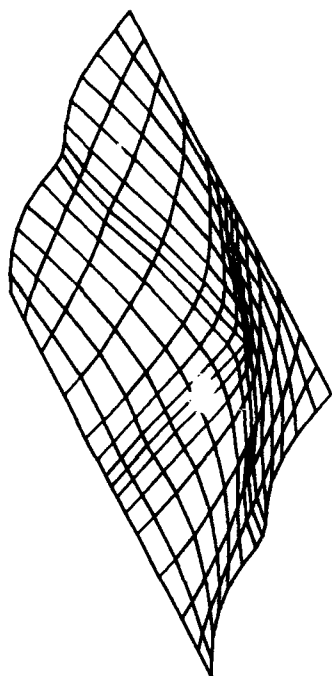
by the other elements. However, no data is available to support this supposition and follow-up work is indicated.

Figure 4.25 shows exaggerated views of some of the displacement fields corresponding to the plate with the heavier loading (a correct scaling produced meshes with features that were difficult to distinguish). The figure indicates that the free edges of the flat plate undergo significant motions as in the deep shell cases, but these effects are diminished in intensity. Thus, as the shell curvature is reduced, the edge effects restrains the free edge motion in relation to the displacement at the center node.

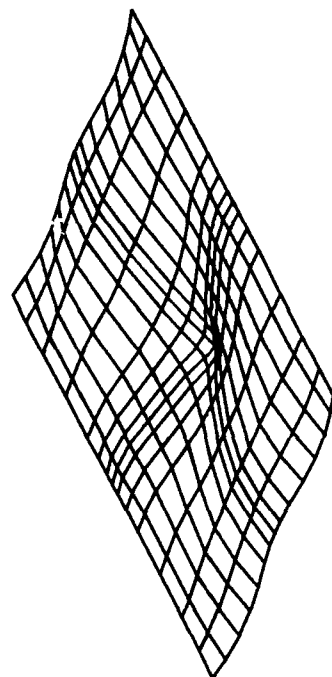
An unexpected outcome of the plate analysis is that there was no significant difference between the SLR and von Karman (i.e., a special case of the Donnell formulation where all radius values are arbitrarily large) results for a flat plate. Comparison between the output files of the two formulations did reveal very minute numerical differences, but not enough to affect the displayed waveforms. Thus, all of the previous plate results are applicable to both the SLR and von Karman formulations. This result implies that the higher-order nonlinear terms are effectively removed when the value of  $R_2$  is arbitrarily large. A check of the strain equations (14:44) indicates that  $R_2$  appears in the denominators of most (if not all) of the higher-order nonlinear terms effectively removing them from the equations.



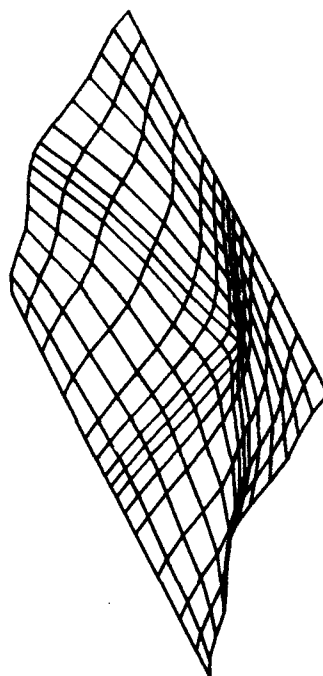
**Figure 4.25a.** Meshes representing a flat composite plate subjected to a transverse step load. Vertical displacements scaled up by a factor of 4.



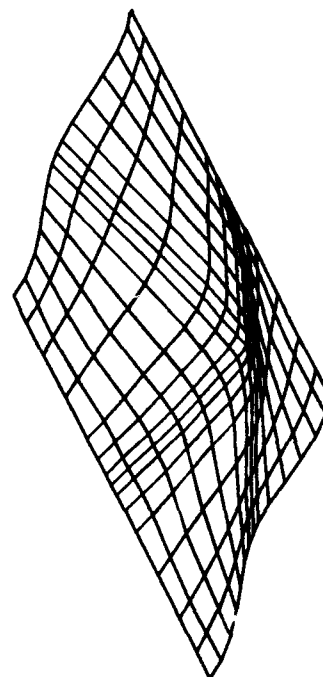
0.0037 seconds



0.0030 seconds



0.0146 seconds



0.0133 seconds

**Figure 4.25b.** Meshes representing a flat composite plate subjected to a transverse step load. Vertical displacements scaled up by a factor of 4.

## V NUMERICAL STABILITY

The time-step selection scheme outlined in the Section III results in numerically stable output for all of the Donnell models examined. On the other hand, for SLR cylindrical shells with radii less than 8 inches, the recommended post-collapse time step will eventually result in the accumulation of numerical errors. It is believed that since the SLR formulation contains far more terms than the Donnell formulation, the possibility of propagating errors becomes higher. Figures 5.1 and 5.2 show where numerical instabilities occur for a given time step. Despite the fact that an erratic solution is predicted, which implies numerical convergence, the solution is not assumed to be correct. Accuracy of this unstable portion can be checked by reducing the time step further. As the figures indicate, a slightly smaller time step results in completely different displacement values (upper portions of the curves) when compared to the numerical instabilities. Further time step reductions do not result in appreciable changes in the upper portions of the curves, so the solution is likely to be correct. The figures suggest that periodically reducing the time step will result in numerically stable output. However, the drawback to this procedure is in the significant computational times required. For example, a fully dedicated SPARC 2 Sun system required 12 days to compute that portion of the SLR curve in Figure 5.2 where a time step of  $2.0(10^{-6})$  seconds was required for stable results. Moreover, it is not clear when a change to the smaller time step should be initiated. An alternative would be to require improved accuracy by lowering the convergence tolerance requirements, but it is also not clear if this procedure would reduce or increase the computational time. Although it is recognized that the SLR and Donnell formulations are not applicable to modelling the post-collapsed behavior of the deeper

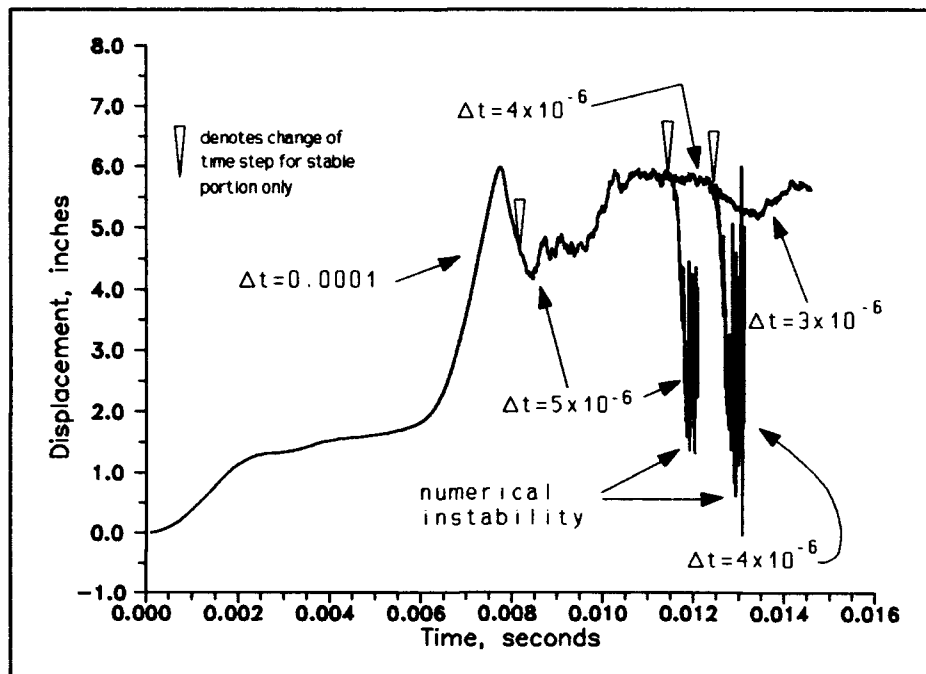


**Figure 5.1** Numerical instability in the center node displacement of a composite cylindrical shell subjected to a transverse step load applied to the center. Radius = 6 in., SLR formulation.

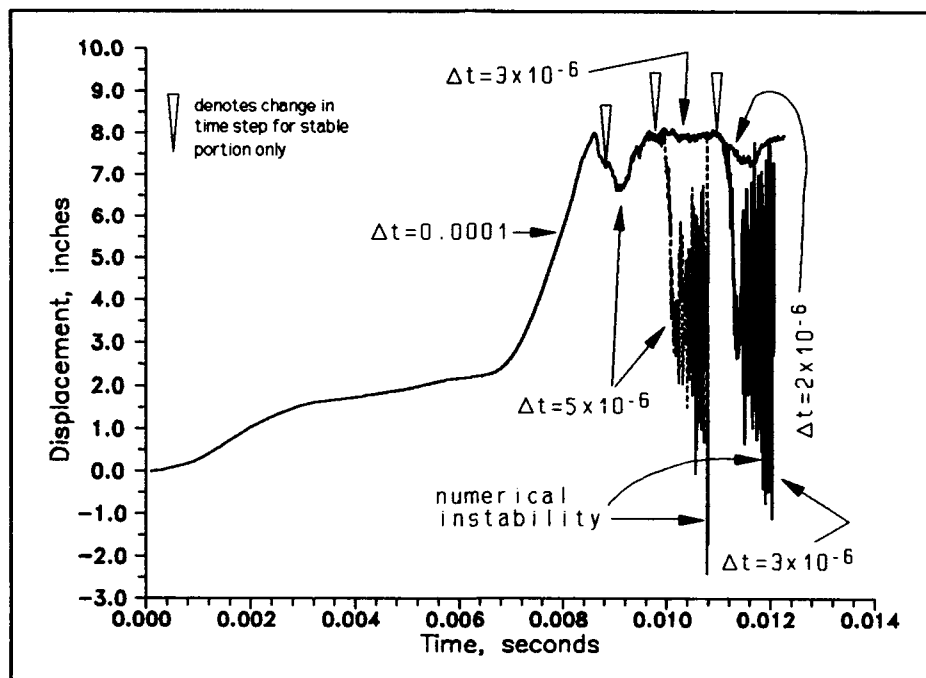


**Figure 5.2** Numerical instability in the center node displacement of a composite cylindrical shell subjected to a transverse step load applied to the center. Radius = 4 in., SLR formulation.

shell geometries for the meshes selected (it is not clear if changing the mesh would produce better results), the findings do indicate that the Newton-Raphson and Beta-m methods will produce numerically stable results for deep shells as long as the time step is sufficiently small. Therefore, these iterative methods should be useful in producing stable results for formulations incorporating large deflection and large rotation features.

Numerical instability is also evident from an examination of the corresponding mesh. Figure 5.3 shows an example of a numerically unstable mesh solution. Compatibility and potential energy constraints are still satisfied, but the accumulation of numerical errors results in a totally unrealistic displacement field.

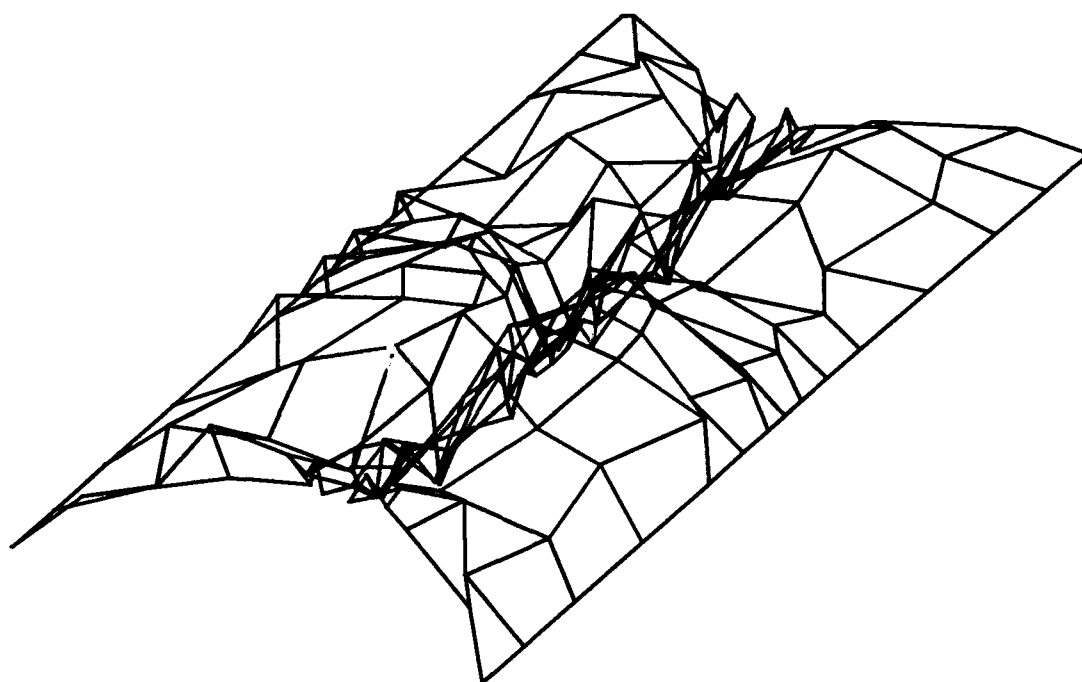


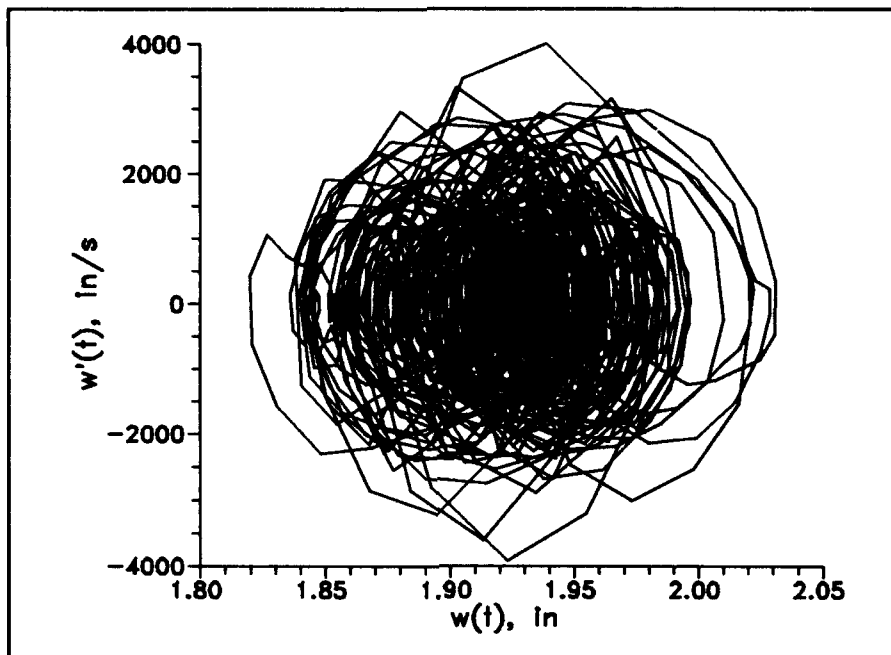
**Figure 5.3** Numerically unstable solution of a deep composite cylindrical shell subjected to a transverse point load applied to the center.

## VI CHAOTIC BEHAVIOR

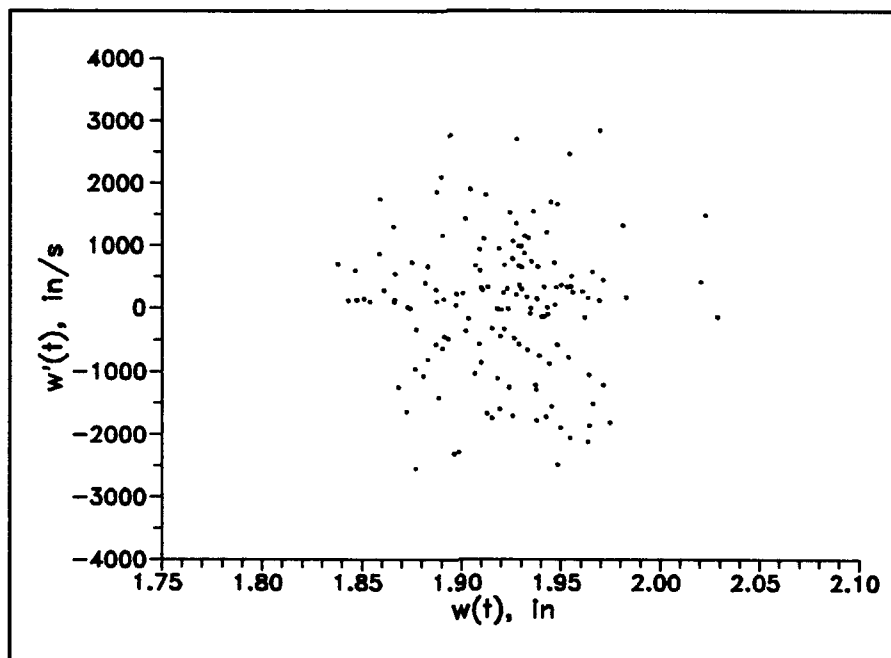
There is ample evidence to show that undamped cylindrical shells exhibit chaotic behavior after collapse. Figure 6.1 shows the phase-plane trajectory of the collapsed response of the 20 in. radius cylindrical shell. This graph indicates that the orbits never close or repeat and that the trajectory fills up a portion of the phase space which are characteristic of chaotic motion. Figure 6.2 shows a Poincaré map of the same shell since the applied force was not of the periodic type, the sampling period  $T$  was chosen to be an average of the time between dominant amplitude peaks. Figure 6.3 shows an expanded portion of the SLR displacement curve (and the data point resolution used in plotting the curve). The highly dynamic changes of the curve illustrates the dilemma in choosing an appropriate sampling time; if a periodic forcing function was applied, the sampling time could have been chosen by the criteria discussed in Section 2.3. Figure 6.2 indicates that the a cloud of unorganized points inhabits a portion of the phase space plane; this is indicative of the existence of a strange attractor (as defined in Section 2.3) which draws the trajectories to a region in the phase space, but due to the lack of dissipation, fractal structures (as defined in Section 2.3) are not expected.

Figure 6.4 shows the phase-plane trajectory of a flat plate subjected to the same loading history applied to the 20 in. radius cylindrical shell. The orbits have more ordered trajectories when compared to Figure 6.1. Since the curves are not closed and repetitive, the motion has the potential to be classified as chaotic. Moreover, a Poincaré map may indicate the presence of fractal-like structures since the trajectories tend to congregate about similar orbital paths.

Unfortunately, the present computational resources limits the amount of available data



**Figure 6.1.** Phase-plane trajectory for chaotic motion of a collapsed 20 in. radius composite cylindrical shell subjected to a transverse point load applied to the center. Shell is undamped.



**Figure 6.2.** Poincaré map of chaotic motion of a collapsed 20 in. radius composite cylindrical shell with no damping.

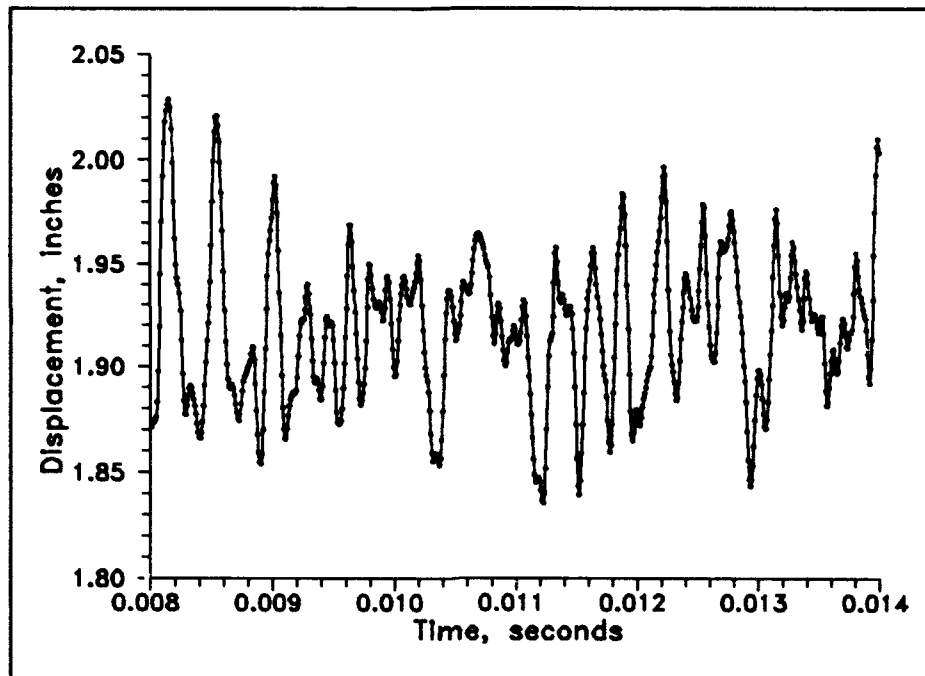


**Figure 6.3.** Portion of the center node displacement history of a collapsed composite cylindrical shell subjected to a transverse point load. Radius = 20 in., SLR formulation.

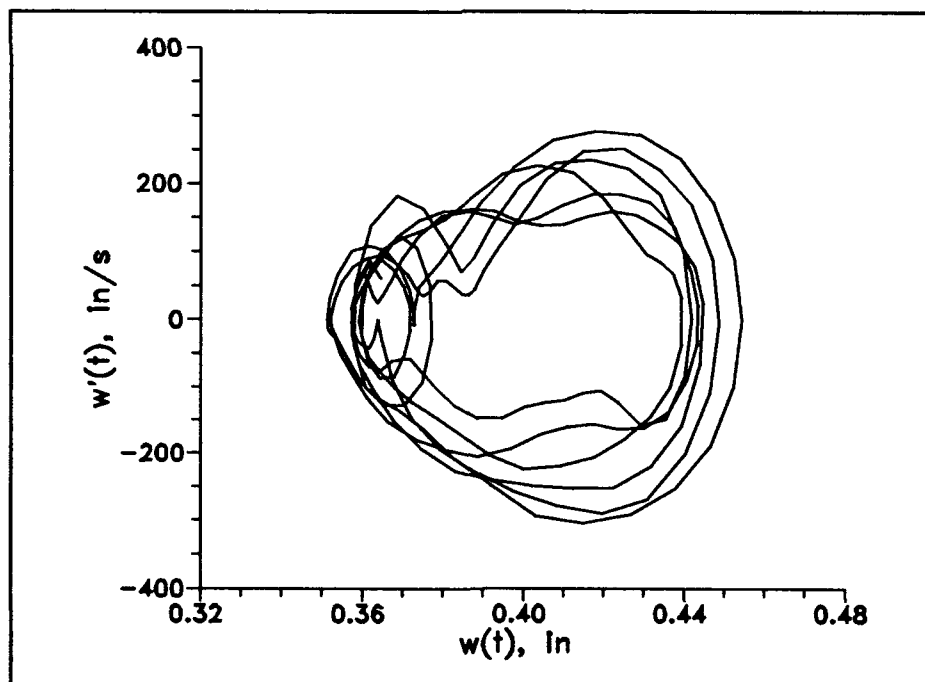


**Figure 6.4.** Phase-plane trajectory for chaotic motion of a flat composite plate subjected to a transverse point load applied to the center.

that may be used to further clarify the existence of chaotic phenomenon. For example, since one point on a Poincaré map represents a minimum of one cycle, hundreds or thousands of cycles are needed to adequately capture the character of a strange attractor. As Figure 4.20 indicates, there are at most 11 cycles. Nearly 3 days of computational time were required to generate the data for that figure. Further, it would be desirable to quantify existence of chaotic behavior with the calculation of Lyapunov exponents, but the time required to generate the necessary amount of data was not available towards the conclusion of this work. Zeng, Eykholt, and Pielke (29) have demonstrated that a minimum of about 5000 data points in three- or four-dimensional phase space, without transients, is needed to obtain a reasonable Lyapunov value. The largest number of data points generated for one particular shell geometry in this work numbered no more than 2500 data sets (including transients) and required in excess of 2 weeks. Attempts were made to utilize Wolf's algorithm (27) to determine the largest Lyapunov exponent for the collapsed 12 and 20 in radius shells since there appeared to be several hundred cycles available. However, Wolf's algorithm is generally oriented to systems with dissipation. The highly dynamic behavior of the data for the two shell geometries did not lead to a convergence to a Lyapunov exponent. The calculation of Lyapunov exponents is based on exponential growth between a reference trajectory (called a *fiduciary* by Wolf et al. (27) and a point on a nearby trajectory. When the growth between the two trajectories grows at a rate which is larger than an exponential rate, the algorithm seeks out a new nearby trajectory. As Figure 6.3 might suggest, the erratic behavior of the signal may not be suitable for the algorithm since large changes take place over a very short period.

A cursory examination of the Donnell curve in Figure 4.1 would suggest that the pre-

collapsed shell center-node displacement history is a result of the superposition of harmonic motions. However, a truly quasiperiodic signal would have closed and exactly repeating orbits. Figure 6.5 is a phase-plane trajectory of the pre-collapsed 8 in. radius shell and shows harmonic or quasiperiodic motion is not present. Chien and Palazotto (2) noted harmonic motion of arches subjected to step loads. However, the applied loads were significantly less than the collapse load. Greer (6) also noted harmonic motion in composite cylindrical shells when the applied load was far less than the collapse load. He concluded that the nonlinear portions of the SLR formulation played a minimal part in the displacement solution for that case. Yet at the same time, he noted that the motion of a free edge node exhibited chaotic tendencies. Figure 6.5 suggests that chaotic tendencies are present in the 8 in. radius uncollapsed shell. A possible explanation is that since the applied load is close to the collapse load, nonlinear terms are significant enough to influence the solutions and hence throw the trajectory off a harmonic path.

Figure 6.6 is a pseudo-phase-plane trajectory of the pre-collapsed behavior of an 8 in. radius Donnell shell. The similarities between this figure and the previous figure further supports the possibility of chaotic behavior since the orbits are nonrepetitive. The similarities between the two figures also validates that a single time dependent variable may provide enough information to classify the existence of chaotic or non-chaotic behavior, especially when only one variable is measured (numerically or experimentally). Moon (10:43) suggests that one may numerically integrate (if velocity, for example, is the only measured parameter) or differentiate (if displacement, for example, is the only measured parameter) in order to obtain the necessary information to plot a phase-plane history or a Poincaré map. Again, due to the tendency of the trajectories to congregate

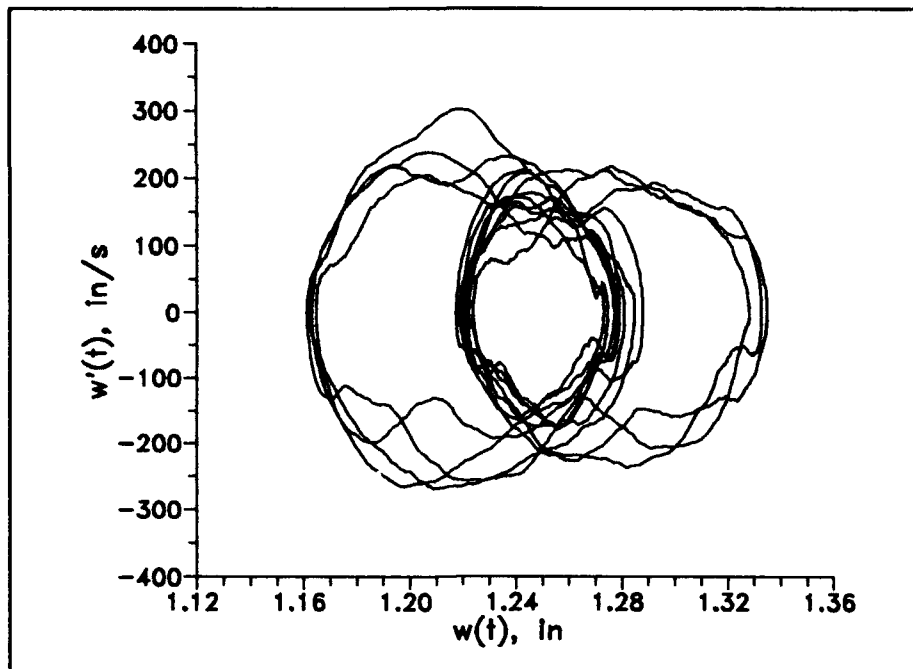


**Figure 6.5.** Phase-plane trajectory of an uncollapsed composite cylindrical shell subjected to a transverse step load applied to the center. Radius = 8 in., Donnell formulation.

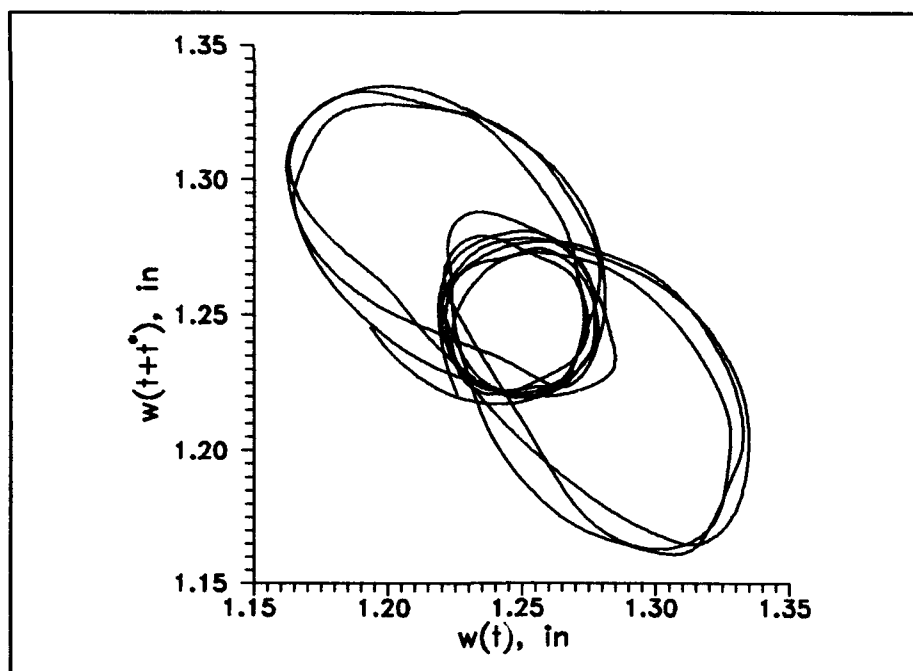


**Figure 6.6.** Pseudo-phase-plane trajectory for an uncollapsed composite cylindrical shell subjected to a transverse step load applied to the center. Radius = 8 in., Donnell formulation.

about similar orbital paths, a Poincaré map might reveal the presence of fractal structures if enough data points were available.

A spectrum analysis of the displacement history suggests the presence of chaotic behavior. Figures 6.7 and 6.8 show the frequency spectrums of the 12 in. radius shells after collapse. The response over a broad range of frequencies implies chaotic behavior. The results also show that the SLR and Donnell formulations yields similar collapsed-shell frequency responses. In both cases, there is a gradual attenuation of signal strength as frequency increases. Figure 6.9 shows the frequency spectrum of the 20 in. radius shell using the SLR formulation. The Donnell model yielded similar results and is not presented. Figure 6.10 is the frequency spectrum of the uncollapsed 8 in. radius cylindrical shell. In a periodic or quasiperiodic signal, there would be discrete peaks corresponding to the signal frequencies separated by flat responses in between. The figure shows that the predominant signals form at the lower end of the scale as expected since the displacement waveform is composed of lower frequency signals. Instead of a flat response after the low frequencies, the signal strength gradually tapers off, i.e., a weak, but broad spectrum of frequencies nonetheless. This characteristic may be further evidence that a shell may display chaotic behavior without collapsing. A frequency analysis of the 8 in. radius collapsed shell using the SLR formulation was not carried out due to the limited amount of data available corresponding to the collapsed state.

Figures 6.11, 6.12, 6.13, and 6.14 show the phase-plane plots of three of the composite plates subjected to step loads that have different initial loading rates. Figure 6.14 is the same as Figure 6.13 with the exception that the scale is expanded to reveal more details of the phase-plane trajectories. The figures imply that chaotic motion is

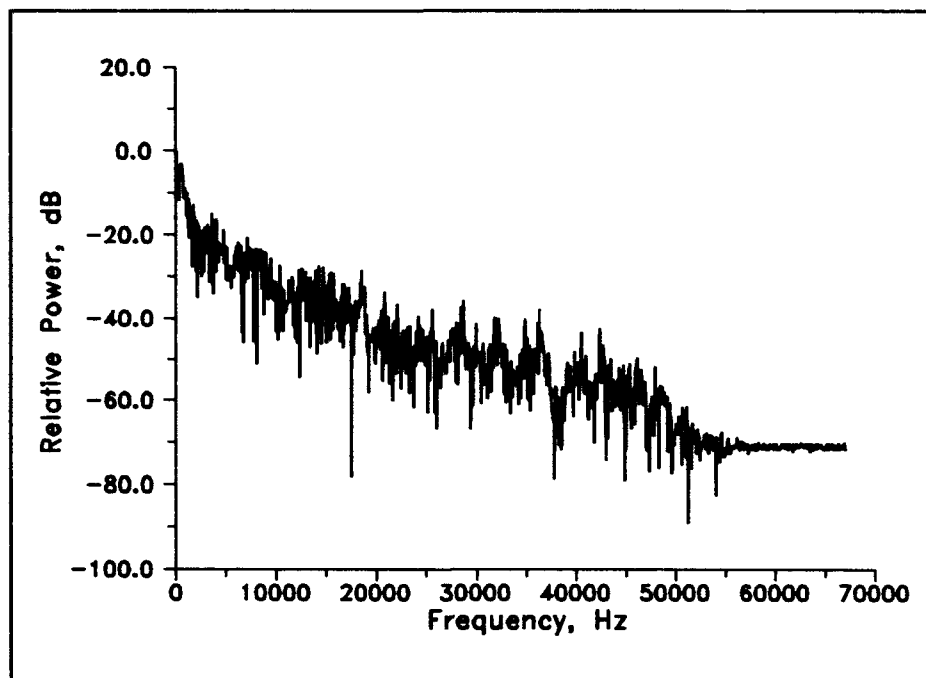


**Figure 6.7.** Frequency spectrum of the center node of a collapsed composite cylindrical shell subjected to a transverse point load applied to the center node. Radius = 12 in., SLR formulation.

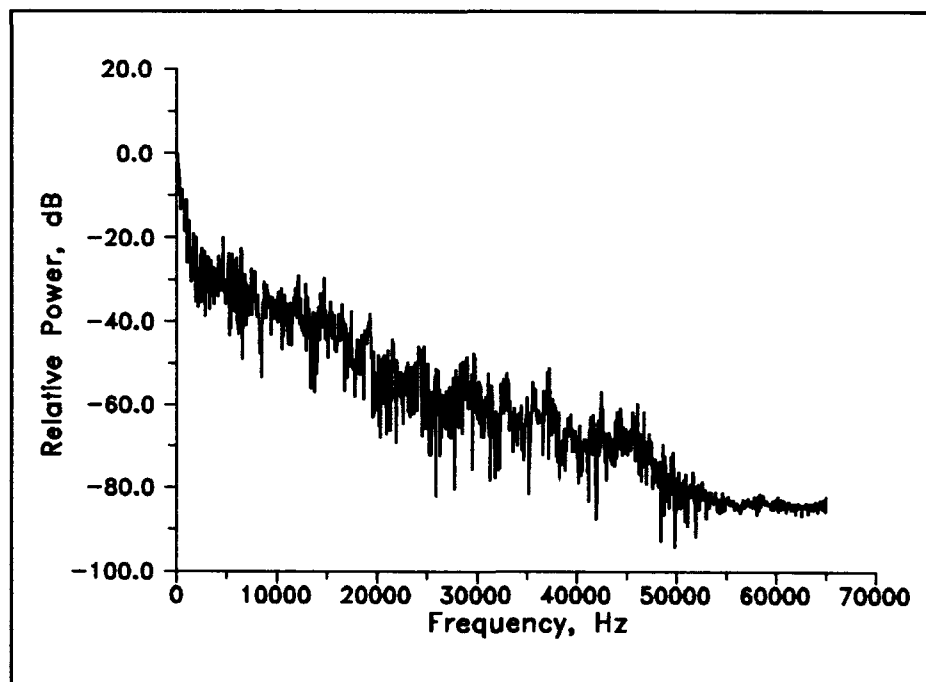


**Figure 6.8.** Frequency spectrum of the center node of a collapsed composite cylindrical shell subjected to a transverse step load applied to the center. Radius=12 in., Donnell formulation.

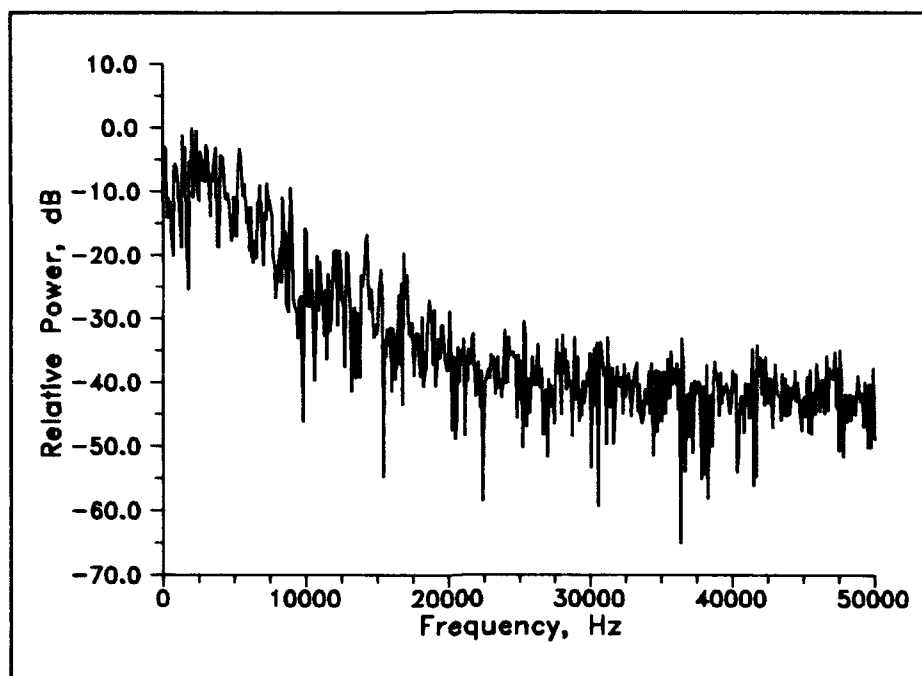


**Figure 6.9** Frequency spectrum of the center node of a collapsed composite cylindrical shell subjected to a transverse step load applied to the center. Radius = 20 in., SLR formulation.

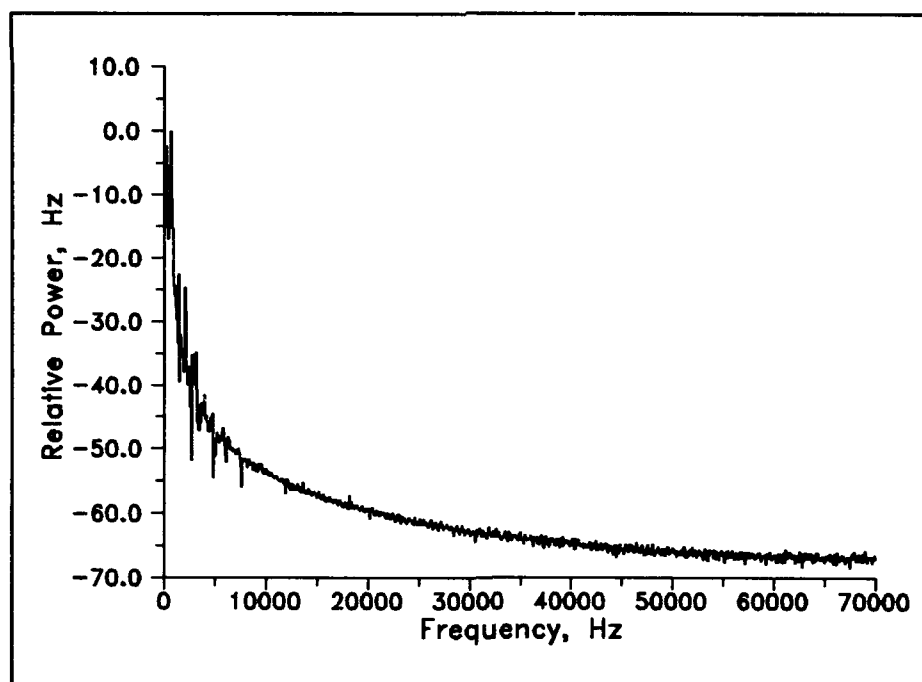


**Figure 6.10** Frequency spectrum of the center node of an uncollapsed composite cylindrical shell subjected to a transverse point load applied to the center. Radius = 8 in., Donnell formulation.

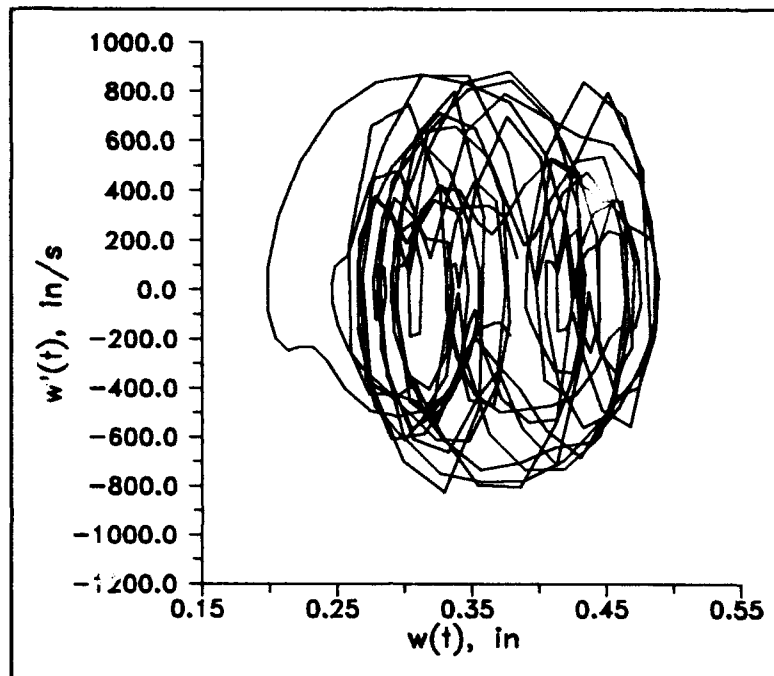


**Figure 6.11.** Phase-plane trajectory for chaotic motion of a flat composite plate subjected to a transverse step load applied to the center. Initial loading rate of  $3.16(10^6)$  lbs/s, max load of 1,592 lbs.

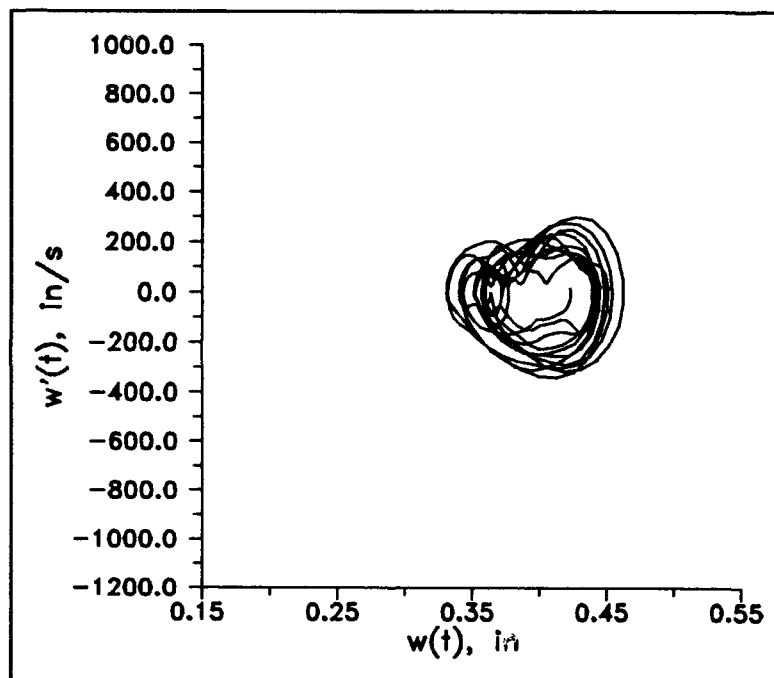


**Figure 6.12** Phase-plane trajectory for chaotic motion of a flat composite plate subjected to a transverse step load applied to the center. Initial loading rate of  $7.9(10^5)$  lbs/s, max load of 1,592 lbs..

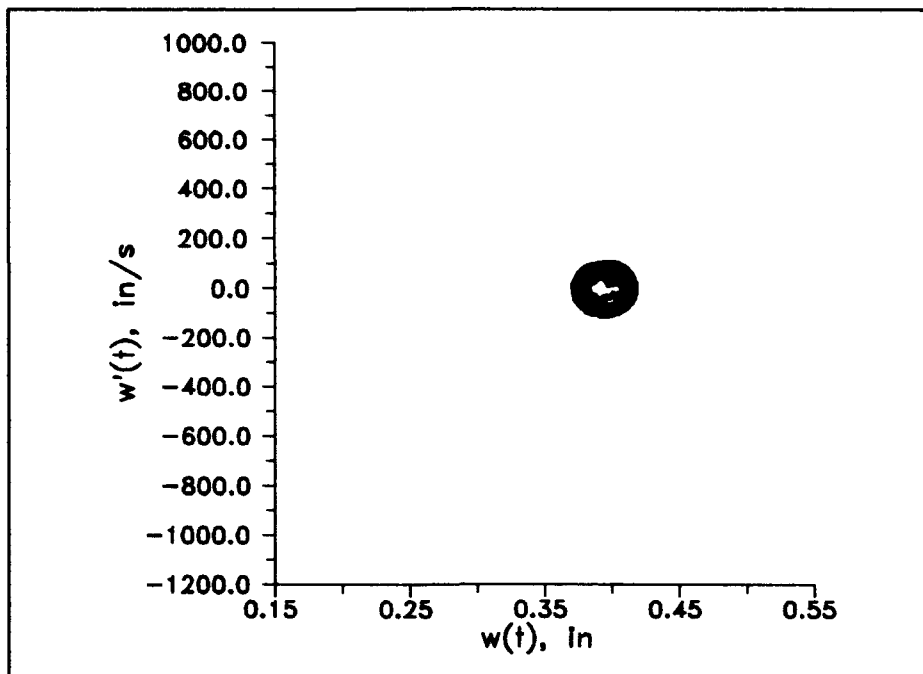


**Figure 6.13.** Phase-plane trajectory for chaotic motion of a flat composite plate subjected to a transverse step load applied to the center. Initial loading rate of  $7.9(10^4)$  lbs/s, max load of 1,592 lbs.

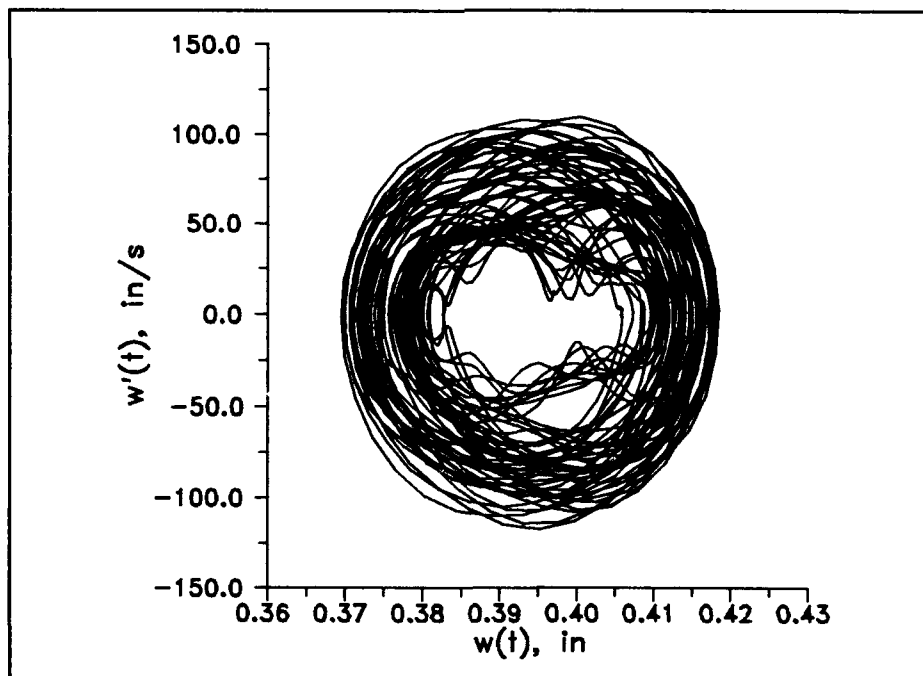


**Figure 6.14.** Scaled up version of Figure 6.13 revealing similar orbital trajectories.

present. They also demonstrate that there is a sensitive dependence on initial conditions, i.e., a definition of chaos. Moreover, as the loading rate decreases, the general path of all the trajectories becomes closer. This phenomenon suggests that if the load is applied at a much slower rate, the phase-plane orbit would tend to a point corresponding to the static equilibrium state, i.e., a quasistatic application of the load. Figures 6.15, 6.16, and 6.17 show the frequency responses of the flat plate center nodes and suggest chaotic behavior is present. As alluded to earlier, the flat plate center node oscillates at generally lower frequencies when compared against the cylindrical shell behaviors.

Since the phase-plane orbits of the plates appeared to have more ordered trajectories, it may be possible that a strange attractor is at work. Figure 6.18 is a Poincaré map of the plate loaded with the lowest loading rate (see Figures 4.22 and 6.14 ). A strange attractor appears to be influencing the orbits since the Poincaré points are congregated in a region in the phase-plane, but the limited number of data points does not allow the identification of fractal-like structures. If fractal patterns were revealed, the predominant state of plate tension, instead of damping, might be the mechanism by which this occurs. Figure 6.19 is the displacement curve used to plot the Poincaré map. This data was also used in an attempt to generate Lyapunov exponents. Wolf's (27) algorithm was used. Input parameters to the algorithm were based on some of his suggested guidelines. For example, he suggested that an embedding dimension  $m$  (the dimension where the attractor exists) of 3 is often sufficient and that the product  $m\tau$  be approximately equal to the mean orbital period. Figure 6.20 shows the results. The two curves correspond to  $m\tau$  values that are slightly more and slightly less than the mean orbital period; a curve corresponding to a value of  $m\tau$  equal to the mean orbital period was not included due to

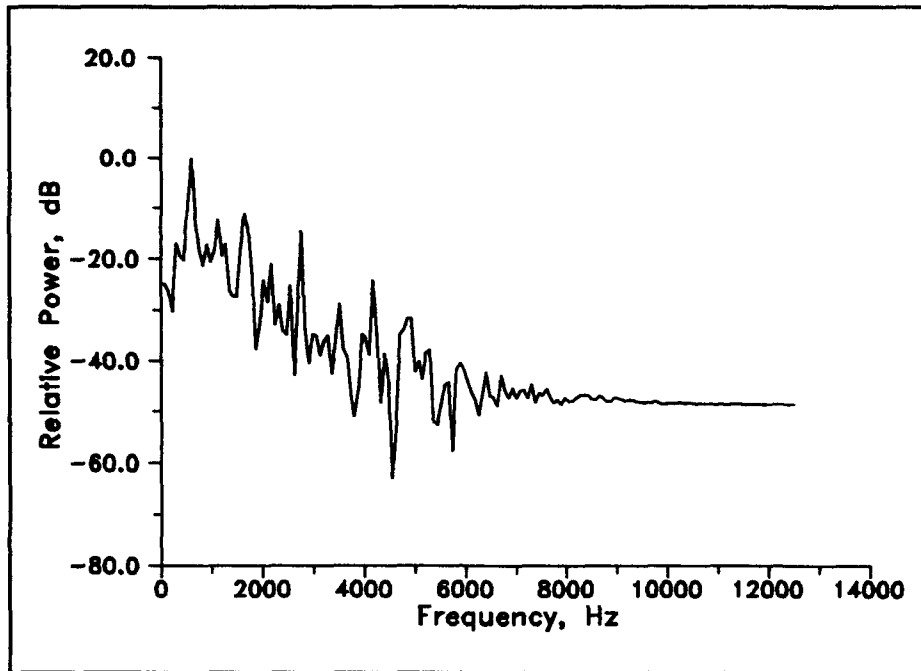


**Figure 6.15.** Frequency spectrum of the center node of a flat composite plate subjected to a transverse step load applied to the center. Initial loading rate of  $3.16(10^6)$ , max. load of 1,592 lbs.

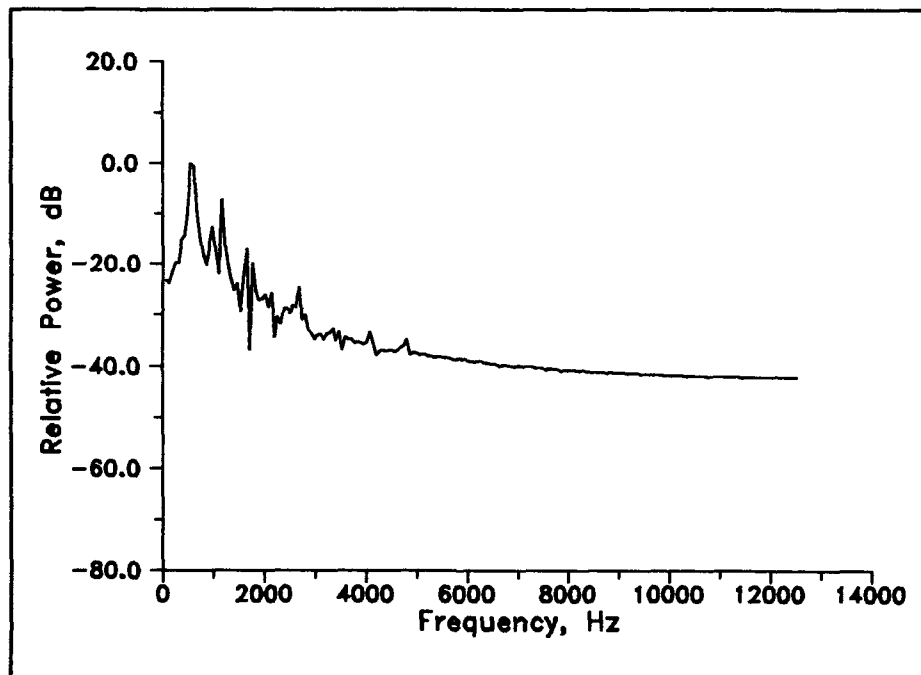


**Figure 6.16.** Frequency spectrum of the center node of a flat composite plate subjected to a transverse step load applied to the center. Initial loading rate of  $7.9(10^5)$  lbs/s max. load of 1,592 lbs.

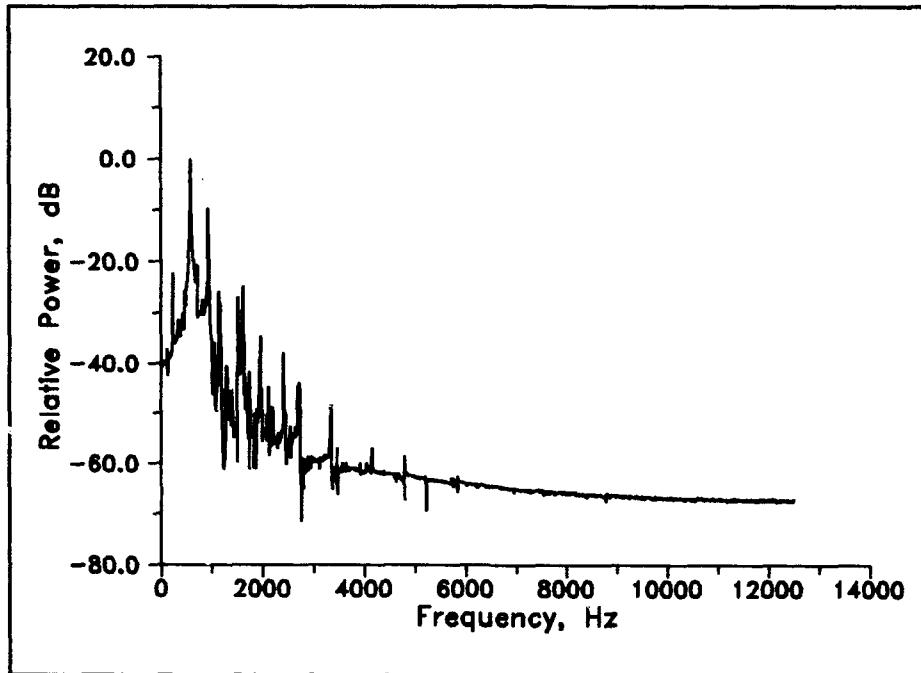


**Figure 6.17.** Frequency spectrum of the center node of a flat composite plate subjected to a transverse step load applied to the center. Initial loading rate of  $7.9(10^4)$  lbs/s, max. load of 1,592 lbs.

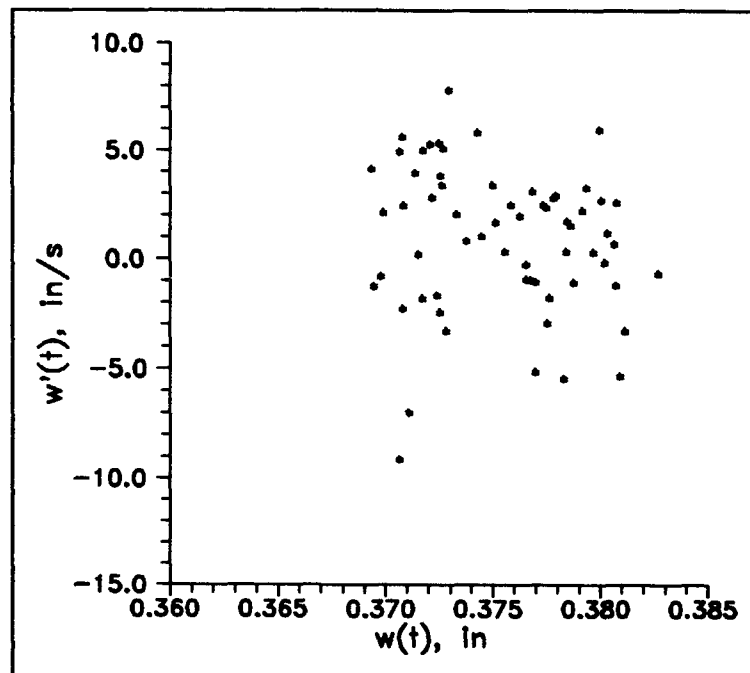


**Figure 6.18.** Poincaré map of a flat composite plate subjected to a transverse point load applied to the center. Initial loading rate of  $7.9(10^4)$  lbs/s, max. load of 1,592 lbs.

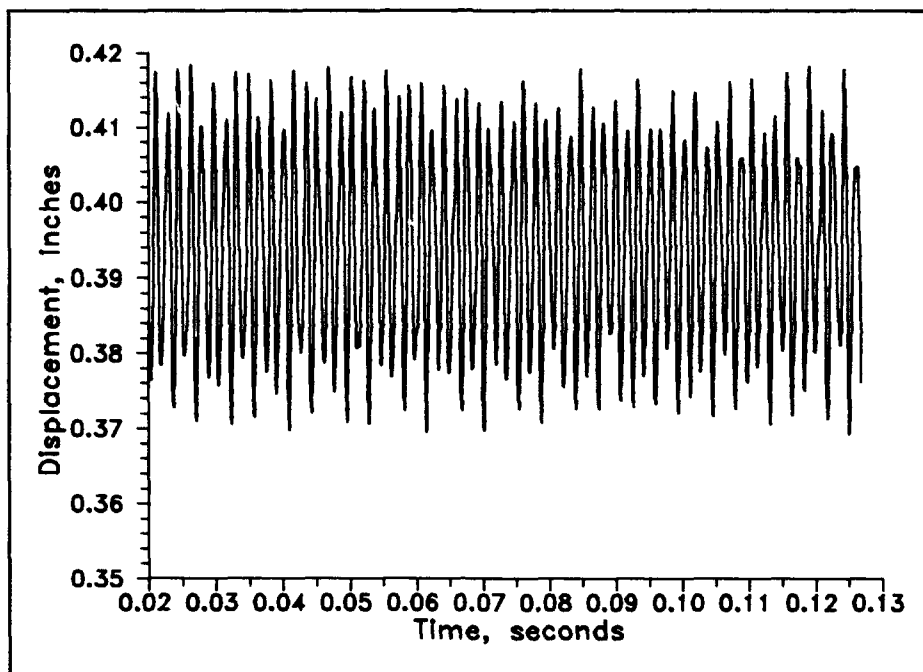


**Figure 6.19.** Center node deflection of a flat composite plate subjected to a transverse step load applied to the center. Initial loading rate of  $7.90(10^4)$  lbs/s, max. load of 1,592 lbs.

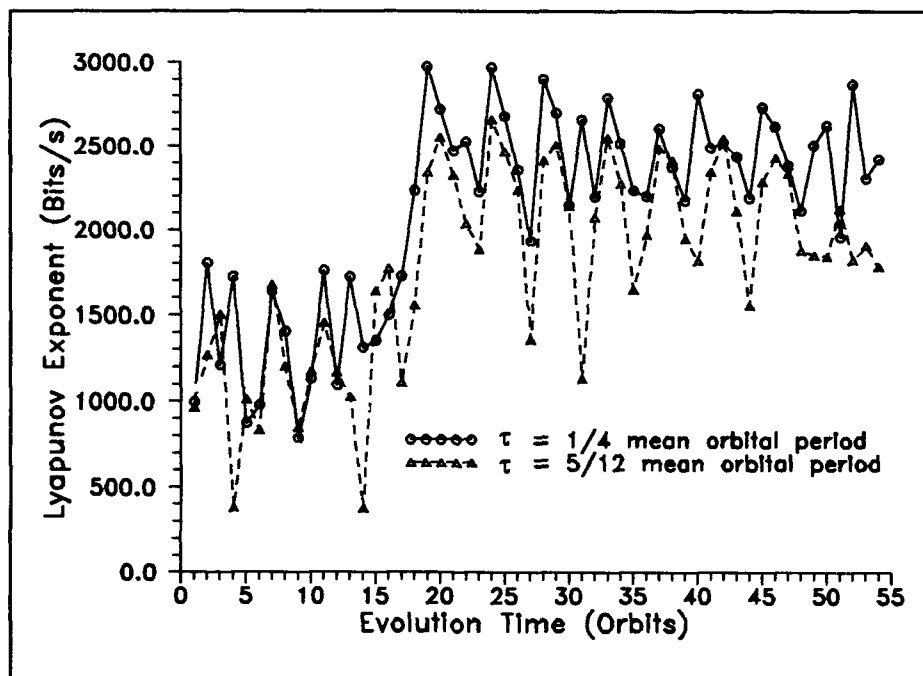


**Figure 6.20.** Possible convergence of the Lyapunov exponent of a transversely loaded flat composite plate (see Figure 6.19).

the confusing overlapping curves that resulted. The two curves appear to oscillate about two different positive steady state values. Lyapunov exponents measure the rate at which system processes create or destroy information and may be expressed as bits per second (27). The value of bits/s refers to the predictive accuracy of the data. For example, if the Lyapunov exponent was actually 2,000 bits/s and if an initial point were known with an accuracy of one part per million (20 bits), future behavior cannot be predicted after  $(20 \text{ bits}) / (2,000 \text{ bits/s}) = 0.01 \text{ seconds}$ , which corresponds to approximately 5 orbits (approximately 48 data points equally spaced by  $4.0(10^5)\text{s}$  in this case). The actual accuracy of the data in parts per million is not known at this time. Nevertheless, the two curves show that the Lyapunov exponents are expected to remain positive. If so, this quantitatively defines the plate behavior as chaotic. Longer computer runs would be needed to assure that the exponents do not suddenly become negative.

## **VII SUMMARY, CONCLUSIONS, AND RECOMMENDATIONS**

### **7.1 Summary**

The composite plate and cylindrical shell models examined in this research were assumed to remain perfectly elastic with no dissipation and no material failure. 5 distinct stages were noted in the displacement history of the cylindrical shells subjected to a transverse step load applied to the center. First there is the initial increase in the center node velocity resulting in a dimpling of the shell. Second, there is a reduction in the displacement rate which may or may not be very distinct depending on the shell radius. This stage is manifested in the creation of a trough or crease along the shell centerline. Third, shell collapse occurs which is characterized by a sudden velocity increase of the entire displacement field (with the exception of the hinged boundaries). Fourth, there is a period of highly dynamic motion that decays with time. Finally, the shell settles into a stage where relatively large motions no longer occur. The shell is near the static equilibrium solution, but low amplitude, high frequency vibrations are taking place both in-plane and out of plane. Plates only exhibited the last two behaviors after maximum center node deflection occurred.

One characteristic briefly noted in earlier work with the DSHELL code is the large secondary motions that are associated with the short but highly dynamic phase after shell collapse in response to the transversely applied point load. This behavior was primarily noted in both SLR and Donnell formulations for most of the shells. Shallower shells did not exhibit this feature because lighter loadings did not provide enough energy to the system to evoke this type of response. Plates subjected to higher loadings exhibited this response but the effects were greatly diminished.

Graphical mesh representations can reveal important qualitative information about plates and shells at a glance. The most obvious information is the overall geometric configurations that occur when the load is applied. Another feature is a general impression of the stress/strain fields as the shell deforms. Comparisons between the distorted and undistorted elements provides this impression. One other feature is that vibrational characteristics of the system are evident by examining a sequence of meshes separated in time. Further, graphical representations provide the structural analyst with information on which criteria can be based or a method to focus-in on behaviors that may require further examination.

## *7.2 Conclusions*

Numerically stable solutions for the period following shell collapse are always obtainable with the iterative methods used in the DSHELL program. The pre-collapse time step selection criteria advocated by Greer was effective for all cylindrical shell configurations considered. The post-collapse time step selection criteria considered in this research was effective for all Donnell shells, but not for all SLR shells. The SLR formulation is more sensitive to time step choices for the deeper shells. For  $h/c$  ratios of 0.273 (in this case, the 6 in. radius shell) and greater, successively smaller time steps were required for numerically stable results during the collapsed shell stages. The SLR formulation carries substantially many more terms than the Donnell formulation and is therefore prone to a combination of the three basic numerical errors, namely round-off, truncation, and propagated errors (16).

For predicting the shell behavior all the way up to the near collapsed configurations,

the modified Donnell and SLR formulations produce essentially the same results. This is an important result because the Donnell formulation is substantially faster than the SLR version. Therefore, the Donnell model can be used when large deflections and rotations are not a prime consideration. However in predicting the behavior at collapse and beyond, the two models produce differing results for the deeper shell depths. Shell depth-to-chord ratios,  $h/c$ , less than or approximately equal to 0.276 (in this case, the 8 in. radius cylindrical shell) are perhaps the limit of the predictive capability of the SLR formulation; this is still a substantial number since it implies rotations of almost  $60^\circ$  and a displacement that is 50 times the thickness. Although it is recognized that plasticity and material failure in the composite would occur at these rotations and deflections, it does show that the SLR model has the *potential* to accurately predict the response of real systems, if plasticity and material failure were incorporated into the program, since the SLR model predicts theoretical behavior that cannot be achieved by current composite materials. At these  $h/c$  ratios, the Donnell model predicts odd shell configurations during the transient phase and much larger deflections after the transient phase when compared to the SLR model. The Donnell model is therefore suspect at these levels of displacements and rotations. It is not clear if the Donnell model is suitable for predicting post collapse behavior for the next lowest  $h/c$  ratio studied (0.183) since the shell did not collapse as expected. This phenomenon shows that Donnell models tend to have higher effective flexural stiffnesses, as one might expect since many higher-order rotational terms are absent from the formulation.

For shells with  $h/c$  ratios between 0.183 and 0.076, the Donnell and SLR formulations produce similar results with some differences during the transient phase. Therefore, if the

analyst is interested in long-term behavior, the Donnell model is sufficient and more efficient from a computational standpoint. If the relatively short dynamic phase (which may include significant backlash for the structure) is an important consideration, the SLR model is recommended. For shells with  $h/c$  ratios less than 0.076, including plates, the behaviors predicted by the two models are similar. Composite plates in particular had no differences in the center node displacement curves. Therefore for computational efficiency, the Donnell model should always be used when very shallow shells or plates are analyzed. One may also conclude that cylindrical shells with  $h/c$  ratios less than or equal to 0.076 is one definition of a shallow shell.

Shells that do not collapse have the potential to exhibit chaotic behavior. The geometric nonlinear features of the Donnell and SLR formulations makes this possible. Since Greer noted harmonic motion with loads that were somewhat less than the collapse load (about 70% of the collapse load), loads much closer to the collapse load affect the nonlinear terms to the extent that chaotic motion will be evident. Transversely loaded plates do not collapse, but the nonlinear effects will result in the chaotic behavior of composite plates as well. Moreover, loading rate also influences the nature of the chaotic motion. For the composite plate, high loading rates results in erratic phase-plane trajectories whereas gradual loading rates facilitates the influence of the strange attractor.

### *7.3 Recommendations*

The graphical displays showed dynamic behaviors not noted in previous research. These behaviors mainly included large secondary motions during the transient phase and significant in-plane vibrational motions. These observations were qualitative in nature.

Further work can be done to characterize these behaviors in a more quantitative manner using some of the methods used in this work.

In order to more fully explore the issues of chaotic behavior, much more data is needed than was generated by this research. Poincaré maps and Lyapunov estimations were used to a very limited extent in this work and the results were not conclusive due to the lack of data. It would also be desirable to include damping effects in the hope of utilizing other methodologies available in analyzing chaotic behavior (damping had been used in earlier research with DSHELL (2) but to a very limited extent). Computational efficiency is another requirement. Aside from improving the present computer hardware, one suggestion would be to reduce the complexity of the systems to be analyzed. Arches, for example, are less complex than cylindrical shells but would exhibit many of the same pre- and post-collapsed characteristics; computational runs should produce significantly more information in comparatively shorter times. Another possibility is simply include damping to the flat plates studied. It was noted that the Von Karman model produced the same results as the SLR model. The Von Karman model required far less computational time than the SLR models. With more data generation, more definitive results with Lyapunov exponents and Poincaré maps could be achieved. Another quantitative technique that could be explored is the calculation of fractal dimensions. Other graphical techniques such as logistic maps, circle maps, horseshoe maps, etc., could also be considered. Finally, periodic load functions should be considered because most of the research on chaotic behavior of structural systems use this feature. For example, Moon (10:133) has shown that a periodic driving force facilitates the identification of fractal-like patterns.

## APPENDIX A Effect of Radius on Flexural Stiffness

For cylindrical shells with the same curvilinear dimensions (curvilinear width, length, and thickness), it is intuitive that a shallower shell would collapse at a lower transverse loading than a deeper shell. Therefore, the effective bending stiffness of a shell is affected by the radius. To illustrate this point, consider a thin, isotropic arch with a constant cross section:

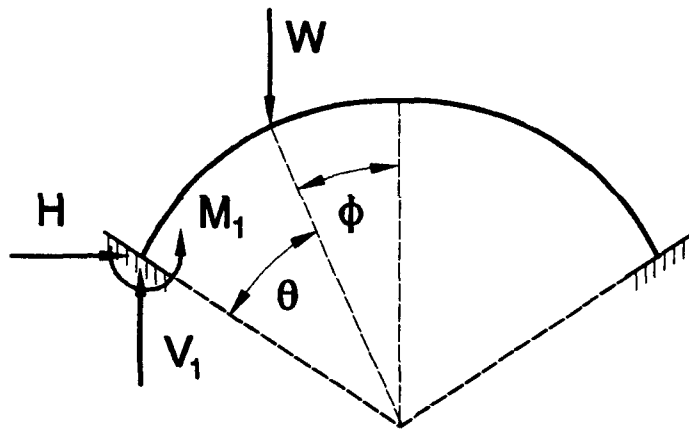


Figure A.1. Thin arch.

where  $W$  is the applied load, and  $M_1$ ,  $H$ , and  $V_1$  are the moment and reaction forces respectively. In order to simplify the problem and gain a general idea of the stress distributions, the arch is assumed to remain rigid. From Roark (18:163), the reaction forces and moment is given by:

$$H = \frac{1}{2} W \left[ \frac{\frac{2}{\theta}(se + \phi sn - sc) - s^2 - n^2 - \alpha(s^2 - n^2)}{\theta + sc - \frac{2s^2}{\theta} + \alpha(\theta + sc)} \right] \quad A.1$$

$$V_1 = \frac{1}{2} W \left( \frac{\theta + \phi - cs + en - 2nc}{\theta - cs} \right) \quad A.2$$

$$M_1 = V_1 R s + H R \left( \frac{\theta c - s}{\theta} \right) + \frac{1}{2} W R \left( \frac{c - e - \phi n - \theta n}{\theta} \right) \quad A.3$$

where  $c = \cos \theta$ ,  $s = \sin \theta$ ,  $n = \sin \phi$ ,  $e = \cos \phi$ , and  $\alpha = I/AR$ .  $I$  and  $A$  are the moment of inertia and area, respectively, of the cross section.  $R$  is the circular radius of the arch. For this example,  $A$  is picked as a square cross sectional area measuring 0.12" x 0.12". The applied load  $W$  is selected as 100 lbs and is applied to the top center of the arch which is defined as the zero coordinate position. The arch length is also held constant at 12 in. Using the above equations and resolving  $H$  and  $V_1$  into stresses results in Figures A.2, A.3 and A.4. These figures compare the stresses and moment distributions as a function of the arc length. Also note that the sign convention chosen has the compressive stresses as positive quantities.

The graphs show that the smaller the radius, the higher the normal compressive stresses. However, the stress due to the moments must be taken into account. The stress due to moment is:

$$\sigma_{moment} = \frac{M_x z}{I^3/12} \quad A.4$$

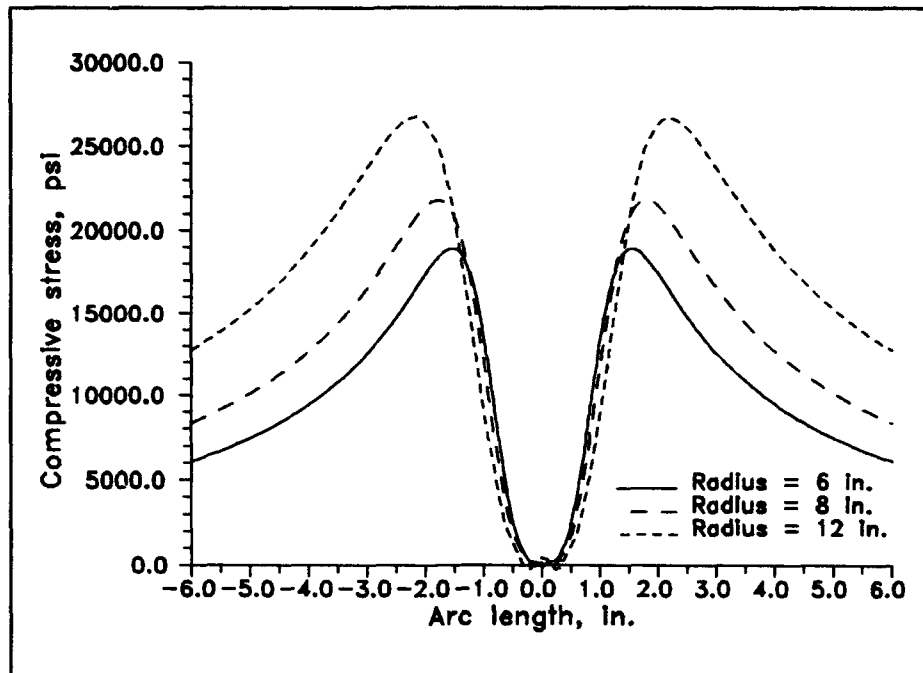


**Figure A.2.** Normal compressive stresses, due to  $H$  and  $V_1$  only, acting on a cross section perpendicular to the neutral axis.

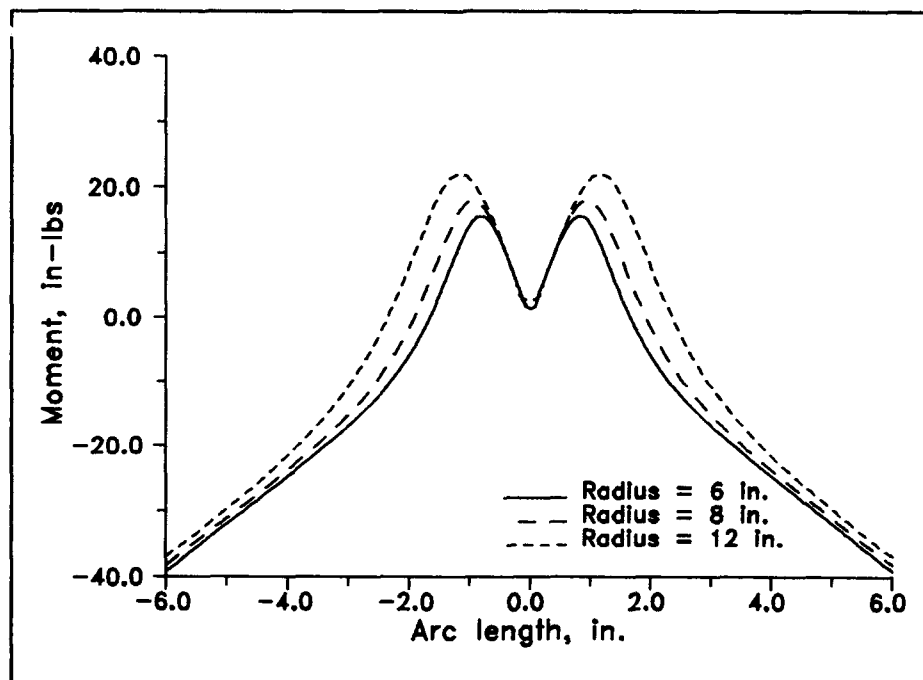


**Figure A.3.** Moments acting along an arch.

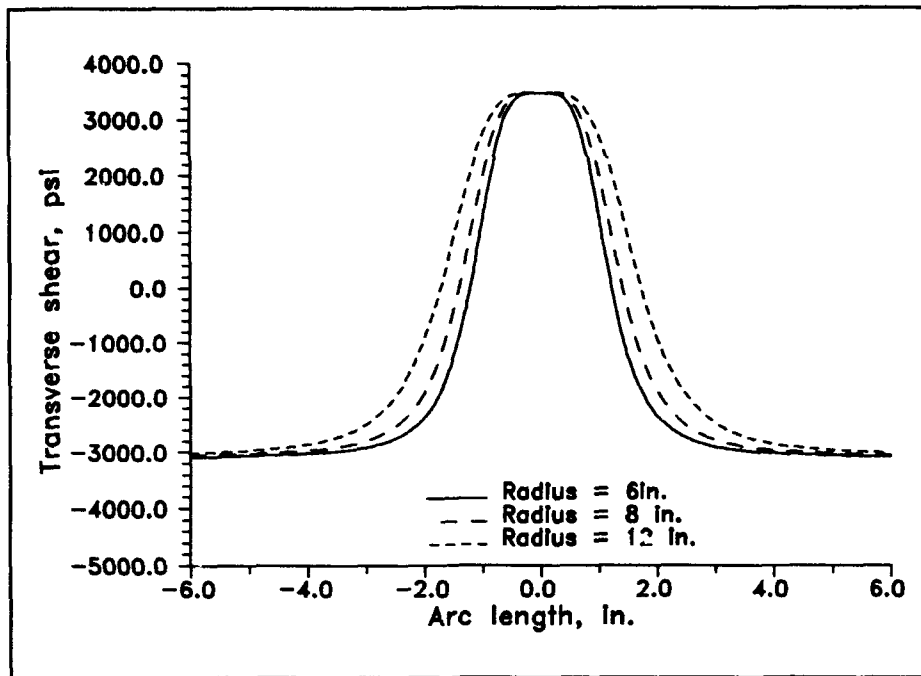


**Figure A.4.** Radial shear stress distribution acting along an arch

where  $M_x$  is moment per unit length. The total membrane stress is:

$$\sigma_x = \frac{N_x}{t} + \frac{M_x z}{t^3/12} \quad \text{A.5}$$

where  $N_x$  is normal stress per unit length. Combining the results of Figures A.2. and A.3. to find the algebraic sum of the stresses over the cross sectional area results in Figure A.5. which shows the average stress distribution along the arch. The figure shows that the shallower beam has generally higher levels of compressive stresses. Compressive membrane forces tend to reduce the bending stiffness of a structure. At some particular load value, the compressive stresses reduce the bending stiffness to zero and buckling occurs [ :429]. For more complex cases such as a thin composite cylindrical shell, the two dimensionality of the system would have to be considered as well. However, this simple example implies the general relationship between shell radius and the effective

bending stiffness for thin shells.

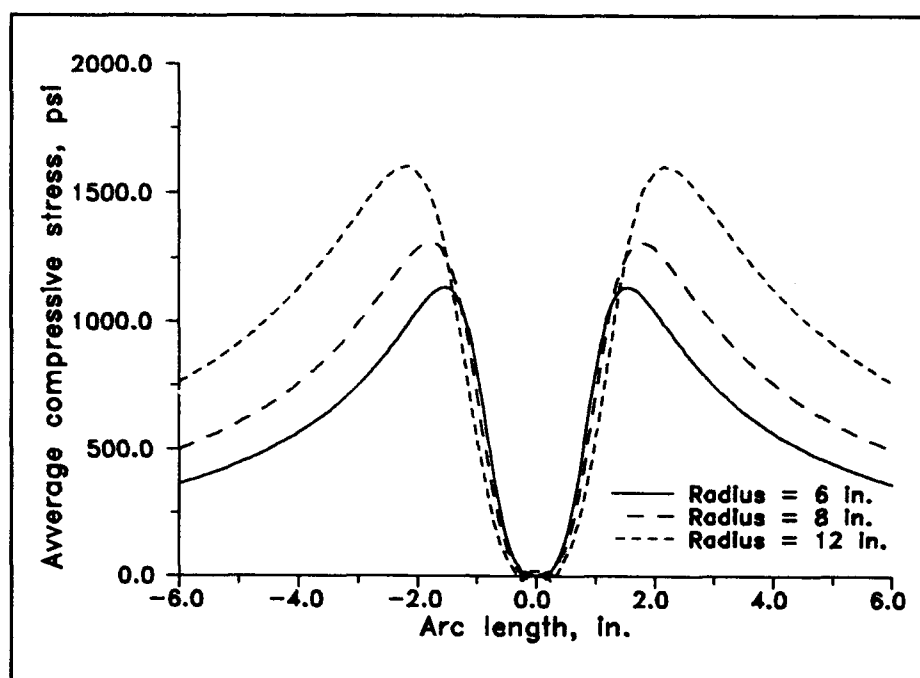


Figure A.5 Average membrane stress distribution along a thin arch.

### *Bibliography*

1. Brush, D. O. and Morton, F. G., "Stress and Stability Analysis of Cylindrical and Conical Shells," *Report LMSD-894808*, Sunnyvale, CA: Lockheed Missles and Space Division (1961)
2. Chien, L.S., and Palazotto A.N., "Nonlinear Snapping Considerations for Laminated Cylindrical Shell Panels," *Composites Engineering*, 2, No. 8:631-639, (1992).
3. Clough, W. and Wilson, E. L. "Dynamic Finite Element Analysis of Arbitrary Thin Shells," *Comput. Struct.* 1:33-56 (1971).
4. Cook, Robert D., et al., *Concepts and Applications of Finite Element Analysis*. New York: John Wiley & Sons, 1989.
5. Flugge, Wilhelm, *Stresses in Shells*, Berlin: Springer-Verlag OHG, 1962.
6. Greer Jr., James M, and Palazotto, A. N., "The Numerical Considerations in Characterizing the Response of a Composite Shell Structure," *Proceedings of the 34th Structures, Structural Dynamics, and Materials (SDM) Conference*, April 19 - 21, 1993.
7. Katona, M.G., and Zienkiewicz, O.C., "A Unified Set of Single Step Algorithms, Part 3: The Beta-*m* Method, A Generalization of the Newmark Scheme," *International Journal for Numerical Methods in Engineering*, 21, No. 7:1345-1359. (1985)
8. Kounadis, A. N. "Chaoslike Phenomena in the Non-linear Dynamic Stability of Discrete Damped or Undamped Systems Under Step Loading," *International Journal of Nonlinear Mechanics*, 26, No. 3: 103-311, (1991).
9. Liaw, Y. C. and Koh, C. G. "Dynamic Stability and Chaos of System with Piecewise Linear Stiffness," *Journal of Engineering Mechanics*, 119, No. 8: 1542-1557.
10. Moon, Francis C., *Chaotic Vibrations: An Introduction for Applied Scientists and Engineers*, New York: John Wiley & Sons, 1987.
11. Naschie, M.S., *Stress, Stability, and Chaos in Structural Engineering: An Energy Approach*. New York: McGraw-Hill Book Co. Inc., 1990.
12. Nayfeh, Ali H. and Mook, Dean T., *Nonlinear Oscillations*. New York: John Wiley and Sons, 1979.

13. Noor, Ahmed K. and Burton Scott B., "Assessment of Shear Deformation Theories for Multilayered Composite Plates," *Applied Mechanics Review*, 42, No. 1:1-11 (1989).
14. Palazotto, A. N., and Dennis, Scott T., *Nonlinear Analysis of Shell Structures*. Washington, D.C.: American Institute of Aeronautics and Astronautics, Inc., 1992
15. Peitgen, Heinz O., Harmut, Jurgens, and Saupe, Dietmar, *Chaos and Fractals New Frontiers of Science*. New York: Springer-Verlag, 1992.
16. Plybon, Benjamin F., *An introduction to Applied Numerical Analysis*. Boston: PWS-Kent Publishing Co. 1992.
17. Rasband, Neil S., *Chaotic Dynamics of Nonlinear Systems*. New York John Wiley and Sons, 1990.
18. Roark, Raymond J. *Formulas for Stress and Strain*, New York: McGraw-Hill Book Co. Inc., 1954.
19. Saada, Adele S., *Elasticity Theory and Applications*. New York: Pergamon Press, 1989.
20. Shaw, S. W. and Holmes, P.J. "A Periodically Forced Piecewise Linear Oscillator," *Journal of Sound Vibration* 90, No. 1:129-155.
21. Siljak, D. D., *Nonlinear Systems*. New York: Wiley, 1969.
22. Silva, K.J. *Finite Element Investigation of a Composite Cylindrical Shell Under Transverse Load with Through the Thickness Shear and Snapping*. M.S. Thesis, AFIT/GAE/ENY/89D-35. School of Engineering, Air Force Institute of Technology (AU), Wright Patterson AFB, OH, 1989.
23. Simitses, George J., *Dynamic Stability of Suddenly Loaded Structures*. New York: Springer-Verlag, 1990.
24. Taylor Jr., Walter W., *Finite Element Investigation Into the Dynamic Instability Characteristics of Laminated Composite Panels*, M.S. Thesis, AFIT/GAE/ENY/90D-28. School of Engineering, Air Force Institute of Technology (AU), Wright Patterson AFB, OH, 1990.
25. Thompson, J.M. and Stewart, H.B., *Nonlinear Dynamics and Chaos*. Chichester, U.K.: Wiley, 1986.

26. Tsai, C. T., and Palazotto, A. N., "On the Finite Element Analysis of Non-Linear Vibration for Cylindrical Shells with Higher-Order Shear Deformation Theory," *International Journal of Non-Linear Mechanics*, 26 No 3/4: 379-388, (1991).
27. Wolf, Alan et al., "Determining Lyapunov Exponents From A Time Series," *Physica D*, 16, 285 - 317 (1985).
28. Yao, John C., "Stability of a Cylinder Under Dynamic Radial Pressure," *A.R.S. Journal*, 31, No. 12: 1705-1708.
29. Zeng, X., Eykholt, R., and Pielke, R.A., "Estimating the Lyapunov Exponent from Short Time Series of Low Precision," *Physical Review Letters*, 66., No. 25:3239-3232, (1991).

### *Vita*

Captain Arthur E. Forral was born on 18 August 1960 at Subic Naval Base, Philippines. He graduated from high school in San Diego, California in 1979 and enlisted in the Air Force 3 May 1979 as an electronics radar technician. He attended the University of California in San Diego, South Florida Community College, and Texas A&M University. Captain Forral earned his Bachelor of Science Degree in Aerospace Engineering from Texas A&M University in 1989 and was commissioned through Officer Training School. He was then stationed at McClellan AFB, California working as a structural engineer on the F-111. He entered the Air Force Institute of Technology, School of Engineering, in May 1992.

# REPORT DOCUMENTATION PAGE

Form Approved  
OMB No. 0704-0188

Public reporting burden for this collection of information is estimated to average 1 hour per response, including the time for reviewing instructions, searching existing data sources, gathering and maintaining the data needed, and completing and reviewing the collection of information. Send comments regarding this burden estimate or any other aspect of this collection of information, including suggestions for reducing this burden, to Washington Headquarters Services, Directorate for Information Operations and Reports, 1215 Jefferson Davis Highway, Suite 1204, Arlington, VA 22202-4302, and to the Office of Management and Budget, Paperwork Reduction Project (0704-0188), Washington, DC 20503

1. AGENCY USE ONLY (Leave blank)		2. REPORT DATE December 1993		3. REPORT TYPE AND DATES COVERED Master's Thesis	
4. TITLE AND SUBTITLE Comparison of the Dynamic Behavior of Composite Plates and Shells Incorporating Green's Strain Terms with the von Karman and Donnell Models				5. FUNDING NUMBERS	
6. AUTHOR(S) Capt Arthur E. Forral					
7. PERFORMING ORGANIZATION NAME(S) AND ADDRESS(ES) Air Force Institute of Technology, WPAFB, OH 45433-5000				8. PERFORMING ORGANIZATION REPORT NUMBER AFIT/GAE/ENY/93D-13	
9. SPONSORING / MONITORING AGENCY NAME(S) AND ADDRESS(ES) Arnold Mayer, WL/FIV and Raje Nachman, AFOSR Wright-Patterson AFB, OH 45433-5000				10. SPONSORING / MONITORING AGENCY REPORT NUMBER	
11. SUPPLEMENTARY NOTES					
12a. DISTRIBUTION / AVAILABILITY STATEMENT Approved for public release; distribution unlimited				12b. DISTRIBUTION CODE	
13. ABSTRACT (Maximum 200 words) The dynamic collapse behavior of thin, composite cylindrical shells subjected to transverse point loads is considered. The dynamic behavior of the undamped cylindrical shells of varying radii is analyzed with a finite element formulation that incorporates all nonlinear Green's strain terms in the in-plane directions; transverse strains are linear and vary parabolically through the shell thickness. This formulation is denoted as the simplified large displacement/rotation (SLR) theory. Graphical representations are used extensively to examine dynamic behaviors not noted in similar research that utilized the DSHELL finite element code. Composite plate behavior is also explored. Comparison of the higher-order formulations to Donnell and von Karman models, modified with transverse shear flexibility, is also made. Several deep shell configurations, using the SLR and Donnell models, are analyzed in an effort to determine the maximum displacement and rotational limits of these formulations. The nonlinear features of the plates and shells imply the potential for <i>chaotic</i> behavior. Various techniques are used to characterize the chaotic behavior of these undamped shells in pre- and post-collapsed states.					
14. SUBJECT TERMS Nonlinear Analysis, Nonlinear Dynamics, Chaos, Finite Element Analysis, Collapse, Buckling, Composites, Structural Mechanics, Cylindrical Shells, Plates				15. NUMBER OF PAGES 106	
				16. PRICE CODE	
17. SECURITY CLASSIFICATION OF REPORT Unclassified	18. SECURITY CLASSIFICATION OF THIS PAGE Unclassified	19. SECURITY CLASSIFICATION OF ABSTRACT Unclassified	20. LIMITATION OF ABSTRACT UL		